

# Computational and Experimental Studies of Redox-Active 1,4-Dithiafulvene Derivatives

by

©Sepideh Mehrani

A Dissertation submitted to the School of Graduate Studies in partial fulfillment of  
the requirements for the degree of

**Ph.D.**

**Department of Chemistry**

Memorial University of Newfoundland

**August 2017**

St. John's

Newfoundland

# Abstract

1,4-Dithiafulvene (DTF) is a  $\pi$ -conjugated organic molecule with excellent electron-donating properties and redox activity, which can be widely used in the application of molecular electronics and optoelectronics. The work described in this dissertation investigates on the fundamental properties of a series of novel DTF-based molecules and macromolecules. The first part of this thesis is focused on the studies of a bis(DTF)-end-capped oligo(phenylene ethynylene). Both experimental characterizations (e.g., cyclic voltammetry, UV-Vis absorption, and Raman spectroscopy) and theoretical density functional theory (DFT) modeling have been conducted to gain insight into the structural, electronic and redox properties of this oligomer in the neutral and oxidized states. Further, the self-assembling behavior of the bis(DTF)-oligomer on the surfaces of mica and highly oriented pyrolytic graphite (HOPG) was examined by atomic force microscopy (AFM). It has been noted that the microscopic morphologies of the self-assemblies of bis(DTF)-endcapped oligo(phenylene ethynylene) on surfaces show redox state dependency. In the second part of this thesis, the adsorption behavior of a carboxyl-substituted DTF molecule on the surface of gold was studied. DFT calculations were performed with the Vienna Ab Initio Simulation Package (VASP) under periodic boundary conditions with Perdew-Burke-Ernzerhof (PBE) correlation and the generalized gradient approximation (GGA) exchange functional. The effect of van der Waals interactions was taken into account by the vdW-DFT (optB88-vdW)

method. The DTF molecule–gold surface interactions were investigated to understand the process of monolayer formation and associated charge transfer properties. Moreover, calculations with and without dispersion correction were performed to examine the role van der Waals interactions play at organic-metal interfaces. Raman spectroscopy and Kelvin probe force microscopy (KPFM) were employed to validate the accuracy of computed work functions. The results demonstrate that the work function of Au (111) can be tuned by depositing a thin film of redox-active DTF molecules with differing molecular dipole moments. Finally, the mechanisms for the reduction of  $\text{HAuCl}_4$  with DTF derivatives were investigated by time-dependent UV-Vis analysis. The experimental results show that stepwise temperature control is a key factor dictating the formation of gold nanoparticles (AuNPs). Overall, this finding points to a promising one-phase synthetic approach for AuNPs in aqueous media.

# Acknowledgements

“Do not judge me by my successes. Judge me by how many times I fell down and got back up again.” Nelson Mandela

Firstly, I would like to express my appreciation to my supervisors Prof. Erika Merschrod and Prof. Yuming Zhao for their support, patience, and motivation. It would not be possible to conduct this project without their advice and support.

Besides my supervisors, I would like to thank Memorial University of Newfoundland, School of Graduate Studies for a fellowship that provided me an opportunity to join the Memorial University’s community. Compute Canada, ACENET, and West-Grid provided infrastructure and support for computational studies. Funding from NSERC and CFI provided a stipend, materials and equipment.

Last but not the least, I would like to thank my family: my parents, my brother and my husband for their continuous support in life.

# Table of Contents

<b>Abstract</b>	<b>ii</b>
<b>Acknowledgments</b>	<b>iv</b>
<b>List of Tables</b>	<b>xii</b>
<b>List of Figures</b>	<b>xxiii</b>
<b>List of Abbreviations and Symbols</b>	<b>xxiv</b>
<b>1 Introduction</b>	<b>1</b>
1.1 Dithiafulvenes and Tetrathiafulvalenes . . . . .	1
1.2 Tetrathiafulvalene Vinylogues: Synthesis and Applications . . . . .	3
1.2.1 TTFV-based Molecular Tweezers as Chemosensors . . . . .	4
1.2.2 TTFV-based Redox-active Ligands . . . . .	6
1.3 Organic Semiconductor/Metal Interfaces . . . . .	7
1.4 Gold Nanoparticles: Synthesis and Properties . . . . .	10
1.4.1 Stabilization and Controlled Growth of AuNPs . . . . .	12
1.4.2 Mechanisms of AuNP Formation . . . . .	14
1.4.3 Functionalization and Application of AuNPs . . . . .	16
1.5 Motivation and Organization of This Thesis . . . . .	18

Bibliography . . . . .	19
<b>Co-authorship Statement</b>	<b>30</b>
<b>2 Redox-dependent Properties of DTF-endcapped <math>\pi</math>-Pligomers</b>	<b>31</b>
2.1 Introduction . . . . .	31
2.2 Experimental Section . . . . .	34
2.2.1 Computational Methods . . . . .	34
2.2.2 Experimental Characterization . . . . .	35
2.3 Results and Discussion . . . . .	36
2.3.1 Structural and Electronic Properties in the Neutral and Oxidized States . . . . .	36
2.3.2 Frontier Molecular Orbitals and Redox Properties in Solution Phase . . . . .	38
2.3.3 Electrochromic Properties in Solution and in the Solid State . . . . .	42
2.3.4 Raman Analysis . . . . .	45
2.3.5 Surface Self-assembling Properties . . . . .	49
2.4 Conclusions . . . . .	51
Bibliography . . . . .	52
<b>3 Self-Assemblies of Dithiafulvene Derivatives on an Au (111)</b>	<b>60</b>
3.1 Introduction . . . . .	60
3.2 Computational Methodology . . . . .	62
3.2.1 Modeling the Gas-Phase Properties of DTF <b>3a</b> . . . . .	62
3.2.2 Modeling the Adsorption Behavior of DTF <b>3a</b> on an Au (111) Surface . . . . .	63
3.3 Experimental Details . . . . .	66
3.4 Sample Preparation . . . . .	67

3.5	Results and Discussion . . . . .	68
3.5.1	Crystallographic and Topographic Properties . . . . .	68
3.5.2	Geometric and Energetic Properties of DTF <b>3a</b> on a Gold Surface	70
3.5.3	Raman Evidence for Geometrical Orientation . . . . .	72
3.5.4	Work Function Modification . . . . .	74
3.5.5	Charge Distribution . . . . .	75
3.5.6	Impact of Terminal Group on Electronic Properties . . . . .	77
3.5.7	Substituent Effect on Charge Distribution . . . . .	79
3.6	Summary . . . . .	82
	Bibliography . . . . .	83
<b>4</b>	<b>Reduction of Au (III) into Au(0) by Dithiafulvenes in Aqueous Me-</b>	
	<b>dia</b> . . . . .	<b>88</b>
4.1	Background . . . . .	88
4.2	Computational Methods . . . . .	89
4.3	Experimental Details . . . . .	90
4.4	Functionalized AuNPs Nucleation and Growth . . . . .	91
4.4.1	UV-Vis Analysis of Functionalized AuNPs . . . . .	95
4.4.2	Raman Analysis of Functionalized AuNPs . . . . .	98
4.5	Time-dependent UV-Vis Spectral Analysis . . . . .	101
4.6	Effective Parameters on Reaction . . . . .	106
4.6.1	Effects of Solvents Polarity . . . . .	107
4.7	Computational Analysis of <b>4a</b> -Au <sub>n</sub> Complex . . . . .	108
4.8	Summary . . . . .	111
	Bibliography . . . . .	112

<b>5</b>	<b>Conclusions and Future Work</b>	<b>116</b>
	Bibliography . . . . .	118
<b>A</b>	<b>Redox-dependent Properties of DTF-encapped <math>\pi</math>-Oligomers</b>	<b>120</b>
	A.1 Electronic Transition and Molecular Orbital Properties . . . . .	120
	A.2 Descriptions of Raman-Active Vibrational Modes . . . . .	124
	A.3 Raman Spectra of the Oxidized Film of <b>2a</b> After Two Weeks . . . . .	128
	A.4 Coordinates of Optimized Geometries and Energies . . . . .	128
<b>B</b>	<b>Redox-dependent Properties of DTF-encapped <math>\pi</math>-Oligomers</b>	<b>134</b>
	B.1 NLO Properties . . . . .	134
	B.2 Phenol Detection . . . . .	135
	B.3 UV-Vis Spectra of DTF and H <sub>2</sub> AuCl <sub>4</sub> . . . . .	137
<b>C</b>	<b>SAM formation of Dithiafulvene Derivatives on Au(111): Orienta-</b>	
	<b>tional Geometry, Binding Energies and Work Function</b>	<b>139</b>
	C.1 Geometry Optimization and Electronic Property Calculations . . . . .	139
	C.2 Molecular Work Function . . . . .	140
	C.3 Polarizability . . . . .	142
	C.4 Raman Spectra of Gold Substrate . . . . .	142
<b>D</b>	<b>Vienna Ab-initio Simulation Package (VASP)</b>	<b>144</b>
	D.1 Introduction . . . . .	144
	D.2 Pseudopotentials and PAW . . . . .	144
	D.3 Periodic boundary condition . . . . .	145
	D.4 Reciprocal space and k-points . . . . .	146
	Bibliography . . . . .	146

<b>E One phase reduction mechanism of Au (III) by dithiafulvene building blocks in aqueous media</b>	<b>149</b>
E.1 Simulated and experimental IR spectra . . . . .	149
E.2 Raman spectra of <b>3a</b> . . . . .	149
E.3 calculated oxidation potential of gold . . . . .	150
E.4 UV-Vis investigations of redox reaction . . . . .	152
E.4.1 UV-Vis spectra of <b>4a</b> before peak deconvolution . . . . .	152
E.4.2 Time dependant UV-Vis measurements . . . . .	152
E.4.3 UV-Vis peaks assignments . . . . .	153
E.5 Substituent effect on electronic levels . . . . .	154
E.6 Substituent effect on structural properties . . . . .	157

# List of Tables

3.1	Adsorption energies ( $E_B$ ), work function of the Au (111) with deposited DTF on top ( $\Phi_{DTF-Au}$ ) and the magnitude of drop in the work function of the Au (111) by deposition of DTF ( $\Phi_{Au} - \Phi_{DTF-Au}$ ) with six different substituents (all values are reported in eV). The electric dipole moments ( $\mu_{tot}$ ) of the single molecule in the gas phase are investigated with B3LYP/6-31++G(d,p) level of theory. . . . .	77
4.1	Calculated oxidation potential of <b>3a</b> and <b>4a</b> in different solvents with B3PW91/6-31+G(D,P) level of theory and basis set (all values are reported in Volts). . . . .	109
A.1	Assignments of electronic transitions of <b>2b</b> in the neutral state. . . .	121
A.2	Assignments of electronic transitions of <b>2b</b> in the radical cation state. . . .	121
A.3	Assignments of electronic transitions of <b>2b</b> in the dication triplet state. . . .	122
A.4	Assignments of electronic transitions of <b>2b</b> the dication singlet state. . . .	122
A.5	Frontier molecular orbital energies of <b>2b</b> in various oxidation states. . . .	122
A.6	Raman active vibrational modes for <b>2b</b> in the neutral state. . . . .	125
A.7	Raman active vibrational modes for <b>2b</b> in the radical cation state. . . .	125
A.8	Raman active vibrational modes for <b>2b</b> in the dication triplet state. . . .	126
A.9	Raman active vibrational modes for <b>2b</b> in the dication singlet state. . . .	127

B.1	The electric dipole moment ( $\mu$ ,D), polarizability ( $\alpha$ ), first hyperpolarizability ( $\beta$ ), and second hyperpolarizability ( $\gamma$ ) of investigated compounds at B3LYP/6-31++G(d,p) level. . . . .	136
C.1	Calculated binding energies ( $E_B$ ), Fermi energies ( $\epsilon_F$ ) and work-function ( $\varphi$ ) of the DTF <b>3a</b> at eighteen different orientations on the surface of Au(111) with (without) dispersion correction. All values are reported in eV. B stands for the benzene plane and "S" stands for the dithiol plane.	141
C.2	Table shows the Au-S <sub>1</sub> and Au-S <sub>C<sub>2</sub></sub> distances (d) in Å along with the C <sub>4</sub> -C <sub>5</sub> and C <sub>3</sub> -S <sub>1</sub> dihedral angle change between plane of bonds ( $\Delta\Phi$ ) by deposition on the A (111) . . . . .	141
C.3	Molecular work function $\varphi$ of the DTF derivatives in the unit cell with (without) dispersion correction. All values are reported in eV. . . . .	142
C.4	The electric dipole moment ( $\mu$ ,D), polarizability ( $\alpha$ ), first hyperpolarizability ( $\beta$ ), and second hyperpolarizability ( $\gamma$ ) of DTF derivatives with different substitutes at para position of benzene ring with B3PW91/6-31+G(d,p) level of theory. . . . .	143
E.1	The calculated oxidation potential of gold(I) to gold(0) in different solvents with b3pw91/6-31+g(d,p) level of theory and basis set (all values are reported in Volts). . . . .	151
E.2	Assignments of electronic transitions of <b>4a</b> in the neutral state. . . . .	153
E.3	Assignments of electronic transitions of <b>4a</b> in the radical cation state. . . . .	154
E.4	The total energies in eV for the compound in Figure 4.1 with different R substituents and at three positions of ortho, meta, and para on the benzene ring. . . . .	155

E.5	Fermi energies in eV for the compound in Figure 4.1 with different R substituents and at three positions of ortho, meta, and para on the benzene ring. . . . .	155
E.6	HOMO, LUMO, band gap energies of the ortho, meta, and para at neutral state obtained with b3pw91/6-31+g(d,p) level of theory and basis set. . . . .	156
E.7	HOMO, LUMO, band gap energies of the ortho, meta, and para at neutral state obtained with b3pw91/6-31+g(d,p) level of theory and basis set. . . . .	156
E.8	C <sub>1</sub> -C <sub>2</sub> -C <sub>3</sub> -S <sub>1</sub> dihedral angles before and after oxidation for the compound with different Substituents at three positions of ortho, meta, and para. . . . .	157

# List of Figures

1.1	Redox processes taking place on DTF and TTF. . . . .	2
1.2	Oxidative dimerization reaction of DTF. . . . .	4
1.3	Binding of TTFV-phenylboronic acid molecular tweezer <b>1</b> to a saccharide molecule in water. . . . .	5
1.4	Redox-active Mo-TTFV complex <b>2</b> and Zn-TTFV complex <b>3</b> . . . . .	7
1.5	Schematic illustration of an OFET. . . . .	7
1.6	(a) The electrostatic stabilization of neighboring metal particles that are approaching together until the surface to surface distance becomes larger than the particle's double layer. (b) The potential energy as a function of the surface to surface distance is plotted, which exhibits the dominance of repulsion forces before the maximum total potential. The total potential tends to a stronger van der Waals force by further decreasing the distance by agglomeration. The dashed green line represent the total potential as the sum of repulsive and attractive forces. (c) Schematic of steric stabilization of nanoparticles by coating with the layer of anchoring polymer. (d) The neighboring particles experience strong repulsive forces when particles are closer than the anchored layer. . . . .	12
2.1	General redox reactivity of a DTF-substituted arene. . . . .	32

2.2	Structures of bis(DTF)-endcapped oligo(phenylene ethynylene)s <b>2</b> . . .	33
2.3	Optimized geometry of <b>2b</b> at the B3LYP/6-31++G(d,p) level and adopted labeling scheme in this study. . . . .	36
2.4	(A) Comparison of averaged C=C and C≡C bond lengths of compound <b>2b</b> in neutral (Neu), radical cation (RC), singlet dication (DC(S)), and triplet dication (DC(T)) states. (B) A resonance scheme for the radical cation of <b>2b</b> . (C) Calculated spin density map for the radical cation of <b>2b</b> . (D) Calculated spin density map for the triplet dication of <b>2b</b> . The high and low unpaired electron density areas are highlighted by blue and green colours respectively. . . . .	37
2.5	Contour maps of frontier MOs for compound <b>2b</b> (isovalue = 0.02 a.u.) and their eigenvalues calculated at the B3LYP/6-31++G(d,p) level. .	39
2.6	Square scheme of stepwise oxidation of <b>2b</b> to radical cation and dication. Gibbs free energies ( $\Delta G$ ) are indicated in the unit of $\text{kJ mol}^{-1}$ .	40
2.7	(A) CV and (B) DPV profiles of <b>2a</b> ( $1.33 \times 10^{-3}$ M) measured in $\text{CH}_2\text{Cl}_2$ at room temperature with $\text{Bu}_4\text{NBF}_4$ (0.1 M) as the supporting electrolyte, glassy carbon as the working electrode, Pt wire as the counter electrode, Ag/AgCl as the reference electrode. CV conditions: scan rate = $50 \text{ mV s}^{-1}$ . DPV conditions: scan rate = $20 \text{ mV s}^{-1}$ , pulse width = 20 mV, pulse period = 200 ms, pulse amplitude = 50 mV, and step = 4 mV. . . . .	41
2.8	NPA charge distribution for compound <b>2b</b> in the neutral (Neu), radical cation (RC), and triplet dication (DC(T)) sates. The values indicated are accumulated NPA charges for the atoms in each shaded area. . . .	42

2.9	(A) Normalized UV-Vis absorption spectrum of <b>2a</b> measured in CH <sub>2</sub> Cl <sub>2</sub> at room temperature. (B) UV-Vis absorption spectrum of the thin film of <b>2a</b> cast on a quartz slide. (C) UV-Vis absorption spectrum of the thin film of <b>2a</b> measured after exposure to iodine vapour for 30 min. (D) Calculated UV-Vis absorption spectrum (normalized) of <b>2b</b> . (E) Calculated UV-Vis absorption spectrum (normalized) of the radical cation of <b>2b</b> . (F) Calculated UV-Vis absorption spectra (normalized) of the dications of <b>2b</b> in the singlet and triplet states. . . . .	44
2.10	Raman spectroscopic analysis monitoring the thin film of <b>2a</b> upon exposure to iodine vapour at various time periods. The baselines of the spectra were corrected using the <i>Fityk</i> software (free version 0.9.8) [53].	45
2.11	Raman spectra of compound <b>2b</b> in different oxidation states calculated at the B3LYP/6-31++G(d,p) level of theory. . . . .	46
2.12	Selected Raman-active vibrational eigenvectors for compound <b>2b</b> at different oxidation states calculated at the B3LYP/6-31++G(d,p) level.	47
2.13	Comparison of (A) the Raman spectrum for the thin film of <b>2a</b> upon exposure to iodine vapour for 10 min and (B) the simulated Raman spectrum for a mixture of <b>2b</b> in neutral, radical cation, and triplet dication states at a 10:1:1 molar ratio. . . . .	48
2.14	AFM images of compound <b>2b</b> (A) on freshly cleaved mica surface, (B) on mica after oxidation with iodine for 30 min, (C) on freshly cleaved HOPG, and (D) on HOPG after oxidation with iodine for 30 min. . .	50
3.1	(A) Molecular structure of carboxylated DTF <b>3a</b> , and (B)–(E) four possible modes by which <b>3a</b> can be bound to a metal surface. . . . .	63

3.2	(A) and (B) Optimized structure of DTF <b>3a</b> , which represents a dihedral angle of 1.47 degrees between the planes of C <sub>4</sub> -C <sub>5</sub> and C <sub>3</sub> -S <sub>1</sub> . (C) Representation of the highest occupied and lowest unoccupied molecular orbitals of DTF <b>3a</b> . . . . .	64
3.3	Total and projected density of states of (left) the bulk (right) and the Au (111). Total DOS of bulk closely matches the local DOS of the third layer of the slab. The numbering of the layers in the slab starts from the closest slab to the adsorbent. . . . .	66
3.4	XRD patterns of the gold substrate prepared experimentally. . . . .	68
3.5	AFM topography of (A) the bare gold substrate, (B) the gold substrate with a thin film of DTF <b>3a</b> deposited on top of it, and (C) the thin film of DTF <b>3a</b> deposited on a glass slide. . . . .	69
3.6	Optimized structure of DTF <b>3a</b> deposited on the surface of the Au (111). (A) and (B) show the face-on orientation at two different side views, (C) and (D) show two views of the edge-on orientation with a 42.8° angle between the plane of the benzene ring and the surface of the slab. . . . .	71
3.7	(A) Simulated Raman spectrum of DTF <b>3a</b> in the gas phase obtained by B3PW91/6-31+G(d,p) level of theory. (B) Raman spectrum of the pure compound in the solid state. (C–F) Raman spectrum of the DTF <b>3a</b> on the surface of 15 nm Au (111) at different concentrations, starting from the lowest concentration on the bottom. . . . .	73
3.8	Vibrational modes of calculated peaks at 498, 519, 1453 cm <sup>-1</sup> . . . . .	74

3.9	Iso-surfaces of difference charge distributions over adsorbent and surface at the top and side view with and without considering vdW interactions. The negative area (green) shows the gaining of electrons, and the positive area (yellow) indicates the production of holes. The plot of charge distribution versus distance in the z-axis can be seen on the right side of each type of calculation which is aligned with the side view of the iso-surfaces. . . . .	76
3.10	Iso-surfaces of difference charge distribution over adsorbent and surface at top and side views with considering vdW interactions for (A) CHO (B) CN (C) NH <sub>2</sub> (D) NO <sub>2</sub> (E) OCH <sub>3</sub> substituents. The negative area (green) associated with gaining electrons and the positive area (yellow) indicates the production of holes. The plot of charge distribution versus distance in the z-axis can be seen on the right side of each type of calculations which is aligned with the side view of the iso-surfaces. . .	80
3.11	Iso-surfaces of difference charge distribution over adsorbent and surface at top and side views without considering vdW interactions for (A) CHO (B) CN (C) NH <sub>2</sub> (D) NO <sub>2</sub> (E) OCH <sub>3</sub> substituents. Negative area (green) shows the gaining of electrons and positive area (yellow) indicate the production of holes. The plot of charge distribution versus distance in the z-axis can be seen on the right side of each type of calculations which is aligned with the side view of the iso-surfaces. . .	81

4.1	The structure of the DTF oligomer with R substituent at the <i>para</i> position of the benzene ring (yellow color represents sulfur atom). Two different substituents of carboxyl (DTF <b>3a</b> ) and carboxymethyl (DTF <b>4a</b> ) were used for future comparison studies. Dimerization occurs under oxidative condition by losing hydrogen through a bridging carbon atom between the five-membered ring and the benzene (Chapter 2 (Figure 2.1)).	91
4.2	Left) The solution of <b>4a</b> in methanol before (vial number one with yellow color) and after (vial number two with orange color) mixing it with the H <sub>Au</sub> Cl <sub>4</sub> and sonication for an hour. Right) The UV-Vis spectra of solution number one and two as labeled. AuNPs peak at peak at 525 nm appeared after addition of the H <sub>Au</sub> Cl <sub>4</sub> .	92
4.3	SEM images of the AuNPs that are freshly prepared through redox reaction of <b>3a</b> and gold acid. The film of solution on the glass slide was then coated with a layer of carbon for imaging.	93
4.4	AFM height image of the deposited AuNPs on freshly cleaved mica at two scan areas. Left) the AFM image of the surface at 10×10 nm scan area. Right) The focused AFM image of the flower shape feature in 5×5 nm scan area.	93
4.5	(A) The solution of <b>3a</b> in acetone and a trace of water (yellow solution). The color of the solution turns green by addition of preheated H <sub>Au</sub> Cl <sub>4</sub> to 40 °C and gradually turns orange by heating and stirring. (B) The solution of <b>4a</b> in acetone and a trace of water (yellow solution). The color of the solution turns blue by addition of preheated H <sub>Au</sub> Cl <sub>4</sub> to 40 °C and gradually turns orange by heating and stirring.	95

- 4.6 (Top) UV-Vis spectrum of **4a**; the peak at 420 nm refers to the maximum absorption of **4a** in neutral form, which is shown in simulated UV-Vis spectrum of **4a** in neutral form (Figure 4.7 (A)). (Middle) UV-Vis spectrum of **4a** after half an hour addition of H<sub>AuCl</sub><sub>4</sub> and sonication; the peak at 524 nm corresponds to the AuNPs absorbance. (Bottom) UV-Vis spectrum of **4a** after twenty four hours following addition of the H<sub>AuCl</sub><sub>4</sub>; the AuNPs corresponding peak is shifted to the higher wavelengths at 547 nm with relatively higher absorbance. . . . 96
- 4.7 (A) and (C) are simulated UV-Vis spectra of **4a** in neutral and oxidized forms, which are obtained with time-dependent B3PW91/6-311G(d,p) level of theory and basis set and 40 number of states. Simulated UV-Vis spectrum indicate that there is no band between 500–600 nm before, and after oxidation of **4a**. Therefore the band at 524 nm right after addition of H<sub>AuCl</sub><sub>4</sub> refers to the AuNPs absorbance, which shifts for 23 nm to the higher wavelength after twenty-four hours (Figure 4.6). (B) and (D) are simulated UV-Vis spectra of dimerized **4a** in neutral and oxidized forms, which are computed with time-dependent B3PW91/6-31+G(D,P) level of theory and basis set and the number of states is 40. . . . . 97
- 4.8 (A) and (D) The experimental Raman spectra of **3a** in methanol before and after addition of H<sub>AuCl</sub><sub>4</sub>, respectively. Red spectrum (D) is taken from the solution of **3a** after twenty-four hours of mixing it with H<sub>AuCl</sub><sub>4</sub> in which the color was turned orange. (B) and (E) Simulated Raman spectra of dimerized **3a** in neutral and oxidized states, respectively. (C) and (F) Simulated Raman spectra of **3a** in neutral and oxidized states, respectively. . . . . 99

4.9	(A) The experimental Raman spectrum of <b>4a</b> in methanol. (B) Simulated Raman spectra of dimerized <b>4a</b> in neutral form. (C) Simulated Raman spectrum of <b>4a</b> in neutral form at B3PW91/6-31+G(G,P) level of theory and basis set. C=O bond stretching band appears in both computed and experimental spectrum of <b>4a</b> and dimerized <b>4a</b> at 1800 and 1620 cm <sup>-1</sup> , respectively. All simulations performed at B3PW91/6-31+G(D,P) level of theory and basis set. . . . .	100
4.10	Vibrational modes of three enhanced peaks at 1289 and 1612, 1726 cm <sup>-1</sup> observed in the Raman spectra of <b>3a</b> computed with B3PW91/6-31+G(D,P) level of theory and basis set. . . . .	101
4.11	Left) Experimental time-dependent UV-Vis spectra of <b>4a</b> in acetone and a trace of water before and after addition of the pre-warmed H <sub>2</sub> AuCl <sub>4</sub> at different time intervals. Red spectra are taken after warming the solution that was left in the closed cap vial overnight. Right) Peak intensity versus time are plotted for major peaks that are indicated in UV-Vis spectra. . . . .	103
4.12	(Left) Experimental UV-Vis spectra of <b>3a</b> in acetone and a trace of water before and after addition of the pre-warmed H <sub>2</sub> AuCl <sub>4</sub> to 40 °C throughout 32 hours. (Right) Peak intensity versus time is plotted for the assigned peaks. . . . .	105
4.13	Optimized structure of <b>4a</b> and a group of gold atoms (n= 1,3). . . . .	110
4.14	Mülliken charge distribution over <b>4a</b> -Au <sub>3</sub> after oxidation. Red regions represent a higher concentration of electron density while green shows less electron density. . . . .	111
A.1	Contours of frontier MOs for compound <b>2b</b> in the radical cation state and their eigenvalues calculated at the B3LYP/6-31++G (d,p) level. . . . .	123

A.2	Contours of frontier MOs for compound <b>2b</b> in the triplet dication state and their eigenvalues calculated at the B3LYP/6-31++G (d,p) level. .	123
A.3	Contours of frontier MOs for compound <b>2b</b> in the singlet dication state and their eigenvalues calculated at the B3LYP/6-31++G (d,p) level. .	124
A.4	Raman active vibrational vectors for compound <b>2b</b> in the neutral state calculated at the B3LYP/6-31++G(d,p) level. . . . .	125
A.5	Raman active vibrational vectors for compound <b>2b</b> in the radical cation state calculated at the B3LYP/6-31++G(d,p) level. . . . .	126
A.6	Raman active vibrational vectors for compound <b>2b</b> in the dication triplet state calculated at the B3LYP/6-31++G(d,p) level. . . . .	127
A.7	Raman active vibrational vectors for compound <b>2b</b> in the dication singlet state calculated at the B3LYP/6-31++G(d,p) level. . . . .	128
A.8	Raman spectra of the solid thin film of <b>2a</b> on a glass substrate measured (A) before exposure to iodine vapour, (B) after exposure to iodine vapour for 65 min, and (C) after being left in open air for two weeks.	129
A.9	Cartesian coordinates of compound <b>2b</b> in the neutral state (sum of electronic and thermal Energies = $-2746.293943$ Hartree, zero-point correction = $0.377252$ Hartree) . . . . .	130
A.10	Cartesian coordinates of compound <b>2b</b> in the radical cation state (Sum of electronic and thermal Energies = $-2746.077723$ Hartree, zero-point correction = $0.378033$ Hartree) . . . . .	131
A.11	Cartesian coordinates of compound <b>2b</b> in the dication singlet state (sum of electronic and thermal Energies = $-2745.773027$ Hartree, zero-point correction = $0.378722$ Hartree) . . . . .	132

A.12 Cartesian coordinates of compound <b>2b</b> in the dication triplet state (sum of electronic and thermal Energies = $-2745.779398$ Hartree, zero-point correction = $0.378547$ Hartree) . . . . .	133
B.1 UV-Vis spectra of (orange) glass slide that are coated with gold layer (yellow) coated glass slide with gold that was then immersed in the solution of DTF, that is dissolved in toluene, for two hours (blue) the prepared surface that was immersed in the phenol solution with concentration of 500 ppm for two hours. . . . .	137
B.2 Raman spectra of (a) glass slide that is coated with gold layer and then immersed in the solution of DTF, that is dissolved in toluene, for two hours (b) glass slide that is coated with gold layer and then immersed in the solution of DTF, that is dissolved in toluene, for twenty-two hours (c) the prepared surface that was immersed in the phenol solution with concentration of 500 ppm for two hours. . . . .	138
B.3 UV-Vis spectra of . . . . .	138
C.1 Energy variation by increasing the cell lengths in (x, y,z) directions with (A) and without (B) dispersion correction. The numbers that are shown on the x-axis stand for (15,8,8), (20,15,15), (24,17,17), (25,20,20), (25,25,25) and (30,25,25) dimensions , respectively. All total energies have been obtained by $5 \times 5 \times 1$ number of k-points. . . . .	140
C.2 Raman spectra of the prepared gold substrate. . . . .	142
D.1 A sample INCAR file that was used for optimization and work-function calculations in this work. . . . .	147

E.1	IR spectra of (A) dimerized <b>3a</b> powder, (B) residual particles of mixed dimerized <b>3a</b> and gold acid solutions.(C) and (D) Calculated IR spectra of dimerized <b>3a</b> in neutral and oxidized forms in order. . . . .	150
E.2	(A) Experimental Raman spectra of <b>4a</b> in methanol. (B) Simulated Raman spectra of dimerized <b>4a</b> . (C) Simulated Raman spectra of <b>4a</b> in neutral states. . . . .	151
E.3	UV-Vis spectra of <b>4a</b> in acetone (yellow graph), after addition of HAuCl <sub>4</sub> for half an hour (Orange graph) and after twenty four hours (red graph). . . . .	152
E.4	Time-dependent UV-Vis spectra of 3 samples of <b>3a</b> in acetone and trace of water at different concentrations. . . . .	153
E.5	The structure of dithiafulvenyl with R substituent at the para position of the benzene ring. . . . .	157

# List of Abbreviations and Symbols

AFM	Atomic Force Microscopy
AuNPs	Gold NanoParticles
CPD	Contact Potential Difference
CV	Cyclic Voltmmetric
DFT	Density Functional Theory
DOS	Density of State
DTF	Dithiafulvene
DLS	Dynamic Light Scattering
E	Energy
FCC	Face-Centered Cubic
FET	Field-Effect Transistors
GGA	Generalized Gradient Approximation
HOPG	Highly Ordered Pyrolytic Graphite
ITO	Indium Tin Oxide
KPFM	Kelvin Probe Force Microscopy
MOFs	Metal Organic Frameworks
OFET	Organic Field-Effect Transistors
OLED	Organic Light-Emitting Diodes
PV	Photovoltaic

PAW	Projected Augmented Wave
SAM	Self Assembled Monolayer
SEM	Scanning Electron Microscopy
SERS	Surface Enhanced Raman Scattering
TEM	Transmission Electron Microscopy
TTFV	Tetrathiafulvalene Vinylogue
UV-Vis	Ultra Violet-Visible spectroscopy
$E^{vac}$	Vacuum Potential
vdW	Van der Waals Interactions
XPS	X-ray Photoelectron
$\rho$	Charge Density
$\mu$	Electric Dipole Moment
$\epsilon_F$	Fermi Energy
$\Phi$	Work Function

# Chapter 1

## Introduction

### 1.1 Dithiafulvenes and Tetrathiafulvalenes

The design of new organic electronic devices requires systematic investigations into the relationships between  $\pi$ -conjugated organic molecular structures and solid-state properties. In this context, an intriguing class of sulfur-containing heterocyclic compounds, namely 1,4-dithiafulvene (DTF) and tetrathiafulvalene (TTF), have captured considerable attention ever since the discovery of the first TTF-based organic conductor by Wudl and co-workers in 1972 [1]. DTF and TTF derivatives are excellent organic  $\pi$ -electron donors. As shown in Figure 1.1, each of the DTF and TTF molecules contains five-membered 1,3-dithiole ring(s), which is non-aromatic according to the Hückel's rule. By oxidation, these molecules can be converted into relatively stable radical cation and dication, in which the dithiole ring becomes an aromatic  $\pi$ -sextet after releasing an electron [2]. The gaining of aromaticity thus leads to lowered oxidation potential(s) for DTF and TTF molecules. Moreover, most of the redox reactions taking place on DTF and TTF moieties are reversible. For these reasons, DTF and TTF have been extensively used as functional molecular building blocks in a wide

range of advanced organic electronic materials.

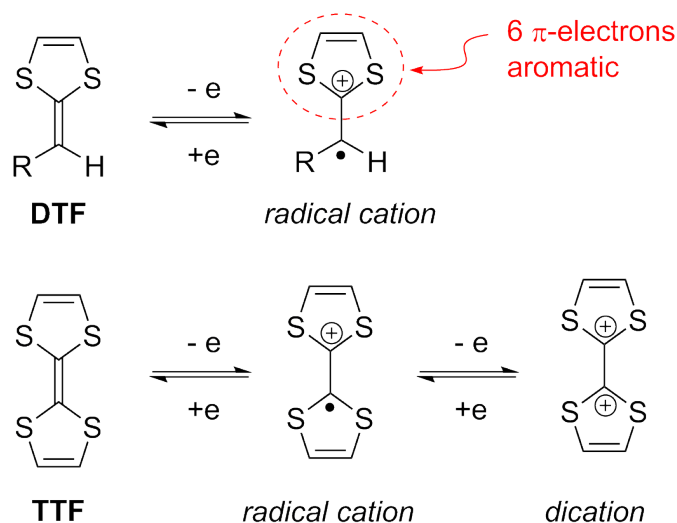


Figure 1.1: Redox processes taking place on DTF and TTF.

Enormous research efforts have been dedicated to the synthesis and characterization of DTF and TTF related molecules and macromolecules for several decades [2]. The unique reversible redox activities, switchable conformation and charge transfer properties of DTF and TTF systems have attracted extensive research activities focusing on the design and synthesis of the new DTF and TTF derivatives [3,4]. Recently, DTF and TTF derivatives have found promising applications in electronic devices, such as batteries, field effect transistors (FETs), and molecular junctions [5–7]. Furthermore, TTFs can be used to prepare switchable self-assembled structures on the surfaces of gold nanoparticles (AuNPs) with their optoelectronic properties well controlled by external inputs [8].

It has been demonstrated that modifications of the structures of DTF and TTF derivatives through advanced organic synthesis provide an effective approach for bottom-up control over a wide range of molecular and supramolecular properties [9]. Some changes in the molecular structures of DTF and TTF derivatives, such as extending  $\pi$ -conjugation paths and adding electron-donating/accepting substituents,

can lead to dramatically altered electronic, photonic, electrochemical, and solid-state packing properties. In this vein, the most commonly adopted strategy for tuning the electronic and redox characteristics of DTF and TTF molecules is to link various substitutes directly to their core  $\pi$ -structures [10,11].

In material and device applications, solid-state packing is a critically important parameter in addition to the structural and electronic properties of discrete molecules. In particular, the optoelectronic performances of organic  $\pi$ -conjugated materials in the solid state are significantly affected by the degree of  $\pi$ -conjugation of the molecules as well as their intermolecular interactions [12,13]. The stacking nature of organic semiconductors has been known to play a key role tuning their band gap energies [14,15]. Modifications of DTF and TTF structures to gain elongated  $\pi$ -conjugated molecular backbones offer an effective way to enhance intermolecular  $\pi$ -stacking. In this respect,  $\pi$ -extended DTF and TTF oligo-/polymers have been actively investigated and applied in novel optoelectronic devices, such as molecular sensors, semiconductors, and nonlinear optics [10].

## 1.2 Tetrathiafulvalene Vinylogues: Synthesis and Applications

An intriguing reactivity of DTF molecules is that they can undergo a facile oxidative dimerization reaction to yield a class of  $\pi$ -extended TTF analogues, namely tetrathiafulvalene vinylogues (TTFVs). Figure 1.2 illustrates the mechanistic details of this dimerization reaction. Aryl-substituted DTF molecules are particularly reactive through this pathway. TTFVs refer to the class of TTF analogues in which the two dithiole rings are connected through conjugated vinyl bridges. Aryl-substituted TTFVs have been extensively investigated by the Zhao group [2] and others over the

past ten years. This class of compounds has shown much better redox activity relative to that of simple TTF due to increased  $\pi$ -conjugation in their structures. Moreover, TTFV compounds can dramatically change their conformations at different redox states, making them interesting redox-controlled molecular switches.

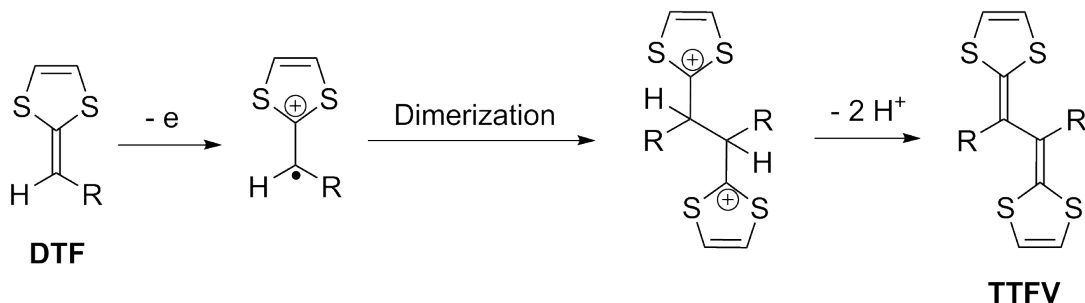


Figure 1.2: Oxidative dimerization reaction of DTF.

The advantageous redox and conformational properties of TTFVs have found extensive applications in optoelectronic devices recently. The most promising properties are driven from their redox versatility and structural switchability, which have led to the design of a large variety of redox-active molecules [16,17], chemical sensors [18–20], supermolecular hosts for fullerenes and single-walled carbon nanotubes [21,22]. In addition, some challenging macromolecular structures, including shape-persistent macrocycles and  $\pi$ -conjugated polymers, have been successfully synthesized recently by the Zhao group using TTFV as the essential building component [23,24]. The following section highlights some recent applications of TTFVs in materials chemistry.

### 1.2.1 TTFV-based Molecular Tweezers as Chemosensors

Aryl-substituted TTFVs usually take a tweezer-like conformation in the neutral state, in which the two dithiole rings are in a pseudo-*cis* orientation. The unique molecular conformations have allowed a series of molecular tweezers to be constructed using TTFV as the central unit. The arene ends of these TTFV tweezers can be read-

ily functionalized with receptor groups for selectively binding with various chemical species. The versatility of these molecular tweezers offers a useful platform for the design of advanced chemical and biological sensors. For example, Figure 1.3 shows a phenylboronic acid functionalized TTFV tweezer **1**, which was synthesized by the Zhao group in 2013. Phenylboronic acid is a well-known saccharide receptor, due to its ability to selectively bind with diols and polyols in aqueous media. Herein, the attachment of two boronic acid groups in compound **1** enables strong binding with monosaccharides under physiological conditions (aqueous, pH 7.4). The binding event changes the oxidation potential of the central TTFV unit, which can be easily detected by electrochemical analysis (e.g., differential pulse voltammetry). As such, compound **1** functions as a redox chemosensor for monosaccharides. Through the same design concept, TTFV tweezers functionalized with other receptor groups have also been prepared by the Zhao group to show sensing functions for fluoride ion, metal cations, and fullerenes.

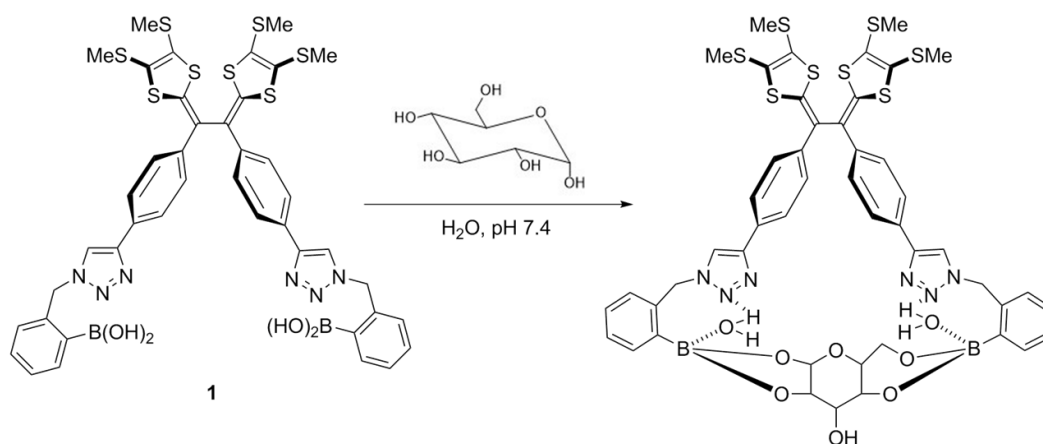


Figure 1.3: Binding of TTFV-phenylboronic acid molecular tweezer **1** to a saccharide molecule in water. Reprinted with permission from Ref. [18]. Copyright [2017], with permission from Elsevier.

### 1.2.2 TTFV-based Redox-active Ligands

Rigid  $\pi$ -conjugated systems with pyridinyl and carboxyl groups exhibit strong ability to coordinate with transition metal ions. Through such metal-ligand interactions, a huge number of metal/organic hybrid materials have been developed. In recent years, the assembly of micro/mesoporous metal organic frameworks (MOFs) has become a hot research topic, owing to the remarkable structural and surface properties of MOFs and their fascinating applications in energy storage, catalysis, and chemical sensing [25].

Redox-active ligands for metal ions have been regarded as very useful building blocks for the design and fabrication of novel organic-metal nanomaterials. In the literature, TTF-based ligands have been often used to complex with various metal ions, bringing redox-activity to the metal-organic hybrid systems. The use of TTFVs in this field has not yet been well developed. In 2010 Lorcy's group reported the TTFV-based redox-active metal-organic complex **2** (see Figure 1.4) [16]. In the structure of **2**, two TTF molecules with pyridyl substituents are coordinated with  $\text{Mo}(\text{CO})_6$  to form a cyclic complex. Single crystal X-ray diffraction analysis reveals a square-shaped cluster in which the TTFV moieties adopt a *cis*-like molecular shape. In a sense, the TTFV unit presents a pre-organized building block facilitating the assembly of cyclic complexes with Mo ions. Another TTFV-based redox-active ligand was recently reported by Wang and Zhao (see compound **3** in Figure 1.4). The TTFV molecule was designed with two carboxyl end groups, through which coordination with Zn(II) ions was achieved, resulting in redox-active TTFV-Zn polymers.

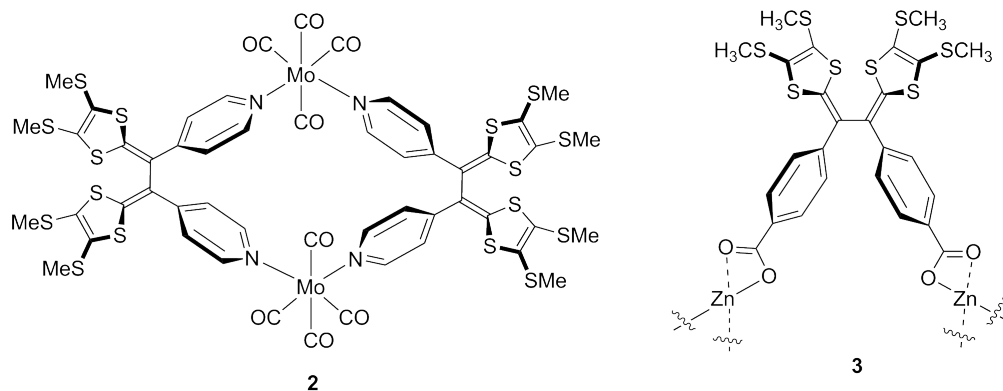


Figure 1.4: Redox-active Mo-TTFV complex **2** and Zn-TTFV complex **3**. Reprinted with permission from Ref. [16,26]. Copyright [2017], with permission from American Chemical Society and Beilstein Journal of Organic Chemistry.

### 1.3 Organic Semiconductor/Metal Interfaces

The knowledge of the interactions between organic molecules and metal surfaces and their electronic structures is of fundamental importance for the functions of organic electronic devices. Depending on the functions, organic electronic devices can be of different types, such as organic light-emitting diodes (OLEDs), field-effect transistors (FETs), and photovoltaic (PV) cells. Most of these devices are constructed in a typical layout, where a thin film of an organic semiconductor is used as active material for rectification and illumination (OLEDs), current modulation (OFETs), or solar energy conversion (PV cells). Figure 1.5 illustrates the architecture of an OFET. Compared to their inorganic counterparts, organic semiconductors show some advantages; for example, they have very good processability in solution and their properties can be easily tailored through rational chemical synthesis.

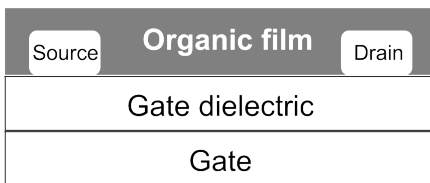


Figure 1.5: Schematic illustration of an OFET.

The self-organization of a single layer of organic molecules on the surface of a well-ordered metal substrate can significantly alter surface properties. For instance, strong charge transfer to the metal is caused by chemisorption of organic structures, which are referred to as the self-assembled monolayers (SAMs). The electronic interactions between the orbital of molecules and the substrate play a key role in tuning the electronic properties at the interface. Simulations of single-molecule adsorption on the metal surface can tell whether the organic-metal interactions are either due to weak van der Waals attraction or strong chemical bonding. On the other hand, organic molecules with  $\pi$ -conjugated structures have been found to show complicated adsorption behaviour on metal surfaces, with both van der Waals interaction and static polarization involved.

An important issue about the organic/metal interface is the energy level alignment, which can be described by two models, namely Schottky-Mott limit and Fermi-level pinning. In the first model, the molecular energy levels are determined by the metal work function, while in the second model, the molecular energy levels are defined relative to the Fermi energy of metal in which charge transfer occurs between adsorbent and substrate. Neither of these models can explain the complicated adsorptions such as the organic/metal interfaces that are involved in the chemisorption, charge transfer, dipole induced at the interface and geometry change induced by adsorption. It is also worth noting that the weak interactions between organic molecules and metal substrates should be considered in order to describe the energy alignment of the interface in an accurate way.

Quantum chemical calculation has been employed to understand the electronic structure of organic/metal interfaces by evaluating the electronic levels, work functions, and charge densities. Density functional theory (DFT) using the periodic boundary condition is a commonly used approach to simulate the adsorption of an

organic molecule on a metal surface that consists of a few layers of metal atoms. The unit cell of the adsorbent molecules and the slab are periodically repeated in two dimensions. A vacuum is assumed on the top of adsorbent to restrain the electronic interactions between surfaces.

Studies of the polycyclic aromatic hydrocarbons (PAHs) adsorbed on the surfaces of copper and gold show that the charge rearrangement is proportional to the distance between positively and negatively accumulated charges, which is decreased by reducing the size of the PAH molecule [27]. In another work, the effect of van der Waals interactions on the work function of gold and highly ordered pyrolytic graphite (HOPG) substrates was investigated. The results show that the work function of the substrate is decreased due to the formation of a cobalt(II) octaethylporphyrin monolayer [28].

In 2008 Hofmann and co-workers reported the use of TTF derivatives to tune the work function of a copper substrate [29]. DFT calculations in the periodic condition and generalized gradient approximation (GGA) were used to simulate the adsorption of TTF on the (110) surfaces of gold and silver by Martorell *et al.* in 2009 [30]. The adsorption of TTF and tetraselenofulvene on the surface of Ag (110) was studied by the same group in 2011 [31]. The molecule was predicted to assume a parallel adsorption orientation on the metal surface. Furthermore, simulated vibrational modes of adsorbent on the surface of the metal were reported in this work. The adsorption of TTF on the gold surface was compared against that on the silver surface. Charge transfer from TTF to the slab was found in that work. The formation of TTF SAMs on the surface of copper was studied by Wang *et al.* in 2011, which shows that the molecules tilt along the chain at maximum molecule-molecule interactions [32]. The thin film formation of TTF on the surface of Cu (110) was experimentally and computationally investigated by Sarasola *et al.* in 2014 [33]. Results show that the tilted

adsorption mode leads to stronger binding to the surface at low temperature, which is no longer stable at temperatures slightly above room temperature. Adsorption of a  $\pi$ -extended TTF on the surface of copper was investigated to understand the changes of electronic levels by Schuler *et al.* in 2014 [34]. Adsorption of a dihydro-TTF on the gold surface was computationally studied by Jethwa *et al.* in 2014 [35]. Their results show that each thiolate endgroup binds to a single gold atom, and there is a small degree of charge transfer between the molecule and the substrate. Compared with the well-studied TTF and related derivatives, little work has been devoted to understanding the behavior of DTF molecules adsorbed on the metal surface. More systematic studies in this direction are thus warranted.

## 1.4 Gold Nanoparticles: Synthesis and Properties

Metal nanoparticles with sizes ranging from 1–100 nm display properties that are very different from those of bulk materials or single atoms [36]. Large surface area and high surface energy are the two main features of nanoparticles [37]. Metal nanoparticles can be prepared at relatively low costs to attain remarkable controllability and high tunability in terms of dimension, shape, and functionality. As such, they have been widely recognized as promising nanomaterials for developing new technologies, such as bio-imaging, photocatalysis, and nanoscale optoelectronic devices [38].

Among numerous types of metal nanoparticles, gold nanoparticles (AuNPs) are the ones showing the most intriguing properties and applicability. Enormous research activity has been dedicated to the rational design and tailoring of AuNPs over the past few decades. So far, a large array of functionalized AuNPs has been successfully applied in various areas, such as memory storage [39], semiconductor films [40], biological detectors [36], monitoring of biomolecular events [41], catalysis, and sen-

sors [42], just to name a few. It is worth noting that AuNPs usually show very low toxicity or even non-toxicity, which make them particularly useful in biological and medicinal applications [36].

Synthetically, the preparation of AuNPs with defined shapes and dimensions can be attained by tuning various parameters; for example, the type of ligands encapsulating AuNPs plays a key role in dictating the shape and size of AuNPs [43]. In addition, the morphological features of AuNPs are also significantly influenced by synthetic conditions, such as solvent, temperature, and pH. The formation of AuNPs involves two key steps, namely nucleation and growth, which have a direct impact on the final morphology of AuNPs. Nucleation is the process in which preliminary seeds act as nuclei and template for the formation of nanometer-size particles, while growth is the process in which other atoms accumulate on the nuclei to increase the size of the particle. Herein, nuclei refers to the arrangement of very few Au(0) atoms that can grow by deposition of additional atoms over the surface [44]. The formation of colloids through “burst nucleation” was first proposed and investigated by Lamer *et al.* in 1940. Burst nucleation considers the nucleation and growth as separate process. In other words, there is no nucleation occurring during the growth step. After growth, AuNPs are formed with an even distribution of the size and shape [44]. The nucleation and growth processes are then modeled and described by classical nucleation theory and Ostwald ripening, followed by Lifshitz-Slyozov-Wagner (LSW) theory [45, 46]. The origin of Ostwald ripening theory comes from the lower energy of smaller particles with a higher surface to volume ratio. The outer layer of a nanoparticle is found to be at higher energy than the inner atoms. Therefore, the Ostwald ripening is a thermodynamically favored phase-transformation process from liquid to solid, by which monomers adsorb to the surface of solid to produce a more stable species.

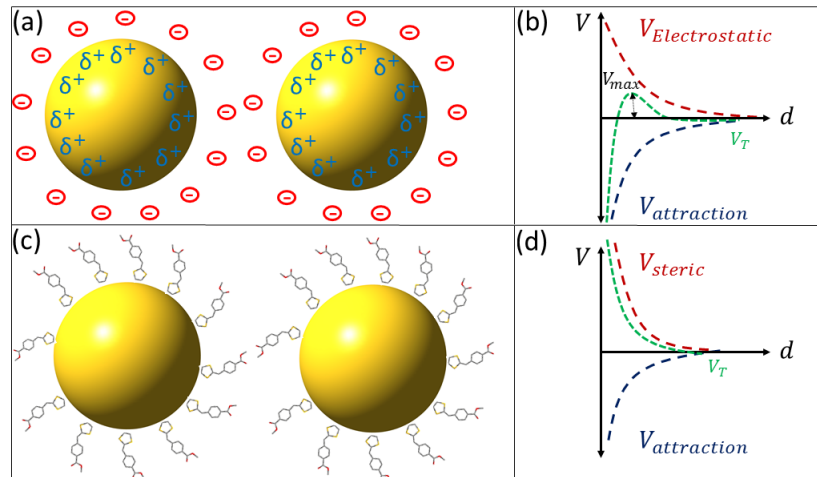


Figure 1.6: (a) The electrostatic stabilization of neighboring metal particles that are approaching together until the surface to surface distance becomes larger than the particle's double layer. (b) The potential energy as a function of the surface to surface distance is plotted, which exhibits the dominance of repulsion forces before the maximum total potential. The total potential tends to a stronger van der Waals force by further decreasing the distance by agglomeration. The dashed green line represent the total potential as the sum of repulsive and attractive forces. (c) Schematic of steric stabilization of nanoparticles by coating with the layer of anchoring polymer. (d) The neighboring particles experience strong repulsive forces when particles are closer than the anchored layer.

### 1.4.1 Stabilization and Controlled Growth of AuNPs

As mentioned earlier, the large surface area to the volume ratio endows AuNPs with excellent properties in comparison to bulk materials. The high surface energy, on the other hand, makes AuNPs show strong tendency towards agglomeration or coagulation [44]. To prevent this from happening, some means of stabilization must be introduced during the formation of AuNPs. Different methods of stabilizing AuNPs have been developed and investigated, in which the polymeric effect, electrostatic effect, and pH effect are the most commonly used parameters for fine-tuning the stabilizing outcomes [44, 47].

The electrostatic effect is based on the repulsion of like charges that surround the surface of nanoparticles at the double layer region (Figure 1.6A). The double layer is

the charge redistribution over the surface of a particle due to the electrostatic attraction between the particle and surrounding charged species (solvent molecules and/or electrolytes). The classic illustration of electrostatic effect on a particle's stabilization was first proposed by Derjaguin, Landau, Verwey and Overbeek (DLVO) in 1940. The DLVO theory considers ions as points of charges with a uniform distribution which is supposed to decrease the speed of particle agglomeration with no dependency on the type of ion. The total potential energy of two interacting particles is assumed to be the sum of attracting forces (e.g., van der Waals) and repulsive forces [37, 47, 48].

A plot of potential energy versus the distance between two approaching metal particles is shown in Figure 1.6B, in which  $V_T$  (dashed green line) is the sum of repulsion and van der Waals attraction potentials [49]. The repulsive potential is higher than the attractive force when two particles are far away from each other. However, the total potential starts to gradually increase by reducing the surface to surface distance. The repulsive force becomes dominant until it reaches the maximum potential at  $V_{max}$ . The maximum potential is the energy barrier. After going through it the van der Waals force becomes dominant [37].

The electrostatic layer can be experimentally evaluated by zeta potential and is essentially influential in the dilute system [37, 49]. The different chemical nature of charged particles can result in more complex charge rearrangement over the surface of nanoparticles [37]. According to the DVLO theory, higher potential energy leads to more stabilization of nanoparticles. Higher kinetic energy, on the other hand, increases the coagulation of interacting particles. Therefore, the stability of the particles cannot be only ascribed to the electrostatic effect as described in the DVLO theory. Charge redistribution or polarization effects are contributive to the strength of electrostatic forces between a neutral metal particle and a point of charge where there is no chemical interaction [37]. The partial positive charge can be distorted

upon approaching another positively charged particle, inducing an electric dipole moment in the metal particle. Shortening the distance between an external charge and the surface of a metal particle increases the induced dipole moment and hence the attractive force between them.

Coating metal nanoparticles with a tight layer of polymers or surfactant molecules prevents the nanoparticles from aggregation, providing another approach for stabilization of nanoparticles. As can be seen in Figure 1.6C, the layers repel the surrounded coated particles due to steric hindrance and make the particles resistant to deformation. The repulsive forces have been found to be exponentially proportional to the interparticle distance (Figure 1.6D) [50]. The neighboring particles experience strong repulsive forces when the particles come within a distance shorter than the total thickness of coating layers. Binding of polymers to the surface of metal particles can be achieved through covalently anchoring the end functional groups of polymers to the surface, or simply by adsorption of the polymers on the surface. The adsorption is due to relatively weak non-covalent interactions, in which polymers randomly wrap their backbones around the nanoparticles [37, 44]. Polymers with higher molecular weights and stronger chelating ability can encapsulate and stabilize metal nanoparticles more efficiently. In general, electron donating ligand groups, such as sulfur, nitrogen, and aromatic rings with loosely bound  $\pi$ -electrons can interact effectively with metal surfaces in particular those with partial positive charges [44, 51, 52].

### 1.4.2 Mechanisms of AuNP Formation

Many methods have been proposed for the preparation of colloidal noble metal nanoparticles in solution during the last three decades. A commonly used strategy is to reduce corresponding metal salts by a suitable reducing agent in the presence of the surfactants. The nature of surfactant controls the size and morphology of the resulting

nanoparticles. Colloidal AuNPs can be prepared by adding a reducing agent to a solution of  $\text{HAuCl}_4$  under stirring. A stabilizing agent is used to encapsulate the formed particles to prevent the aggregation of nanoparticles. The nanoparticle nucleation begins with the reduction of the Au(III) to Au(I) (equation 1.1), which is followed by the formation of Au(0) seeds. Nanoparticle seeds are surrounded by Au(I) species which will then reduce to Au(0) leading to an increase in the size of AuNPs [53].



In 1951 Turkevich developed the first synthesis of colloidal spherical AuNPs with an average size of  $200 \pm 15$  nm. In this method, trisodium citrate dihydrate ( $\text{Na}_3\text{C}_6\text{H}_5\text{O}_7 \cdot 2\text{H}_2\text{O}$ ) was added to a stirred solution of chloroauric acid ( $\text{HAuCl}_4$ ). The mixture was heated to  $100^\circ\text{C}$  to give a clear red solution which contained AuNPs encapsulated by the citrate anions. At the last stage of the synthesis, hydroxylamine hydrochloride ( $\text{NH}_3\text{OH}\cdot\text{HCl}$ ) was added to terminate the growth of the AuNPs with a desired average size [54]. The stability of AuNPs prepared with the Turkevich method originates from the electrostatic effect; citrate ions carrying negative charges are deposited on the surface of AuNPs to engender repulsion between the particles [47]. In 1998 Henglein devised a method to convert Au(I) to AuNPs through a radiochemical reaction [55]. In 2006, a revisited Turkevich's method was reported by Kimling and co-workers, in which ascorbic acid and cetyltrimethylammonium bromide (CTAB) were used as the stabilizing agent and surfactant, respectively [56].

A strong ionic environment can significantly enhance the electrostatic stability of AuNPs due to the charge transfer from ions to the surface of AuNPs [47]. Merk and co-workers studied the effect of the polarizability of ions on AuNP formation in 2013 [48]. Their results clearly indicate that the colloidal stability of ligand-free AuNPs can be

improved with increasing the polarizability of ions. In the current literature, there are numerous publications on mechanistic studies of AuNP formation, but knowledge on the detailed steps involved in the actual process of AuNP growth is still quite limited [44].

### 1.4.3 Functionalization and Application of AuNPs

Surface functionalization is a powerful technique for tailoring and controlling the properties of AuNPs [44]. The large surface area of AuNPs allows a variety of functional molecular moieties to be introduced to the AuNP systems, which in turn bring about new features useful to many applications [36]. For example, AuNPs functionalized with specific receptors can act as highly efficient chemical and biological sensors. Certain biologically active functional groups can be attached to AuNPs to dictate the destinations and fates of AuNPs in a biological system [57]. Such functionalized AuNPs are useful in the application of bio-imaging, bio-diagnosis, and targeted drug delivery [58]. AuNPs in combination with conjugated polymers and dendrimers can boost the efficiency of organic solar cells [59].

Thiol is a commonly used anchoring group for linking various organic/inorganic functional groups to the surface of AuNPs, owing to its relatively high affinity for gold (i.e., covalent bonding). Functionalization of AuNPs with thiol derivatives can overcome the stability issue that colloidal AuNPs usually face. Thiol-functionalized AuNPs were first reported by Brust in 1994 [60]. The Brust method yields AuNPs throughout the reduction of  $\text{HAuCl}_4$  in the presence of sodium borohydrate and dodecanethiol. A year later, Brust and co-workers developed a method to functionalize AuNPs with *p*-mercaptophenol, which is a more stable thiol ligand than alkylthiols [61]. The IR spectra of the *p*-mercaptophenol before and after reaction with tetrachloroaurate ions were examined to clearly show the absence of the S–H stretch-

ing band at  $2600\text{ cm}^{-1}$  and the presence of free hydroxyl group. They concluded that the molecules were self-assembled on the surface of AuNPs through thiol groups. The studies by Brust established a simple synthetic procedure for air stable functionalized AuNPs. Nitrogen-based surfactants were used to facilitate the transfer of  $\text{HAuCl}_4$  from water to the organic phase to further redox reactions; however, they tend to cover the surface of formed AuNPs and hence require an extra effort of purification [62,63]. Sarathy *et al.* reported a novel procedure for the synthesis of gold nanostructures that are derivatized with the dodecanethiol group. In their method, the nitrogen-containing phase transfer agent was replaced by hydrochloric acid to facilitate the transfer of Au to the organic layer containing the thiol compounds [62,64]. X-ray photoelectron (XPS) spectroscopy confirmed that the sulfur atoms were chemisorbed on the surface of Au. Modification of the AuNP surface with thionicotinamide upon laser excitation was reported by Fujiwara *et al.* in 1999 [65]. Their results indicated that the AuNPs end-capped with thionicotinamide groups underwent physical changes such as coagulation or dissolution upon laser radiation. As such, the characteristic UV-Vis peak of AuNPs at 520 nm was shifted to higher wavelength due to coagulation of AuNPs. Yee *et al.* reported a monophasic synthesis of functionalized spherical AuNPs packed in the fcc arrangement. Octadecanethiol and lithium triethylborohydride were used as the surfactant and reducing agent in THF solution [63].

In 1999 Nakai *et al.* synthesized a class of stable functionalized AuNPs functionalized with tetrathiafulvalene (TTF) derivatives [66]. Zhou and co-workers reported a redox reaction between  $\text{HAuCl}_4$  and poly(dithiafulvene)s in 2001, which gave AuNPs with an average size of 6 nm [67]. The AuNPs were found to be stable for more than a month with the narrow size distribution well kept. TTF compounds were also used to synthesize silver nanostructures in acetonitrile by Wang *et al.* in 2003 [68]. The TEM images of these silver particles showed a dendritic shape. Wang investigated the

reduction of Au ions to AuNPs through oxidation of a prepared layer-by-layer self-assembled film of poly(dithiafulvene)s on an ITO substrate in 2006 [69]. Dithiafulvene derivatives were used by Lanterna in 2015 to reduce Au(III) to Au(0), resulting in stable AuNPs without the need for any other reducing agents [70].

## 1.5 Motivation and Organization of This Thesis

1,4-Dithiafulvene (DTF) and tetrathiafulvalene (TTF) functionalized oligomers are a promising group of  $\pi$ -conjugated materials with excellent electron-donating and redox properties. They are particularly useful in the application of thin-film molecular electronic and optoelectronic devices as the active materials [71]. The thesis work is aimed at understanding the fundamental properties of a series of novel DTF-based molecules and macromolecules. In particular the structural, electronic, and microscopic properties of these compounds in the forms of self-assembled monolayers (SAMs) on the surface of Au (111) or AuNPs were investigated. Molecular modeling in the gas phase and the solid state was conducted through density functional theory (DFT) calculations, and the computational results were compared with various experimental data such as Raman spectroscopy, atomic force microscopy (AFM), and ultraviolet-visible (UV-Vis) spectroscopy to establish some understanding of structure-property relationships.

The first part of this thesis focuses on the structural and electronic properties of bis(DTF)-endcapped oligo(phenylene ethynylene)s in the neutral and oxidized forms. The self-assembling properties of the oligomers in different redox states were examined on mica and highly oriented pyrolytic graphite (HOPG) surfaces to show dependency of thin film morphology on oxidation state. In the second part, the adsorption behaviour of a carboxylated DTF molecule on the surface of Au was studied by DFT

calculations with the Vienna Ab initio Simulation Package (VASP) under periodic boundary conditions with Perdew-Burke-Ernzerhof (PBE) correlation and generalized gradient approximation (GGA) exchange functional and considering the effect of van der Waals interaction by using the vdW-DFT (optB88-vdW) method. First, the role of molecule-gold interaction is discussed with regards to the effect of monolayer formation on charge transfer. Second, the effect of van der Waals interactions on metal organic interface is elucidated by comparison of the computational results with and without dispersion correction. Raman spectroscopy and Kelvin probe force microscopy (KPFM) were employed to evaluate the accuracy of the computed workfunctions. The results show that the workfunction of Au (111) can be tuned by deposition of an aryl-substituted DTF film of varying polarity. In the final part, the mechanism for the reduction of  $\text{HAuCl}_4$  with DTF derivatives is discussed based on time-dependent UV-Vis analysis. The study discloses a promising one-phase synthetic approach for AuNPs in aqueous media, where stepwise temperature control has been found to exert a key effect on the synthetic outcomes.

## Bibliography

- [1] Fred Wudl, Darold Wobschall, and Earl J. Hufnagel. Electrical conductivity by the bis(1,3-dithiole)-bis(1,3-dithiolium) system. *J. Am. Chem. Soc.*, 94:670–672, 1972.
- [2] Yuming Zhao, Guang Chen, Karimulla Mulla, Ilias Mahmud, Shuai Liang, Praateek Dongare, David W. Thompson, Louise N. Dawe, and Stephen Bouzan. Tetrathiafulvalene vinylogues as versatile building blocks for new organic materials. *Pure Appl. Chem.*, 84:1005–1025, 2012.

- [3] Kathleen Woolridge, Luana C. Goncalves, Stephen Bouzan, Guang Chen, and Yuming Zhao. Aryl-substituted dithiafulvenes: synthesis, electronic properties, and redox reactivity. *Tetrahedron Lett.*, 55:6362 – 6366, 2014.
- [4] Dominique de Caro, I Malfant, J-P Savy, and L Valade. A review of molecule-based conductors electrodeposited as thin films on silicon wafers. *J. Phys. Condens. Matter*, 20:184012, 2008.
- [5] Henning Hopf and M. S. Sherburn. *Cross conjugation: dendralene, radialene and fulvene chemistry*. Wiley-VCH, 2016.
- [6] Olivier Alévêque, Pierre Frère, Philippe Leriche, Tony Breton, Antonio Cravino, and Jean Roncali. Effects of aromatic spacers on the properties of organic field effect transistors based on  $\pi$ -extended tetrathiafulvalene derivatives. *J. Mater. Chem.*, 19:3648–3651, 2009.
- [7] Georg Heimel, Lorenz Romaner, Jean-Luc Brédas, and Egbert Zojer. Interface energetics and level alignment at covalent metal-molecule junctions:  $\pi$ -conjugated thiols on gold. *Phys. Rev. Lett.*, 96:196806, 2006.
- [8] Rafal Klajn, J. Fraser Stoddart, and Bartosz A. Grzybowski. Nanoparticles functionalised with reversible molecular and supramolecular switches. *Chem. Soc. Rev.*, 39:2203–2237, 2010.
- [9] Philippe Hapiot, Dominique Lorcy, André Tallec, Roger Carlier, and Albert Robert. Mechanism of dimerization of 1,4-dithiafulvenes into TTF vinylogues. *J. Phys. Chem.*, 100:14823–14827, 1996.
- [10] Pierre Frere and Peter J. Skabara. Salts of extended tetrathiafulvalene analogues: relationships between molecular structure, electrochemical properties and solid state organisation. *Chem. Soc. Rev.*, 34:69–98, 2005.

- [11] Marcos Chas, Margareth Lemarie, Mihaela Gulea, and Narcis Avarvari. Chemo- and enantioselective sulfoxidation of bis(ethylenedithio)-tetrathiafulvalene (BEDT-TTF) into chiral BEDT-TTF-sulfoxide. *Chem. Commun.*, pages 220–222, 2008.
- [12] J. L. Brédas, J. P. Calbert, D. A. da Silva Filho, and J. Cornil. Organic semiconductors: a theoretical characterization of the basic parameters governing charge transport. *Proc. Natl. Acad. Sci.*, 99:5804–5809, 2002.
- [13] Diego Paschoal and Hélio F. Dos Santos. Assessing the quantum mechanical level of theory for prediction of linear and nonlinear optical properties of push-pull organic molecules. *J. Mol. Model.*, 19:2079–2090, 2013.
- [14] G.H. Wagniere. *Linear and nonlinear optical properties of molecules*, volume 99. Wiley-VCH, 1995.
- [15] Richard J. D. Tilley. *Colour and the optical properties of materials: an exploration of the relationship between light, the optical properties of materials and colour*. Wiley, second edition, 2011.
- [16] Elodie Gontier, Nathalie Bellec, Pierre Brignou, Arnaud Gohier, Michel Guerro, Thierry Roisnel, and Dominique Lorcy. Pyridyldithiafulvenes as precursors of coordination-driven self-assembled redox active macrocycle. *Org. Lett.*, 12:2386–2389, 2010.
- [17] Michel Guerro, Ngoc Ha Pham, Julien Massue, Nathalie Bellec, and Dominique Lorcy. New redox active ligands involving a tetrathiafulvalene vinylogue backbone. *Tetrahedron*, 64:5285–5290, 2008.
- [18] Karimulla Mulla and Yuming Zhao. TTFV molecular tweezers with phenylboronic acid and phenylboronate endgroups: modular synthesis and electrochem-

- ical responses to saccharides and fluoride ion. *Tetrahedron Lett.*, 55:382–386, 2014.
- [19] Dominique Lorey, Michel Guerro, Jean-François Bergamini, and Philippe Hapiot. Vinylogous tetrathiafulvalene based podands: complexation interferences on the molecular movements triggered by electron transfer. *J. Phys. Chem. B*, 117:5188–5194, 2013.
- [20] Karimulla Mulla, Prateek Dongare, David W. Thompson, and Yuming Zhao. Click synthesized dianthryl-TTFV: an efficient fluorescent turn-on probe for transition metal ions. *Org. Biomol. Chem.*, 10:2542–2544, 2012.
- [21] Karimulla Mulla, Haseena Shaik, David W Thompson, and Yuming Zhao. TTFV-based molecular tweezers and macrocycles as receptors for fullerenes. *Org. Lett.*, 15:4532–4535, 2013.
- [22] Shuai Liang, Yuming Zhao, and Alex Adronov. Selective and reversible noncovalent functionalization of single-walled carbon nanotubes by a pH-responsive vinylogous tetrathiafulvalene–fluorene copolymer. *J. Am. Chem. Soc.*, 136:970–977, 2014.
- [23] Guang Chen, Ilias Mahmud, Louise N Dawe, and Yuming Zhao. Acetylenic phenyldithiafulvene: a versatile synthon for TTFV-based macromolecules. *Org. Lett.*, 12:704–707, 2010.
- [24] Emilie Ripaud, Philippe Leriche, Nicolas Cocherel, Thomas Cauchy, Pierre Frere, and Jean Roncali. Tristhienylphenylamine - extended dithiafulvene hybrids as bifunctional electroactive species. *Org. Biomol. Chem.*, 9:1034–1040, 2011.

- [25] Lauren E. Kreno, Kirsty Leong, Omar K. Farha, Mark Allendorf, Richard P. Van Duyne, and Joseph T. Hupp. Metal–organic framework materials as chemical sensors. *Chem. Rev.*, 112:1105–1125, 2012.
- [26] Yunfei Wang and Yuming Zhao. Carboxylated dithiafulvenes and tetrathiafulvalene vinylogues: synthesis, electronic properties, and complexation with zinc ions. *Beilstein J. Org. Chem.*, 11:957–965, 2015.
- [27] Paulo V.C. Medeiros, G.K. Gueorguiev, and S. Stafström. Bonding, charge rearrangement and interface dipoles of benzene, graphene, and PAH molecules on Au(111) and Cu(111). *Carbon*, 81:620 – 628, 2015.
- [28] Bhaskar Chilukuri, Ursula Mazur, and K. W. Hipps. Effect of dispersion on surface interactions of cobalt(ii) octaethylporphyrin monolayer on Au(111) and HOPG(0001) substrates: a comparative first principles study. *Phys. Chem. Chem. Phys.*, 16:14096–14107, 2014.
- [29] Oliver T. Hofmann, Gerold M. Rangger, and Egbert Zojer. Reducing the metal work function beyond pauli pushback: a computational investigation of tetrathiafulvalene and viologen on coinage metal surfaces. *J. Phys. Chem. C*, 112:20357–20365, 2008.
- [30] Benjamí Martorell, Anna Clotet, and Jordi Fraxedas. A first principle study of the structural, vibrational and electronic properties of tetrathiafulvalene adsorbed on Ag(110) and Au(110) surfaces. *J. Comput. Chem.*, 31:1842–1852, 2010.
- [31] B. Martorell, J. Fraxedas, and A. Clotet. Tetrathia- and tetraselenafulvalene adsorbed on Ag(110): a theoretical study. *Surf. Sci.*, 605:187–192, 2011.
- [32] Yang Wang, Christian Urban, Jonathan Rodríguez-Fernández, José M. Gallego, Roberto Otero, Nazario Martín, Rodolfo Miranda, Manuel Alcamí, and Fernando

- Martín. Formation of self-assembled chains of tetrathiafulvalene on a Cu(100) surface. *J. Phys. Chem. A*, 115:13080–13087, 2011.
- [33] Ane Sarasola, Sara Barja, Amadeo L. Vázquez de Parga, and Andrés Arnau. Adsorption of tetrathiafulvalene (TTF) on Cu(100): can  $\pi$ -stacked 1-D aggregates be formed at low temperature? *Chem. Phys. Lett.*, 612:45–50, 2014.
- [34] Bruno Schuler, Shi-Xia Liu, Yan Geng, Silvio Decurtins, Gerhard Meyer, and Leo Gross. Contrast formation in Kelvin probe force microscopy of single  $\pi$ -conjugated molecules. *Nano Lett.*, 14:3342–3346, 2014.
- [35] Siddharth J. Jethwa, Federico Grillo, Herbert A. Fruchtl, Grant J. Simpson, Michael-John Treanor, Renald Schaub, Stephen M. Francis, Neville V. Richardson, and R. Alan Aitken. Adsorption of a dihydro-TTF derivative on Au(111) via a thiolate complex bonding to gold adatoms. *Chem. Commun.*, 50:10140–10143, 2014.
- [36] Lucas A. Lane, Ximei Qian, and Shuming Nie. SERS nanoparticles in medicine: from label-free detection to spectroscopic tagging. *Chem. Rev.*, 115:10489–10529, 2015.
- [37] Scott Handy. *Applications of ionic liquids in science and technology*. InTech, 2011.
- [38] Susie Eustis and Mostafa A. El-Sayed. Why gold nanoparticles are more precious than pretty gold: Noble metal surface plasmon resonance and its enhancement of the radiative and nonradiative properties of nanocrystals of different shapes. *Chem. Soc. Rev.*, 35:209–217, 2006.

- [39] Peng Cui, Sohyeon Seo, Junghyun Lee, Luyang Wang, Eunkyo Lee, Misook Min, and Hyoyoung Lee. Nonvolatile memory device using gold nanoparticles covalently bound to reduced graphene oxide. *ACS Nano*, 5:6826–6833, 2011.
- [40] Robert G. Palgrave, , and Ivan P. Parkin. Aerosol assisted chemical vapor deposition using nanoparticle precursors: a route to nanocomposite thin films. *J. Am. Chem. Soc.*, 128:1587–1597, 2006.
- [41] Sajanalal R. Panikkanvalappil, Steven M. Hira, Mahmoud A. Mahmoud, and Mostafa A. El-Sayed. Unraveling the biomolecular snapshots of mitosis in healthy and cancer cells using plasmonically-enhanced Raman spectroscopy. *J. Am. Chem. Soc.*, 136:15961–15968, 2014.
- [42] Yuanchao Zhang, Wendy Chu, Alireza Dibaji Foroushani, Hongbin Wang, Da Li, Jingquan Liu, Colin J. Barrow, Xin Wang, and Wenrong Yang. New gold nanostructures for sensor applications: a review. *Materials*, 7:5169, 2014.
- [43] Helmut Hinterwirth, Stefanie Kappel, Thomas Waitz, Thomas Prohaska, Wolfgang Lindner, and Michael Lämmerhofer. Quantifying thiol ligand density of self-assembled monolayers on gold nanoparticles by inductively coupled plasma-mass spectrometry. *ACS Nano*, 7:1129–1136, 2013.
- [44] Pedro H. C. Camargo, Thenner S. Rodrigues, Anderson G. M. da Silva, and Jiale Wang. *Controlled synthesis: nucleation and growth in solution*. Springer International Publishing, 2015.
- [45] Jörg Polte, T. Torsten Ahner, Friedmar Delissen, Sergey Sokolov, Franziska Emerling, Andreas F. Thünemann, and Ralph Kraehnert. Mechanism of gold nanoparticle formation in the classical citrate synthesis method derived from

- coupled in situ XANES and SAXS evaluation. *J. Am. Chem. Soc.*, 132:1296–1301, 2010.
- [46] Taylor J. Woehl, James E. Evans, Ilke Arslan, William D. Ristenpart, and Nigel D. Browning. Direct in situ determination of the mechanisms controlling nanoparticle nucleation and growth. *ACS Nano*, 6:8599–8610, 2012.
- [47] Christian Pfeiffer, Christoph Rehbock, Dominik Hühn, Carolina Carrillo-Carrion, Dorleta Jimenez de Aberasturi, Vivian Merk, Stephan Barcikowski, and Wolfgang J. Parak. Interaction of colloidal nanoparticles with their local environment: the (ionic) nanoenvironment around nanoparticles is different from bulk and determines the physico-chemical properties of the nanoparticles. *J. R. Soc. Interface*, 11, 2014.
- [48] Vivian Merk, Christoph Rehbock, Felix Becker, Ulrich Hagemann, Hermann Nienhaus, and Stephan Barcikowski. In situ non-DLVO stabilization of surfactant-free, plasmonic gold nanoparticles: effect of hofmeisteres anions. *Langmuir*, 30:4213–4222, 2014.
- [49] Yaovi Holade, Nihat Ege Sahin, Karine Servat, Teko W. Napporn, and Kouakou B. Kokoh. Recent advances in carbon supported metal nanoparticles preparation for oxygen reduction reaction in low temperature fuel cells. *MDPI, Catalyst*, 5:310–348, 2015.
- [50] Younjin Min, Mustafa Akbulut, Kai Kristiansen, and Yuval Golan & Jacob Israelachvili. The role of interparticle and external forces in nanoparticle assembly. *Nat. Mater.*, 7:527–538, 2008.

- [51] Makoto Takafuji, Shunichi Ide, Hirotaka Ihara, and Zhenghe Xu. Preparation of poly(1-vinylimidazole)-grafted magnetic nanoparticles and their application for removal of metal ions. *Chem. Mater.*, 16:1977–1983, 2004.
- [52] Marie-Christine Daniel, , and Didier Astruc. Gold nanoparticles: assembly, supramolecular chemistry, quantum-size-related properties, and applications toward biology, catalysis, and nanotechnology. *Chem. Rev.*, 104:293–346, 2004.
- [53] J.R. Mycroft, G.M. Bancroft, N.S. McIntyre, and J.W. Lorimer. Spontaneous deposition of gold on pyrite from solutions containing Au (III) and Au (I) chlorides. Part I: A surface study. *Geochimica et Cosmochimica Acta*, 59(16):3351 – 3365, 1995.
- [54] John Turkevich, Peter Cooper Stevenson, and James Hillier. A study of the nucleation and growth processes in the synthesis of colloidal gold. *Discuss. Faraday Soc.*, 11:55–75, 1951.
- [55] Arnim Henglein and Dan Meisel. Radiolytic control of the size of colloidal gold nanoparticles. *Langmuir*, 14:7392–7396, 1998.
- [56] J. Kimling, M. Maier, B. Okenve, V. Kotaidis, H. Ballot, , and A. Plech. Turkevich method for gold nanoparticle synthesis revisited. *J. Phys. Chem. B*, 110:15700–15707, 2006.
- [57] Yi-Cheun Yeh, Brian Creran, and Vincent M. Rotello. Gold nanoparticles: preparation, properties, and applications in bionanotechnology. *Nanoscale*, 4:1871–1880, 2012.
- [58] Mazaher Gholipourmalekabadi, Mohammadmahdi Mobaraki, Maryam Ghaffari, Amir Zarebkohan, Vahid F. Omrani, Aleksandra M. Urbanska, and Alexander

- Seifalian. Targeted drug delivery based on gold nanoparticle derivatives. *Curr. Pharm. Des.*, 23:2918–2929, 2017.
- [59] Sai-Anand Gopalan, Anantha-Iyengar Gopalan, Ajayan Vinu, Kwang-Pill Lee, and Shin-Won Kang. A new optical-electrical integrated buffer layer design based on gold nanoparticles tethered thiol containing sulfonated polyaniline towards enhancement of solar cell performance. *Sol. Energy Mater Sol. Cells*, 174:112 – 123, 2018.
- [60] Mathias Brust, Meryll Walker, Donald Bethell, David J. Schiffrin, and Robin Whyman. Synthesis of thiol-derivatised gold nanoparticles in a two-phase Liquid-Liquid system. *J. Chem. Soc., Chem. Commun.*, pages 801–802, 1994.
- [61] M. Brust, J. Fink, D. Bethell, D. J. Schiffrin, and C. Kiely. Synthesis and reactions of functionalised gold nanoparticles. *J. Chem. Soc., Chem. Commun.*, pages 1655–1656, 1995.
- [62] K. Vijaya Sarathy, G. U. Kulkarni, and C. N. R. Rao. A novel method of preparing thiol-derivatised nanoparticles of gold, platinum and silver forming superstructures. *Chem. Commun.*, pages 537–538, 1997.
- [63] Chanel K. Yee, Rainer Jordan, Abraham Ulman, Henry White, Alexander King, Miriam Rafailovich, and Jonathan Sokolov. Novel one-phase synthesis of thiol-functionalized gold, palladium, and iridium nanoparticles using superhydride. *Langmuir*, 15:3486–3491, 1999.
- [64] K. Vijaya Sarathy, Gargi Raina, R. T. Yadav, G. U. Kulkarni, , and C. N. R. Rao. Thiol-derivatized nanocrystalline arrays of gold, silver, and platinum. *J. Phys. Chem. B*, 101:9876–9880, 1997.

- [65] Hiroaki Fujiwara, Shozo Yanagida, and Prashant V. Kamat. Visible laser induced fusion and fragmentation of thionicotinamide-capped gold nanoparticles. *J. Phys. Chem. B*, 103:2589–2591, 1999.
- [66] Hidetaka Nakai, Masakuni Yoshihara, and Hisashi Fujihara. New electroactive tetrathiafulvalene-derivatized gold nanoparticles and their remarkably stable nanoparticle films on electrodes. *Langmuir*, 15:8574–8576, 1999.
- [67] Yong Zhou, Hideaki Itoh, Takashi Uemura, Kensuke Naka, and Yoshiki Chujo. Preparation of small  $\pi$ -conjugated polymer-protected gold nanoparticles in stable colloidal form. *Chem. Commun.*, pages 613–614, 2001.
- [68] Xiaqin Wang, Hideaki Itoh, Kensuke Naka, and Yoshiki Chujo. Tetrathiafulvalene-assisted formation of silver dendritic nanostructures in acetonitrile. *Langmuir*, 19:6242–6246, 2003.
- [69] Xiaqin Wang, Kensuke Naka, Chaosheng Wang, Hideaki Itoh, Takashi Uemura, and Yoshiki Chujo. Layer-by-layer films based on charge transfer interaction of  $\pi$ -conjugated poly(dithiafulvene) and incorporation of gold nanoparticles into the films. *J. Appl. Polym. Sci.*, 103:1608–1615, 2007.
- [70] Anabel E. Lanterna, Eduardo A. Coronado, and Alejandro M. Granados. Synthesis of gold nanoparticles using electron-donating dithiafulvene units. *Tetrahedron Lett.*, 56:4871 – 4876, 2015.
- [71] Atsushi Wachi, Yusuke Kudo, Aoba Kanesaka, Hiroyuki Nishikawa, Takuya Shiga, Hiroki Oshio, Masayuki Chikamatsu, and Reiko Azumi. Organic field-effect transistor based on paramagnetic Cu(II) neutral complexes coordinated by Schiff base-type TTF ligands. *Polyhedron*, 2017.

# Co-authorship Statement

Dithiafulvenes and tetrathiafulvalene derivatives were obtained from Prof. Yuming Zhao's research lab, which were synthesized and purified by Karimulla Mulla, Yunfei Wang, and Hadeel Adows.

The experimental work functions were measured with Kelvin probe force microscopy with the help of Abhijit Chatterjee, a Ph.D. student in Prof. Erika Merschrod's research group.

The designing of the procedure for AuNP synthesis and identification of the produced AuNPs at different pH were done through a collaborative study with Dr. Jiaqi Cheng in January 2015, who was a post-doctoral fellow in Prof. Merschrod's research group.

All computational work was conducted by Sepideh Mehrani including the choice of methods and parameters. The experimental protocols were designed and implemented by Sepideh Mehrani, with collaboration mentioned above. All chapters and appendices in this thesis were written by Sepideh Mehrani, with feedback and corrections from Profs. Zhao and Merschrod. Data analysis was developed and carried out by Sepideh Mehrani, with input from Profs. Zhao and Merschrod.

# Chapter 2

## Redox-dependent Properties of DTF-endcapped $\pi$ -Conjugated Oligomers

### 2.1 Introduction

Redox-active  $\pi$ -conjugated oligomers and polymers have been extensively investigated over the past few decades owing to their widespread uses in molecular electronic and optoelectronic materials and devices [1–4]. In the current literature, a large family of functional  $\pi$ -conjugated polymer structures has been established, wherein specially designed electron-donating and/or electron-withdrawing groups are either incorporated in the polymer backbones or grafted to the side chains, resulting in p- or n-type semiconducting  $\pi$ -conjugated materials for various molecular electronic and optical devices [5–8]. In this context, tetrathiafulvalene (TTF) and related  $\pi$ -analogues have constituted a popular class of building blocks for constructing functional organic electronic and optoelectronic materials, given their excellent electron-donating properties,

rich redox activity, and versatile supramolecular self-assembling behaviour [9–13]. 1,4-Dithiafulvene (DTF), which is the half structure of TTF, is also a good  $\pi$ -electron donor as a result of its gaining of aromaticity upon one-electron oxidation (see Figure 2.1). Synthetically, DTF-substituted arenes can undergo a facile coupling reaction under oxidative conditions to form  $\pi$ -extended TTF derivatives as depicted in Figure 2.1, namely tetrathiafulvalene vinylogues (TTFVs) [14–21]. Over the past few years, such reactivity has enabled the preparation of a variety of intriguing molecular devices, including chemosensors [22–25], molecular switches [25–32], and supramolecular hosts [23].

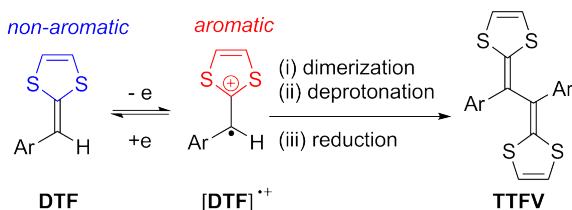


Figure 2.1: General redox reactivity of a DTF-substituted arene.

Most recently, the application of DTF as a redox-active substituent to modulate the electronic and photonic properties of  $\pi$ -conjugated oligomers has been increasingly pursued. In 2009, Roncali and co-workers reported the study of a series of bis(DTF)-functionalized arenes (benzene, pyrrole, thiophene, *etc.*) as the active building components for organic field effect transistors (OFETs) [33]. In 2012, Yang and co-workers prepared a group of DTF-functionalized phenylene/thienylene oligomers and applied them as highly efficient organic sensitizers for dye-sensitized solar cells [34]. In 2014, Guo and co-workers discovered that a bis(DTF)-endcapped phenylene thienylene oligomer can form *J*-aggregates in the solid state and hence give rise to aggregation-induced enhanced emission (AIEE) [35]. Most recently, functionalization of DTF groups on the  $\pi$ -frameworks of oligo(phenylene ethynylene)s was found to result in significantly increased molecular conductance by Nielsen and co-workers [36,37]. Mulla

and Zhao recently synthesized a group of bis(DTF)-endcapped phenylene ethynylene and phenylene vinylene oligomers and characterized their supramolecular interactions with fullerenes and single-walled carbon nanotubes (SWNTs) [38].

Despite the active exploration of DTF-functionalized  $\pi$ -oligomer systems in the recent literature, there are still some fundamentally important questions that await to be answered; for instance, in a dumbbell-like DTF- $\pi$ -DTF system, (i) what are the redox activity and reactivity of the two DTF groups in the solution phase and solid state? (ii) How would the DTF groups affect the electron delocalisation of the  $\pi$ -oligomer in their neutral and oxidized states? (iii) To what extent will the redox processes taking place on the DTF groups change the solid-state aggregation properties? Understanding these issues will be of great benefit and guidance to further development of DTF-functionalized molecular materials, while comprehensive experimental characterization in combination with high-level computational studies are deemed as an effective problem-solving approach.

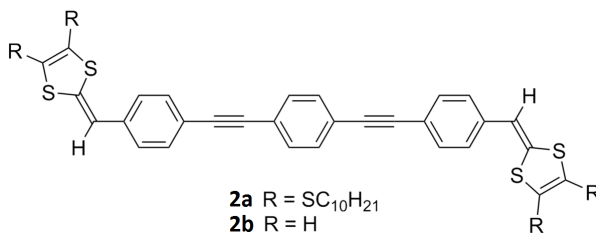


Figure 2.2: Structures of bis(DTF)-endcapped oligo(phenylene ethynylene)s **2**.

In this work, linear-shaped bis(DTF)-endcapped phenylacetylene oligomers **2** (Figure 2.2) were chosen as model compounds for a joint experimental and theoretical investigation on the DTF- $\pi$ -DTF systems. The synthesis of **2a** has been established previously [38]. Structurally, it contains two electron-donating DTF endgroups that are in direct  $\pi$ -conjugation with a central trimeric phenylene ethynylene unit. Modulation of the  $\pi$ -electron delocalization characteristics of the oligo(phenylene ethynylene) unit by the DTF endgroups can thus be envisioned. In the previous studies carried

out by the Zhao group, the electronic and redox properties of **2a** in solution phase were generally characterized by UV-Vis absorption and cyclic voltammetric analyses in solution [38], Herein the characterization of oligomer **2a** in both solution and solid phases was undertaken using electrochemical, UV-Vis absorption, and Raman spectroscopic analyses. It is worth mentioning that Raman spectroscopy has been proven to be a very powerful tool for elucidating the properties of  $\pi$ -conjugated oligomers in their neutral and various oxidized states [39–42]. To better interpret the experimental data, density functional theory (DFT) calculations were conducted on a model compound, bis(DTF)-oligomer **2b**, which has an identical DTF– $\pi$ –DTF framework to that of **2a**, but without the  $\text{SC}_{10}\text{H}_{21}$  side groups attached to the DTF moieties to save computational costs. The following sections describe the experimental and theoretical data determined for the bis(DTF)-oligo(phenylene ethynylene) system **2a–b**. On the basis of these data, relevant structure-property relationships can be established.

## 2.2 Experimental Section

### 2.2.1 Computational Methods

DFT calculations were carried out with the Gaussian 09 software package [43], using Becke’s three-parameter exchange functional combined with the LYP correlation functional (B3LYP) [44]. Optimization of molecular geometry was conducted at the B3LYP/6-31++G(d,p) level of theory, with frequency calculations performed afterwards to analyse the vibrational modes and to determine whether the optimized structures are true minima. Excitation energies and excited-state properties were calculated based on the time-dependent density functional theory (TD-DFT) [45] using the B3LYP functional and 6-31++G(d,p) basis set, with only singlet to singlet transitions considered. Simulated UV-Vis absorption and Raman spectra were generated

by the GaussView 5 software package [46]. The polarizable continuum model (PCM) was adopted to include the effect of chloroform solvent [47].

### 2.2.2 Experimental Characterization

Oligomer **2a** was synthesized according to the reported procedures [38]. UV-Vis absorption spectra of **2a** were recorded in solution or solid thin films on a Cary 6000i UV-Vis-NIR spectrophotometer. Cyclic voltammetric (CV) analysis was performed on a BASi Epsilon electrochemical analyser using a standard three-electrode setup (glass carbon as the working electrode, Ag/AgCl as the reference electrode, and Pt wire as the counter electrode). Morphological study of the thin film surface was done by using an MFP-3D (Asylum Research) atomic force microscope (AFM), with a silicon tip (NSC35/AIBS, MikroMasch) operating in the tapping mode (scan rate 1 Hz). Surface roughness was calculated using the method implemented in the Asylum Research software. Raman spectroscopic measurements of the thin film of **2a** were conducted on a Renishaw inVia instrument excited at 830 nm.

Thin films of **2a** were prepared by drop-casting or spin-coating a solution of **2a** in toluene on the surfaces of mica, glass, or highly ordered pyrolytic graphite (HOPG) using a Laurell WS-650-23 spin-coater (800 rpm for 1 min followed by 1000 rpm for another 1 min). Chemical oxidation of the thin film of **2a** was conducted by placing the sample in a covered glass vessel containing iodine as oxidant. In this way, the sample was exposed to iodine vapour for different time intervals and then taken out for the spectroscopic and microscopic analyses.

## 2.3 Results and Discussion

### 2.3.1 Structural and Electronic Properties in the Neutral and Oxidized States

The optimized geometry of model compound **2b** in the neutral state is shown in Figure 2.3. The entire molecular  $\pi$ -framework exhibits complete planarity, with the two dithiole rings taking a *trans* orientation with respect to the central oligomer unit. Such a molecular shape is in line with the demands for maximal  $\pi$ -conjugation and minimal molecular dipole moment.

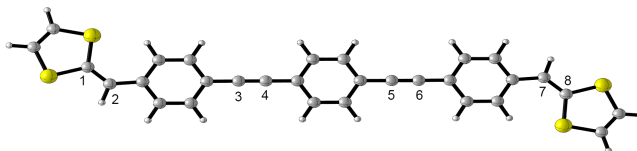


Figure 2.3: Optimized geometry of **2b** at the B3LYP/6-31++G(d,p) level and adopted labeling scheme in this study.

The optimized geometries of **2b** in the radical cation and dication states were also calculated. With these structures, the degrees of  $\pi$ -electron delocalisation for **2b** in different oxidation states were assessed by examining the bond length changes, particularly those of C=C (1–2 and 7–8) and C $\equiv$ C (3–4 and 5–6) bonds in the central  $\pi$ -framework, as it has been established that the bond length alternation (BLA) is correlated with the electronic characteristics of  $\pi$ -conjugated systems [48–50]. Figure 2.4A depicts the comparison of averaged C=C and C $\equiv$ C bond lengths in the neutral, radical cation, and dication forms respectively. For the dication state, two forms of spin multiplicity, singlet and triplet, were calculated and examined. As shown in Figure 2.4A, both the averaged C=C and C $\equiv$ C bonds are considerably more elongated in the state of radical cation than in dication, indicating that the radical cation state achieves the highest degree of  $\pi$ -electron delocalisation.

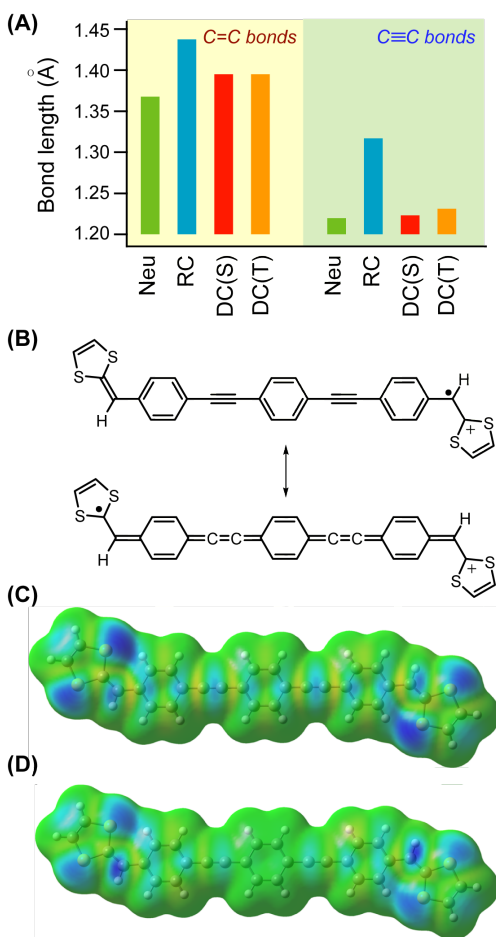


Figure 2.4: (A) Comparison of averaged C=C and C≡C bond lengths of compound **2b** in neutral (Neu), radical cation (RC), singlet dication (DC(S)), and triplet dication (DC(T)) states. (B) A resonance scheme for the radical cation of **2b**. (C) Calculated spin density map for the radical cation of **2b**. (D) Calculated spin density map for the triplet dication of **2b**. The high and low unpaired electron density areas are highlighted by blue and green colours respectively.

The high degree of delocalisation in the radical cation state can be qualitatively interpreted by the classical resonance model shown in Figure 2.4B, in which the vinyl radical is predicted to delocalise through the oligo(phenylene ethynylene)  $\pi$ -bridge to the dithiole moiety at the other end of the molecule. From the resonance scheme one can also identify a synergistic stabilizing effect (known as the captodative effect) on the radical imposed by the electron donating dithiole and electron-withdrawing dithiolium units. The highly delocalised nature of the radical cation of **2b** can also be seen from the results of spin density analysis. In Figure 2.4C, the regions of high unpaired electron density are found to populate along the entire molecular  $\pi$ -framework, with particularly high concentration at the terminal dithiole rings.

In the state of dication, both the singlet and triplet forms show similar C=C bond lengths, whereas the triplet appears to have a slightly longer C $\equiv$ C bond than the singlet. The computational results thus suggest that the singlet and triplet dications possess similar degrees of  $\pi$ -delocalisation, although the triplet dication is calculated to be 16.73 kJ/mol more stable than the singlet in the gas phase. The spin density properties of the triplet dication of **2b**, which is in essence a biradical dication, were also calculated as depicted in Figure 2.4D. In this map, the highest unpaired electron densities are clearly seen to be located around the vinyl carbons, which is different than the case of radical cation (Figure 2.4C) where the radical character is more dispersed along the molecular  $\pi$ -framework.

### 2.3.2 Frontier Molecular Orbitals and Redox Properties in Solution Phase

The frontier molecular orbitals and orbital energies of **2b** are shown in Figure 2.5. The HOMO is found to be evenly distributed along the entire  $\pi$ -framework, encompassing the central oligo(phenylene ethynylene) bridge and the two DTF endgroups. The

LUMO is mainly on the central oligomer bridge, while the DTF groups contribute less significantly. For the HOMO-1 and LUMO+1, the orbital coefficients on central benzene become quite insignificant. More significant contributions actually come from the outside benzene rings and DTF groups in these two orbitals.

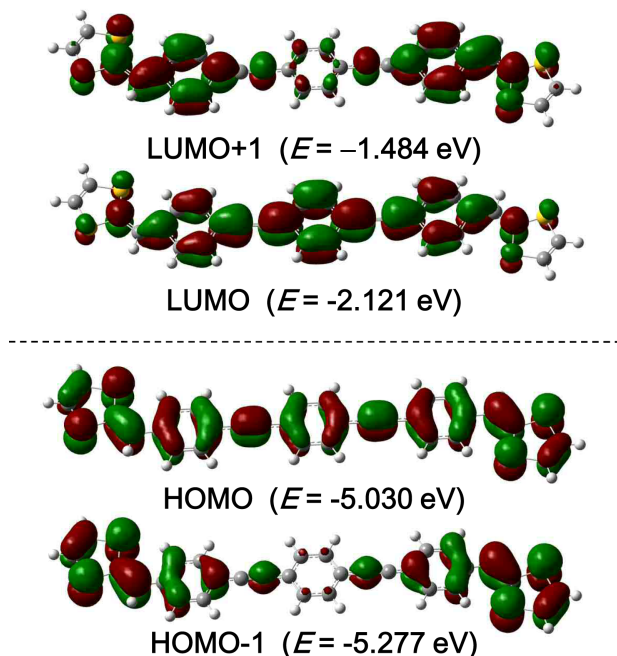


Figure 2.5: Contour maps of frontier MOs for compound **2b** (isovalue = 0.02 a.u.) and their eigenvalues calculated at the B3LYP/6-31++G(d,p) level.

The oxidation processes of compound **2b** leading to the formation of radical cation and dication species were simulated by DFT calculations in both the gas and solution phases ( $\text{CH}_2\text{Cl}_2$  as solvent). The detailed thermodynamic data involved in each step of single-electron transfer are provided in the square scheme shown in Figure 2.6. It is particular notable that the  $\Delta G^\circ$  values for the formation of singlet dication and triplet dication appear to be very different in the gas phase. However, in the solution phase the values become identical, as a result of the different solvation energies for singlet and triplet dications. The potentials ( $E^\circ$ ) for the stepwise oxidation were calculated using the equation,  $\Delta G^\circ = nFE^\circ$ , where  $n$  is the number of electrons and  $F$  is the



dimerization of the DTF units [14–21]. Similarly, two oxidation peaks are seen in the DPV plot of **2a** at +0.74 V and +0.99 V. Compared with the computational results, the experimental data shows a good agreement with the second oxidation potential ( $E_{\text{ox}}^2$ ), while for the first oxidation potential ( $E_{\text{ox}}^1$ ) the calculated value appears to be lower than the experimental result by *ca.* 0.3–0.4 V. The discrepancy may arise from overestimated  $\pi$ -delocalisation degree for the radical cation of **2b** in solution phase, since only the planar conformation was considered in the computational work.

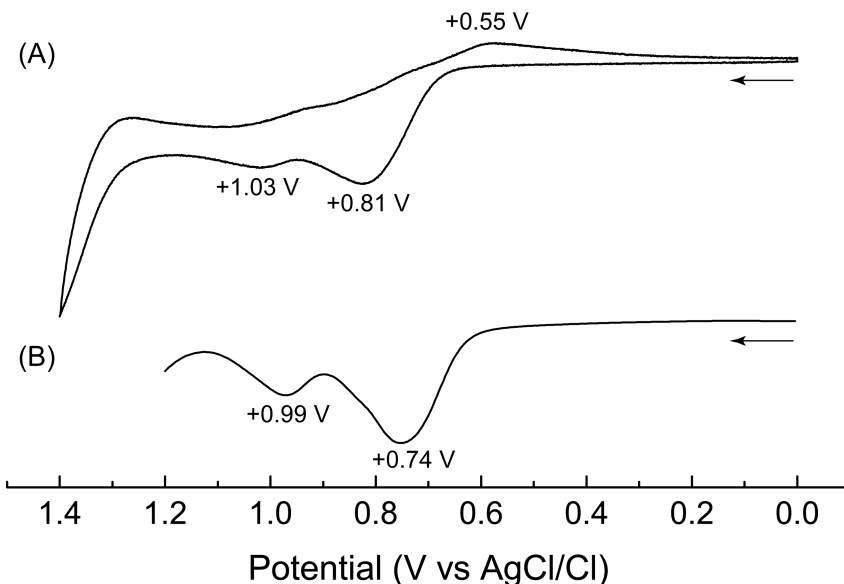


Figure 2.7: (A) CV and (B) DPV profiles of **2a** ( $1.33 \times 10^{-3}$  M) measured in  $\text{CH}_2\text{Cl}_2$  at room temperature with  $\text{Bu}_4\text{NBF}_4$  (0.1 M) as the supporting electrolyte, glassy carbon as the working electrode, Pt wire as the counter electrode, Ag/AgCl as the reference electrode. CV conditions: scan rate =  $50 \text{ mV s}^{-1}$ . DPV conditions: scan rate =  $20 \text{ mV s}^{-1}$ , pulse width = 20 mV, pulse period = 200 ms, pulse amplitude = 50 mV, and step = 4 mV.

To further understand the electron-density contribution by different  $\pi$ -units in the bis(DTF)-functionalized oligo(phenylene ethynylene)s, natural population analysis (NPA) as proposed by Weinhold and co-workers [52] was performed on compound **2b**. Figure 2.8 shows the NPA charge distribution between the DTF endgroup and the central oligomer unit in the neutral, radical cation, and dication states. In the

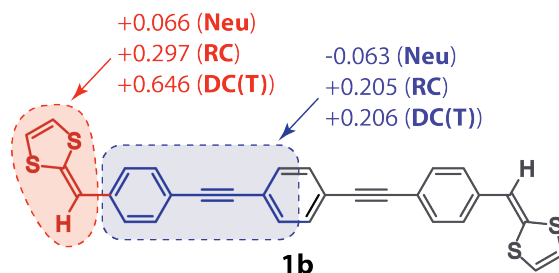


Figure 2.8: NPA charge distribution for compound **2b** in the neutral (Neu), radical cation (RC), and triplet dication (DC(T)) states. The values indicated are accumulated NPA charges for the atoms in each shaded area.

neutral state, each of the DTF groups carries a slight positive charge of +0.066, while the oligomer unit possesses a negative charge of  $-0.126$ . The result points to a charge-transfer scenario from electron-donating DTF groups to the oligo(phenylene ethynylene) unit. Upon oxidation to the radical cation, the DTF groups and oligomer unit all gain significantly increased charge. Quantitatively, the NPA result shows that, in the first step of single electron oxidation, 46% of electron density is extracted from the two DTF groups and 54% taken from the central oligomer unit. This scenario is in line with the highly delocalised nature of radical cation revealed by previous bond length and spin-density analyses. For the second step of oxidation (*i.e.*, from radical cation to dication), the central oligomer unit shows a very tiny increase of +0.002 in charge, while the accumulated charge of the two DTF groups are further increased by +0.698, implying that electron density is predominantly extracted from the DTF groups during the second oxidation.

### 2.3.3 Electrochromic Properties in Solution and in the Solid State

The electronic absorption properties of compound **2a** were investigated in solution phase as well as the solid state by UV-Vis absorption spectroscopy. Figure 2.9A shows

the absorption spectrum of **2a** determined in CH<sub>2</sub>Cl<sub>2</sub>, in which two  $\pi \rightarrow \pi^*$  transition bands are clearly seen at 412 nm and 322 nm. The experimental data of **2a** appear to be consistent with the TD-DFT calculations that **2b** gives two absorption bands at 471 nm and 352 nm as shown in Figure 2.9D. The peak at 471 nm is mainly attributed to the HOMO $\rightarrow$ LUMO transition, while the peak at 352 nm is mainly due to the HOMO-1 $\rightarrow$ LUMO+1 transition. From Figure 2.5, it can be seen that the HOMO and LUMO of **2b** have similar symmetry and spatial distribution, and so do the HOMO-1 and LUMO+1 orbitals. The HOMO $\rightarrow$ LUMO+1 and HOMO-1 $\rightarrow$ LUMO transitions, on the other hand, are forbidden as a result of their mismatching spatial distribution.

The solid-state UV-Vis spectrum of **2a** was measured from a thin film cast on a quartz slide (Fig 2.9B). Unlike the spectrum obtained in solution, the solid-state spectrum shows only one absorption peak at 424 nm, matching the HOMO $\rightarrow$ LUMO transition, whereas the other transition band at 352 nm is barely distinguishable. The thin film was then placed in an iodine chamber to be oxidized by iodine vapour at room temperature for 30 min. According to the electrochemical data, oxidation of compound **2a** leads to sequential formation of radical cation and dication species. The UV-Vis spectrum of oxidized **2a** in solid thin film (Figure 2.9C) shows a wide absorption profile extending to 800 nm, indicating the formation of cationic species after iodine oxidation. Unfortunately, the UV-Vis spectrum of oxidized **2a** appears to be broad and featureless. As a result, it cannot be used to make good match with any of the TD-DFT calculated spectra for oxidized **2a** (Figure 2.9D-F) to convincingly elucidate the nature of the oxidized species. Nevertheless, this dilemma has been solved by Raman spectroscopic analysis (*vide infra*).

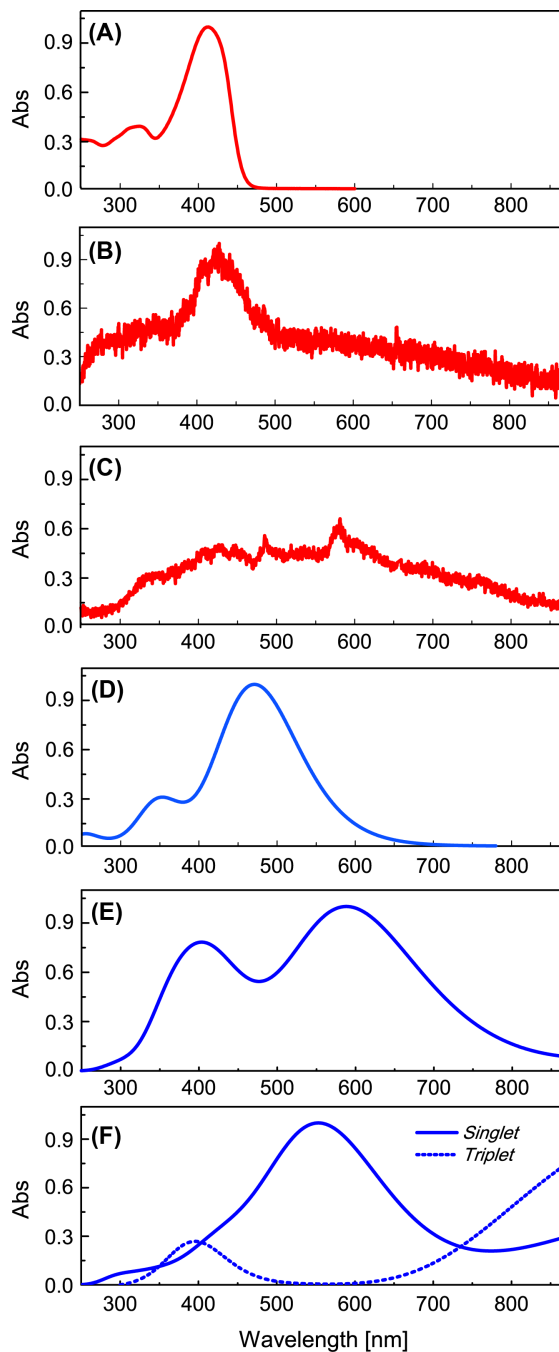


Figure 2.9: (A) Normalized UV-Vis absorption spectrum of **2a** measured in  $\text{CH}_2\text{Cl}_2$  at room temperature. (B) UV-Vis absorption spectrum of the thin film of **2a** cast on a quartz slide. (C) UV-Vis absorption spectrum of the thin film of **2a** measured after exposure to iodine vapour for 30 min. (D) Calculated UV-Vis absorption spectrum (normalized) of **2b**. (E) Calculated UV-Vis absorption spectrum (normalized) of the radical cation of **2b**. (F) Calculated UV-Vis absorption spectra (normalized) of the dications of **2b** in the singlet and triplet states.

### 2.3.4 Raman Analysis

The thin film of **2a** was exposed to iodine vapour in a glass chamber to induce chemical oxidation in the solid state. This process was monitored by Raman spectroscopy, and the spectra obtained at various time periods of oxidation are shown in Figure 2.10.

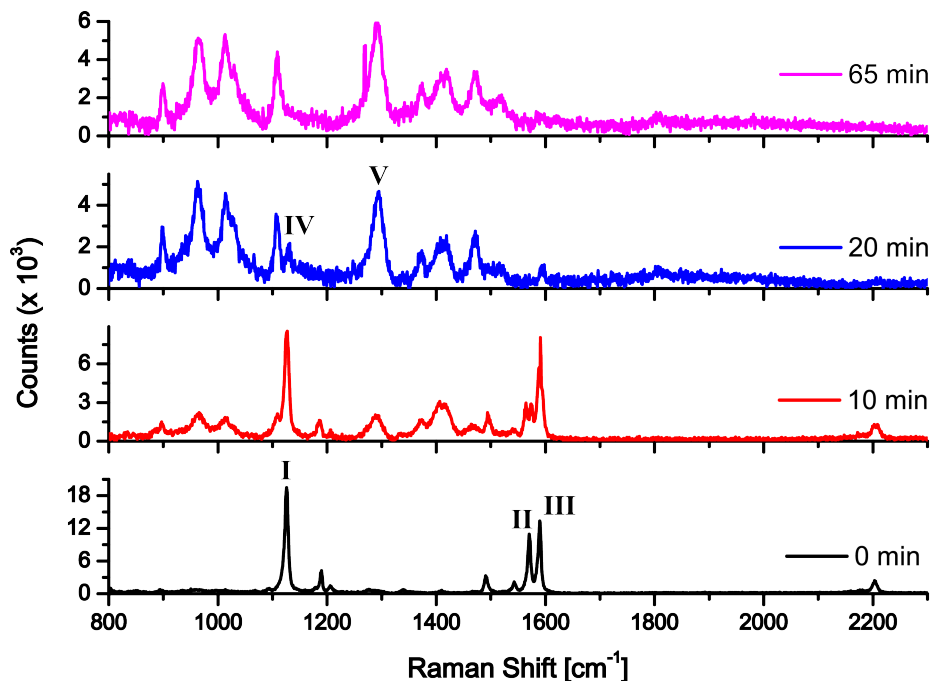


Figure 2.10: Raman spectroscopic analysis monitoring the thin film of **2a** upon exposure to iodine vapour at various time periods. The baselines of the spectra were corrected using the *Fityk* software (free version 0.9.8) [53].

To better understand the origins of the Raman bands experimentally observed, the Raman spectra of model compound **2b** in the neutral and oxidized states were theoretically predicted based on DTF calculations. The calculated Raman spectra are shown in Figure 2.11, and detailed spectral assignments and descriptions of Raman-active vibrational eigenvectors can be found in the Appendix A.

Comparatively, the spectral patterns of the neutral thin film of **2a** agree those calculated for model compound **2b** very well in the range of *ca.* 1000 to 1700  $\text{cm}^{-1}$ , a region mainly due to the stretching of C=C bonds and bending of C-H bonds. Ex-

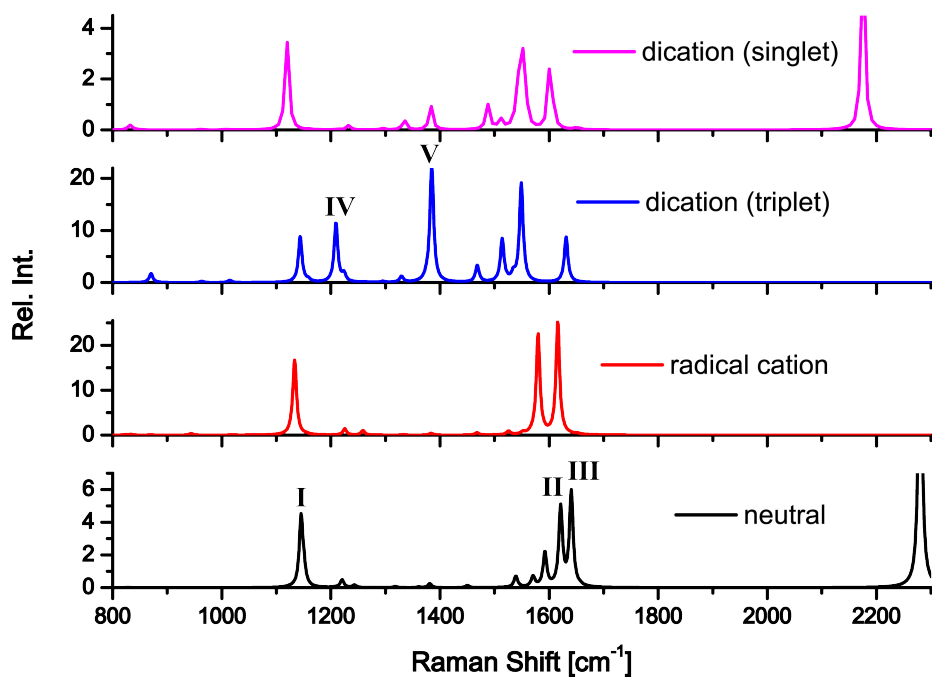


Figure 2.11: Raman spectra of compound **2b** in different oxidation states calculated at the B3LYP/6-31++G(d,p) level of theory.

perimentally, the Raman spectrum of the neutral **2a** gives two significant vibrational bands at  $1571\text{ cm}^{-1}$  and  $1590\text{ cm}^{-1}$ , which reasonably match the DFT calculated C=C stretching (mode III at  $1621\text{ cm}^{-1}$ ) and a combination of C=C stretching and C–H rocking (mode II at  $1640\text{ cm}^{-1}$ ) modes. The detailed descriptions of the vibrational eigenvectors are provided in Figure 2.12. Besides, a strong Raman band at  $1126\text{ cm}^{-1}$  can be clearly seen, the origin of which is ascribed to the C–H rocking theoretically calculated at  $1145\text{ cm}^{-1}$  (mode I). For the stretching of C≡C bonds, however, the experimentally observed band at  $2206\text{ cm}^{-1}$  exhibits a much weaker relative intensity than that in the DFT predicted spectrum. The discrepancy between the experimental and theoretical data may arise from a solid-state packing effect.

After exposing the solid film of **2a** to iodine vapour for 10 min, more vibrational bands emerge in the Raman spectrum in the range from *ca.*  $900$  to  $1600\text{ cm}^{-1}$ . The

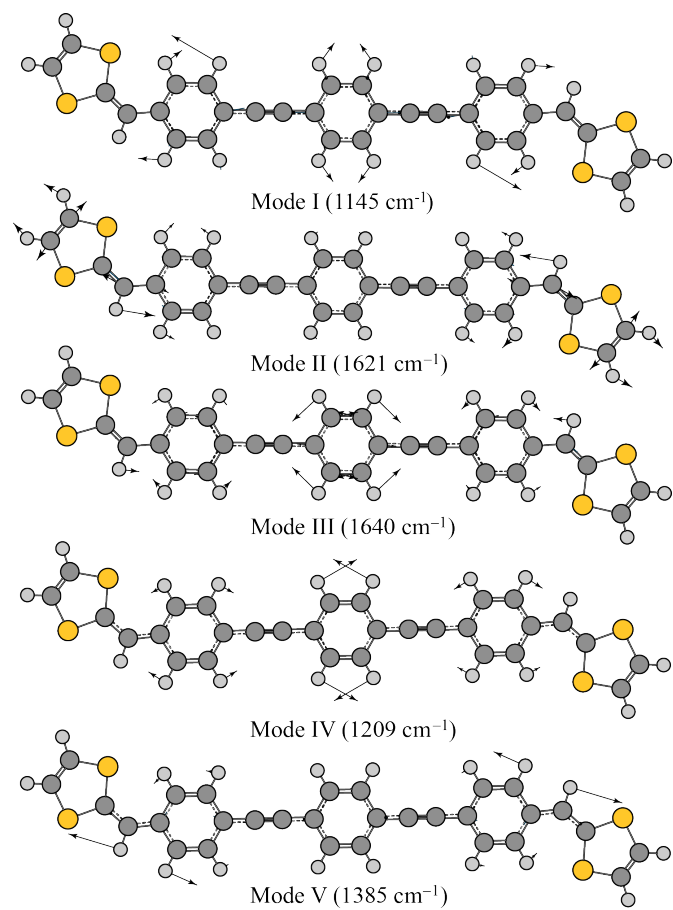


Figure 2.12: Selected Raman-active vibrational eigenvectors for compound **2b** at different oxidation states calculated at the B3LYP/6-31++G(d,p) level.

resulting spectral patterns match reasonably well with the calculated Raman spectrum simulating a mixture of neutral, radical cation and triplet dication in a 10:1:1 ratio (see Figure 2.10). In particular, good agreements can be found for the vibrational bands due to the C=C stretching, C–H scissoring, and C–H rocking modes as highlighted in Figure 2.13. As the oxidation proceeded further with increased exposure time to iodine vapour, the C≡C and C=C stretching and C–H rocking (modes II and III) bands disappeared in the Raman spectra (see Figure 2.10). The resulting spectra show a very significant band at 1291 cm<sup>-1</sup> along with several other relatively weak bands in the region of 1200 to 1600 cm<sup>-1</sup>. The patterns of highly oxidized thin film of **2a** resemble those of triplet dication of **2b**, suggesting the dominant species after exhaustive oxidation in the solid state is triplet dication.

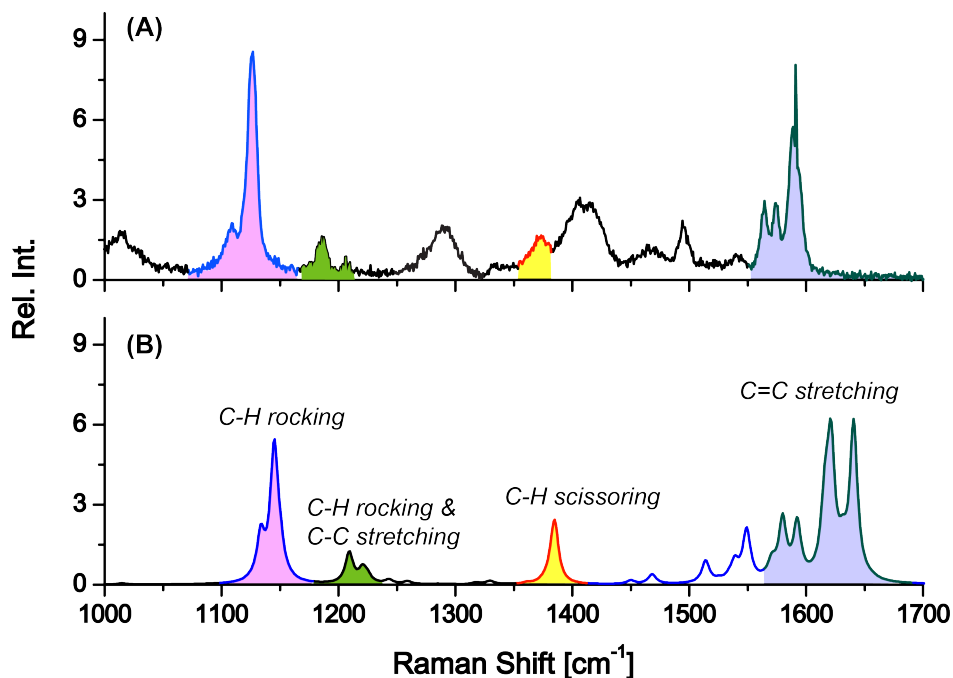


Figure 2.13: Comparison of (A) the Raman spectrum for the thin film of **2a** upon exposure to iodine vapour for 10 min and (B) the simulated Raman spectrum for a mixture of **2b** in neutral, radical cation, and triplet dication states at a 10:1:1 molar ratio.

The joint experimental and theoretical Raman study has allowed an in-depth un-

derstanding of the chemical oxidation reactions of bis(DTF)-encapped oligo(phenylene ethynylene)s in the solid state. Consistent with the solution phase redox behaviour as revealed by the electrochemical characterizations, the solid film of **2a** is believed to undergo stepwise single-electron transfers, forming radical cation and dication sequentially. The dication is in the triplet state as evidenced by Raman analysis. In the meantime, DFT calculations in the gas phase corroborate that the triplet dication is more stable than the singlet dication by 16.73 kJ/mol. The solid film of **2a** after exposure to iodine vapour for about 1 hour was then placed under air to allow the iodine adsorbed in the solid film to be dissipated slowly by vapourisation. After two weeks, the thin film was re-examined by Raman spectroscopy, and the resulting Raman spectrum was found to be similar to the spectrum of the initial neutral thin film. This observation suggests that the DTF oxidative coupling reaction (as shown in Figure 2.1), unlike in solution phase, occurs at a rather slow rate in the solid state.

### 2.3.5 Surface Self-assembling Properties

The morphologies of the thin films of **2b** cast on solid substrates were analyzed by atomic force microscopic (AFM) measurements. In the AFM experiments, two substrates were used, freshly cleaved mica and highly ordered pyrolytic graphite (HOPG), in order to assess the effects of substrate on the microscopic aggregation behaviour. Figure 2.14A shows the AFM image for the thin film of **2b** on a mica surface. The aggregates of **2b** on mica exhibit a certain degree of directional ordering, giving oblong shaped micro-domains with an average length on the micron scale. On the surface of HOPG, similar aggregation features can be seen (Fig. 2.14C), however, the dimensions of the oblong microstructures appear to be much smaller. It is known that the surface of mica contains polar and negatively charge functional groups, while the surface of HOPG is made of hydrophobic polycyclic aromatic hydrocarbons. The AFM

results hence suggest that the nature of the substrate surface can significantly affect the dimension of DTF-oligomer aggregates, but does not cause too much change in shape.

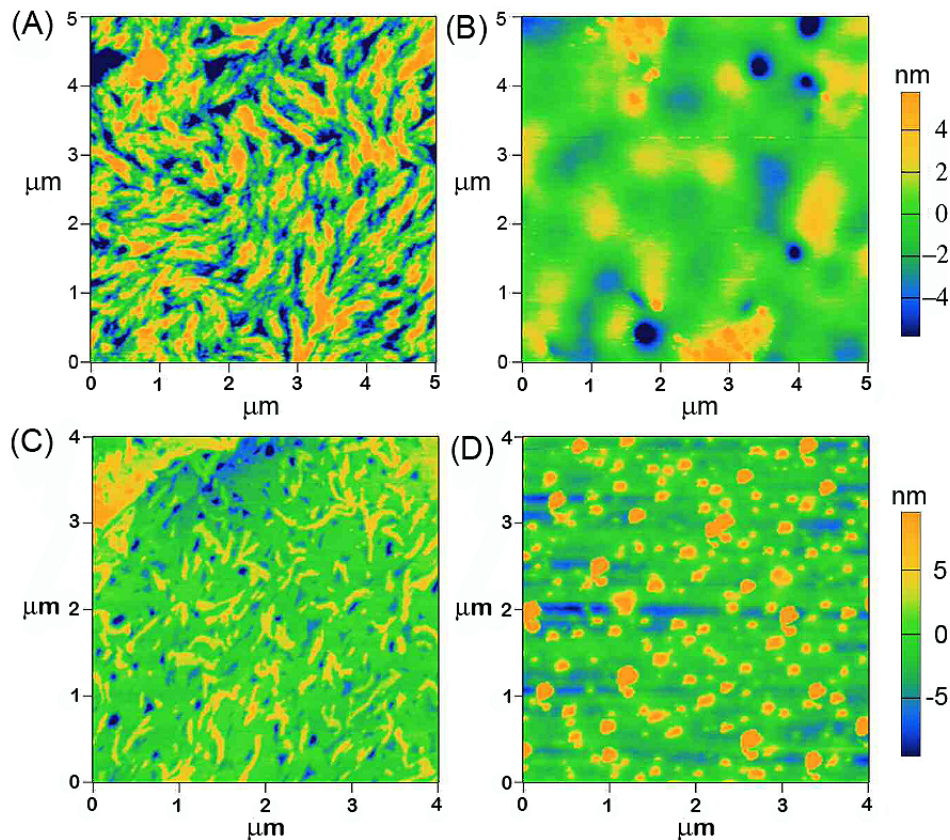


Figure 2.14: AFM images of compound **2b** (A) on freshly cleaved mica surface, (B) on mica after oxidation with iodine for 30 min, (C) on freshly cleaved HOPG, and (D) on HOPG after oxidation with iodine for 30 min.

After oxidation with iodine vapour for *ca.* 30 min, the surface morphologies for the thin films of **2b** show dramatic changes (see Figure 2.14B and D). On mica, the closely packed oblong assemblies completely disappear, while some kind of flake-like nanoassemblies can be observed in certain areas. The dimensions of these “flakes” are on the scale of a few hundreds of nanometers. On HOPG, relatively uniform droplet-like micro-domains were seen on the surface after oxidation (Figure 2.14D). The dimensions of these “droplets” range from tens to hundreds of nanometers. Ob-

viously, the thin film of **2a** on HOPG gains better ordering and uniformity after oxidation. The improved inter-facial organization can be ascribed to the hydrophobic interactions between the HOPG surface and the dication of **2a**.

The aforementioned spectroscopic studies suggest that **2a** does not undergo significant polymerization in the solid state after oxidation. Hence, it is reasonable to assume that the reconstruction of the surface morphologies is mainly driven by the ionic interactions between the dications of **2b** in the solid aggregates. Repulsive forces are likely to play a major role, causing drastic changes in the sizes and shapes of aggregates at the microscopic level. Furthermore, what turns out to be interesting is that ordered nanoparticles were only formed on the surface HOPG, suggesting that the substrate effect indeed plays a key role here. Detailed mechanisms for the surface self-assembling processes require further investigation under more systematically controlled experimental conditions are to be disclosed. Overall, the current AFM study confirms that the thin film morphology of **2b** shows redox-regulated responsiveness, and such behaviour may be utilized to exert bottom-up controls over the microscopic organisation of DTF-functionalised  $\pi$ -oligomers in the solid state.

## 2.4 Conclusions

This work has examined the properties of bis(DTF)-endcapped oligo(phenylene ethynylene)s **2** by a joint experimental and theoretical study. The two DTF groups undergo sequential single electron transfers upon oxidation leading to the formation of radical cation and dication species in both solution phase and the solid state. The redox properties characterized by solution-phase electrochemical analysis are consistent with the ionization energies elicited from DFT calculations. Of the oxidized species, the radical cation form has a higher degree of  $\pi$ -electron delocalisation than the dication form.

For the dication, the triplet state is energetically more stable than the singlet state according to DFT calculations, and this has been corroborated by Raman analysis.

In the solution phase, oxidative polymerisation of **2a** was observed to take place upon electrochemical oxidation in our previous study [38]. In this work, however, the electrochemical reactivity of **2a** was found to be insignificant in the solid state. Finally, the microscopic morphological properties for the thin film of **2a** have been observed to show responsiveness to different redox states. The nature of substrate also appears to be a significant factor influencing the sizes and shapes of nano-assemblies on surface. Currently, DTF-functionalized  $\pi$ -oligomers have begun to attract growing interest in molecular electronic and optoelectronic applications. Our studies hence contribute useful knowledge to the development of redox-active functional  $\pi$ -conjugated oligomers and polymers.

## Bibliography

- [1] G Inzelt. *Conducting polymers: a new era in electrochemistry*. Springer, Berlin, 2008.
- [2] Toshikazu Hirao. *Redox systems under nano-space control*. Springer, Berlin, 2006.
- [3] Jean Roncali. Conjugated poly (thiophenes): synthesis, functionalization, and applications. *Chem. Rev.*, 92:711–738, 1992.
- [4] Jean Roncali. Synthetic principles for bandgap control in linear  $\pi$ -conjugated systems. *Chem. Rev.*, 97:173–206, 1997.
- [5] Toshikazu Hirao. Conjugated systems composed of transition metals and redox-active  $\pi$ -conjugated ligands. *Coord. Chem. Rev.*, 226:81–91, 2002.

- [6] Bradley J Holliday and Timothy M Swager. Conducting metallopolymers: the roles of molecular architecture and redox matching. *Chem. Commun.*, pages 23–36, 2005.
- [7] Hamad Khalid, Haojie Yu, Li Wang, Wael A Amer, Muhammad Akram, Nasir M Abbasi, Muhammad Saleem, et al. Synthesis of ferrocene-based polythiophenes and their applications. *Polym. Chem.*, 5:6879–6892, 2014.
- [8] Raquel Gracia and David Mecerreyes. Polymers with redox properties: materials for batteries, biosensors and more. *Polym. Chem.*, 4:2206–2214, 2013.
- [9] Nazario Martín. Tetrathiafulvalene: the advent of organic metals. *Chem. Commun.*, 49:7025–7027, 2013.
- [10] José L Segura and Nazario Martín. New concepts in tetrathiafulvalene chemistry. *Angew. Chem. Int. Ed.*, 40:1372–1409, 2001.
- [11] Mogens Brøndsted Nielsen, Christian Lomholt, and Jan Becher. Tetrathiafulvalenes as building blocks in supramolecular chemistry II. *Chem. Soc. Rev.*, 29:153–164, 2000.
- [12] Martin R Bryce. Current trends in tetrathiafulvalene chemistry: towards increased dimensionality. *J. Mater. Chem.*, 5:1481–1496, 1995.
- [13] David Canevet, Marc Salle, Guanxin Zhang, Deqing Zhang, and Daoben Zhu. Tetrathiafulvalene (TTF) derivatives: key building-blocks for switchable processes. *Chem. Commun.*, pages 2245–2269, 2009.
- [14] Yuming Zhao, Guang Chen, Karimulla Mulla, Ilias Mahmud, Shuai Liang, Praateek Dongare, David W. Thompson, Louise N. Dawe, and Stephen Bouzan.

- Tetrathiafulvalene vinylogues as versatile building blocks for new organic materials. *Pure Appl. Chem.*, 84:1005–1025, 2012.
- [15] Michael Bendikov, Fred Wudl, and Dmitrii F Perepichka. Tetrathiafulvalenes, oligoacenes, and their buckminsterfullerene derivatives: The brick and mortar of organic electronics. *Chem. Rev.*, 104:4891–4946, 2004.
- [16] Jean Roncali. Linearly extended  $\pi$ -donors: when tetrathiafulvalene meets conjugated oligomers and polymers. *J. Mater. Chem.*, 7:2307–2321, 1997.
- [17] Adrian J Moore and Martin R Bryce. New vinylogous tetrathiafulvalene (TTF)  $\pi$ -electron donors. *Tetrahedron Lett.*, 33(10):1373–1376, 1992.
- [18] Lianhe Yu and Daoben Zhu. New vinylogous tetrathiafulvalene  $\pi$ -electron donors with lower oxidation potentials. *Chem. Commun.*, pages 787–788, 1997.
- [19] Hiroshi Kato and Tomoshige Kobayashi. Nonplanar tetrathiafulvalene vinylogues. *Adv. Mater.*, 5:750–751, 1993.
- [20] Michel Guerro and Dominique Lorcy. A simple route to novel functionalized tetrathiafulvalene vinylogues. *Tetrahedron Lett.*, 46:5499–5502, 2005.
- [21] Philippe Hapiot, Dominique Lorcy, André Tallec, Roger Carlier, and Albert Robert. Mechanism of dimerization of 1, 4-dithiafulvenes into TTF vinylogues. *J. Phys. Chem.*, 100:14823–14827, 1996.
- [22] Karimulla Mulla and Yuming Zhao. TTFV molecular tweezers with phenylboronic acid and phenylboronate endgroups: modular synthesis and electrochemical responses to saccharides and fluoride ion. *Tetrahedron Lett.*, 55:382–386, 2014.

- [23] Karimulla Mulla, Haseena Shaik, David W Thompson, and Yuming Zhao. TTFV-based molecular tweezers and macrocycles as receptors for fullerenes. *Org. Lett.*, 15:4532–4535, 2013.
- [24] Karimulla Mulla, Prateek Dongare, David W Thompson, and Yuming Zhao. Click synthesized dianthryl–TTFV: an efficient fluorescent turn-on probe for transition metal ions. *Org. Biomol. Chem.*, 10(13):2542–2544, 2012.
- [25] Julien Massue, Nathalie Bellec, Michel Guerro, Jean-François Bergamini, Philippe Hapiot, and Dominique Lorcy. Crown ether vinylogous tetrathiafulvalene receptors: Complexation interference on the molecular movements triggered by electron transfer. *J. Org. Chem.*, 72:4655–4662, 2007.
- [26] Dominique Lorcy, Michel Guerro, Jean-François Bergamini, and Philippe Hapiot. Vinylogous tetrathiafulvalene based podands: complexation interferences on the molecular movements triggered by electron transfer. *J. Phys. Chem. B*, 117:5188–5194, 2013.
- [27] Elodie Gontier, Nathalie Bellec, Pierre Brignou, Arnaud Gohier, Michel Guerro, Thierry Roisnel, and Dominique Lorcy. Pyridyldithiafulvenes as precursors of coordination-driven self-assembled redox active macrocycle. *Org. Lett.*, 12:2386–2389, 2010.
- [28] Michel Guerro, Roger Carlier, Kamal Boubekour, Dominique Lorcy, and Philippe Hapiot. Cyclic vinylogous TTF: a potential molecular clip triggered by electron transfer. *J. Am. Chem. Soc.*, 125:3159–3167, 2003.
- [29] Guang Chen, Stephen Bouzan, and Yuming Zhao. Synthesis and properties of TTFV-hinged molecular tweezers. *Tetrahedron Lett.*, 51:6552–6556, 2010.

- [30] Guang Chen, Ilias Mahmud, Louise N Dawe, and Yuming Zhao. Acetylenic phenyldithiafulvene: a versatile synthon for TTFV-based macromolecules. *Org. Lett.*, 12:704–707, 2010.
- [31] Guang Chen, Ilias Mahmud, Louise N Dawe, Lee M Daniels, and Yuming Zhao. Synthesis and properties of conjugated oligoynes-centered  $\pi$ -extended tetrathiafulvalene analogues and related macromolecular systems. *J. Org. Chem.*, 76:2701–2715, 2011.
- [32] Guang Chen and Yuming Zhao. Redox-regulated rotary motion of a bis (9-triptycyl)-TTFV system. *Org. Lett.*, 16:668–671, 2014.
- [33] Olivier Alévêque, Pierre Frère, Philippe Leriche, Tony Breton, Antonio Cravino, and Jean Roncali. Effects of aromatic spacers on the properties of organic field effect transistors based on  $\pi$ -extended tetrathiafulvalene derivatives. *J. Mater. Chem.*, 19:3648–3651, 2009.
- [34] Kunpeng Guo, Keyou Yan, Xiaoqing Lu, Yongcai Qiu, Zhike Liu, Jianwei Sun, Feng Yan, Wenyue Guo, and Shihe Yang. Dithiafulvenyl unit as a new donor for high-efficiency dye-sensitized solar cells: synthesis and demonstration of a family of metal-free organic sensitizers. *Org. Lett.*, 14:2214–2217, 2012.
- [35] Kunpeng Guo, Junli Yang, Xiaofan Shi, Xiaoqing Lu, Jun Cheng, Yuling Wu, Yun Guo, and Hua Wang. A  $\pi$ -extended tetrathiafulvene derivative: Synthesis and photoluminescence properties. *Mater. Chem. Phys.*, 146:193–197, 2014.
- [36] Christian R. Parker, Edmund Leary, Riccardo Frisenda, Zhongming Wei, Karsten S. Jennum, Emil Glibstrup, Peter Bæch Abrahamsen, Marco Santella, Mikkel A. Christensen, Eduardo Antonio Della Pia, Tao Li, Maria Teresa Gonzalez, Xingbin Jiang, Thorbjørn J. Morsing, Gabino Rubio-Bollinger, Bo W.

- Laursen, Kasper Nørgaard, Herre van der Zant, Nicolas Agrait, and Mogens Brøndsted Nielsen. A comprehensive study of extended tetrathiafulvalene cruciform molecules for molecular electronics: synthesis and electrical transport measurements. *J. Am. Chem. Soc.*, 136:16497–16507, 2014.
- [37] Zhongming Wei, Tim Hansen, Marco Santella, Xintai Wang, Christian R. Parker, Xingbin Jiang, Tao Li, Magni Glyvradal, Karsten Jennum, Emil Glibstrup, Nicolas Bovet, Xiaowei Wang, Wenping Hu, Gemma C. Solomon, Mogens Brøndsted Nielsen, Xiaohui Qiu, Thomas Bjørnholm, Kasper Nørgaard, and Bo W. Laursen. Molecular heterojunctions of oligo(phenylene ethynylene)s with linear to cruciform framework. *Adv. Func. Mater.*, 25:1700–1708, 2015.
- [38] Karimulla Mulla and Yuming Zhao. When dithiafulvenyl functionalized pi-conjugated oligomers meet fullerenes and single-walled carbon nanotubes. *J. Mater. Chem. C*, 1:5116–5127, 2013.
- [39] Tracey M. Clarke, Keith C. Gordon, David L. Officer, and Daina K. Grant. The effect of oxidation on the structure of styryl-substituted sexithiophenes: A resonance Raman spectroscopy and density functional theory study. *J. Chem. Phys.*, 124:164501, 2006.
- [40] John C. Earles, Keith C. Gordon, David L. Officer, and Pawel Wagner. A spectroscopic and computational study of the neutral and radical cation species of conjugated aryl-substituted 2,5-bis(2-thien-2-ylethenyl)thiophene-based oligomers. *J. Phys. Chem. A*, 111:7171–7180, 2007.
- [41] Reyes Malave Osuna, Rocio Ponce Ortiz, Victor Hernández, Juan Teodomiro Lopez Navarrete, Makoto Miyasaka, Suchada Rajca, Andrzej Rajca, and Rainer Glaser. Helically annelated and cross-conjugated beta-

- oligothiophenes: a fourier transform Raman spectroscopic and quantum chemical density functional theory study. *J. Phys. Chem. C*, 111:4854–4860, 2007.
- [42] Sandra R. González, Yutaka Ie, Yoshio Aso, Juan T. López Navarrete, and Juan Casado. The frontiers of quinoidal stability in long oligothiophenes: Raman spectra of dicationic polaron pairs. *J. Am. Chem. Soc.*, 133:16350–16353, 2011.
- [43] M. J. Frisch, G. W. Trucks, H. B. Schlegel, G. E. Scuseria, M. A. Robb, J. R. Cheeseman, G. Scalmani, V. Barone, B. Mennucci, G. A. Petersson, H. Nakatsuji, M. Caricato, X. Li, H. P. Hratchian, A. F. Izmaylov, J. Bloino, G. Zheng, J. L. Sonnenberg, M. Hada, M. Ehara, K. Toyota, R. Fukuda, J. Hasegawa, M. Ishida, T. Nakajima, Y. Honda, O. Kitao, H. Nakai, T. Vreven, J. A. Montgomery, Jr., J. E. Peralta, F. Ogliaro, M. Bearpark, J. J. Heyd, E. Brothers, K. N. Kudin, V. N. Staroverov, R. Kobayashi, J. Normand, K. Raghavachari, A. Rendell, J. C. Burant, S. S. Iyengar, J. Tomasi, M. Cossi, N. Rega, J. M. Millam, M. Klene, J. E. Knox, J. B. Cross, V. Bakken, C. Adamo, J. Jaramillo, R. Gomperts, R. E. Stratmann, O. Yazyev, A. J. Austin, R. Cammi, C. Pomelli, J. W. Ochterski, R. L. Martin, K. Morokuma, V. G. Zakrzewski, G. A. Voth, P. Salvador, J. J. Dannenberg, S. Dapprich, A. D. Daniels, ?. Farkas, J. B. Foresman, J. V. Ortiz, J. Cioslowski, and D. J. Fox. Gaussian 09 Revision D.01. Gaussian Inc. Wallingford CT 2009.
- [44] Axel D. Becke. A new mixing of Hartree-Fock and local density-functional theories. *J. Chem. Phys.*, 98:1372–1377, 1993.
- [45] Erich Runge and E. K. U. Gross. Density-functional theory for time-dependent systems. *Phys. Rev. Lett.*, 52:997–1000, 1984.

- [46] Roy Dennington, Todd Keith, and John Millam. GaussView Version 5. Semichem Inc. Shawnee Mission KS 2009.
- [47] Jacopo Tomasi, Benedetta Mennucci, and Roberto Cammi. Quantum Mechanical Continuum Solvation Models. *Chemical Reviews*, 105(8):2999–3094, 2005.
- [48] Miklos. Kertesz and Yong S. Lee. Energy gap and bond length alternation in heterosubstituted narrow gap semiconducting polymers. *J. Phys. Chem.*, 91:2690–2692, 1987.
- [49] J. L. Brédas. Relationship between band gap and bond length alternation in organic conjugated polymers. *J. Chem. Phys.*, 82:3808–3811, 1985.
- [50] J. Roncali. Molecular Engineering of the Band Gap of  $\pi$ -Conjugated Systems: Facing Technological Applications. *Macromol. Rapid Commun.*, 28:1761–1775, 2007.
- [51] R. G. Bates and V. E. Bower. *J. Res. Natl. Bur. Stand.*, 53:283–290, 1954.
- [52] Alan E. Reed, Robert B. Weinstock, and Frank Weinhold. Natural population analysis. *J. Chem. Phys.*, 83:735–746, 1985.
- [53] M. Wojdyr. Fityk: a general-purpose peak fitting program. *J. Appl. Cryst.*, 43:1126–1128, 2010.

# Chapter 3

## Adsorption of Dithiafulvene

### Derivatives on an Au (111):

### Orientational Geometry, Binding

### Energies and Work Function

#### 3.1 Introduction

For decades the interplay between organic molecules and various metal surfaces has drawn considerable research attention, since the electronic properties of metal surfaces (*e.g.*, work function) can be readily altered and controlled by surface functionalization with self-assembled monolayers (SAMs) of rationally designed molecules [1, 2]. Fundamental understanding of this phenomenon has greatly enriched the methodologies for modifying metal surfaces with specific functionalities, which in turn lead to wide applications in nanomaterials, molecular optoelectronic devices, and catalysis [3, 4].

Sulfur-containing  $\pi$ -conjugated heterocycles such as thiophene, dithiafulvene (DTF),

and tetrathiafulvalene (TTF) are  $\pi$ -electron donors that are often used as building blocks for the preparation of organic conducting and semiconducting oligo-/polymers. Over the past few years, the adsorption behavior of thiophenes, TTFs and relevant aromatic molecules on noble metal surfaces has been subject of active experimental and theoretical investigations [5–7]. The interactions between these organic molecules and metal surfaces lead to significantly modulated surface properties, such as work function ( $\varphi$ ), metal-organic junction, and charge injection/transport, which are crucial to the performance of thin film and molecular (opto-)electronic devices [8,9]. Recent theoretical studies have disclosed that density functional theory (DFT) calculations taking van der Waals exchange correlations into account and using localized basis sets could describe the adsorption behavior of these aromatic molecules on metal surfaces in a qualitatively good agreement with experimental results [5]. It is reported that when thiophene or TTF is adsorbed on a metal surface (e.g., Au (111) or Cu(111)) at a low surface coverage, the molecule interacts with the surface in a “flat lying” fashion. With increased surface coverage, a tilted orientation becomes more favored for the surface-bound molecules [10].

As the half structure of TTF, dithiafulvene (DTF) also presents an excellent organic  $\pi$ -electron donor system, since it can form an aromaticity-stabilized radical cation after releasing one electron. Unlike thiophene and TTF, there have been no systematic studies on the interactions of DTF with noble metal surfaces in the current literature. Many known DTF derivatives carry an arene moiety (e.g., phenyl, naphthyl, and pyrenyl) directly connected to the DTF group due to their synthetic accessibility. Such a motif allows the DTF derivatives to act as redox-active building blocks in constructing complex  $\pi$ -conjugated oligomers, polymers, and macrocycles. It can be readily envisioned that the arene unit in conjugation with DTF should give rise to intriguing interactions with metal surfaces through various organic-metal

binding forces. A detailed study is therefore warranted to establish the fundamental understanding on DTF–metal interactions as well as to seek potential applications of DTF derivatives in surface science and nanotechnology.

At the outset of this study, a carboxylated phenyl-DTF **3a** (Figure 3.1) was chosen as a model compound for examination. Both theoretical modeling and experimental analysis were carried out to characterize its adsorption behavior on an Au (111) surface. Compound **3a** was previously synthesized by Wang and Zhao as a building block for redox-active coordination polymers, while the carboxylic group was designed to serve as a ligand for binding with transition metal ions. In this work, it was anticipated that the adsorption behavior of DTF **3a** on an Au (111) surface would be dictated by three major binding forces: van der Waals, Au–S and Au–COOH interactions. Depending on the significance of each binding force, the possible binding modes of **3a** on an Au (111) were proposed to be “face-on”, “edge-on”, and “vertical” as depicted in Figure 3.1B–E. It was also hypothesized that charge transfer between DTF **3a** and an Au (111) surface occurs to induce surface-enhanced Raman scattering (SERS) effects, which might be of great interest to the research on chemical sensing at organic-metal interfaces. The following sections describe the details addressing the aspects mentioned above utilizing DFT calculations, Kelvin probe force microscopy (KPFM), and Raman spectroscopic analyses.

## 3.2 Computational Methodology

### 3.2.1 Modeling the Gas-Phase Properties of DTF **3a**

Density functional theory (DFT) calculations on the structural and electronic properties of compound **3a** in the gas phase were conducted at the B3PW91/6-31+G(d,p) level of theory [11] using the Gaussian 09 software package [12]. First, an optimized

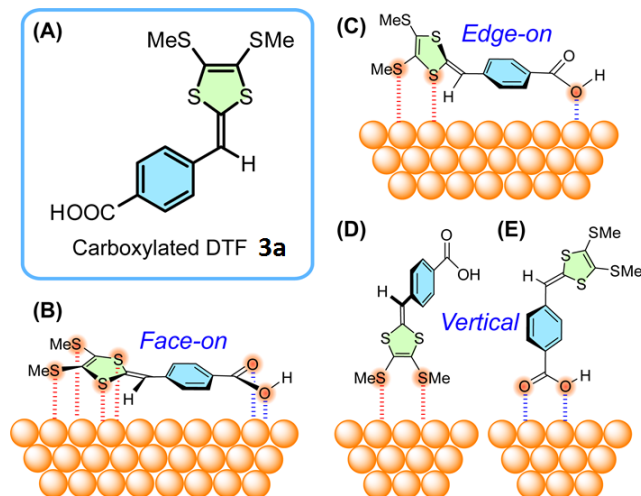


Figure 3.1: (A) Molecular structure of carboxylated DTF **3a**, and (B)–(E) four possible modes by which **3a** can be bound to a metal surface.

geometry of **3a** was computed and validated by frequency calculations to confirm that it is indeed the ground state (i.e., zero imaginary frequencies). Raman spectroscopic properties were then calculated with the optimized structure. Simulated Raman spectra and vibrational modes were visualized by GaussView 5 [13].

Figure 3.2 depicts the optimized structure of DTF **3a** in the gas phase. As can be seen, DTF **3a** is not totally planar and there is a dihedral angle of  $1.47^\circ$  between  $C_4-C_5-C_3-S_1$ . Molecular orbitals show that the HOMO is highly concentrated over the  $C_4$ ,  $C_3$ ,  $S_1$  and  $S_2$  atoms, which are involved in electron donating and the oxidation reaction. Furthermore, the LUMO is mainly localized over the benzene ring.

### 3.2.2 Modeling the Adsorption Behavior of DTF **3a** on an Au (111) Surface

DFT calculations on the adsorption behavior of compound **3a** on the Au (111) surface were carried out using the VASP 5.4.1 software package. Periodic calculations were implemented based on the plane wave density functional theory within the projected

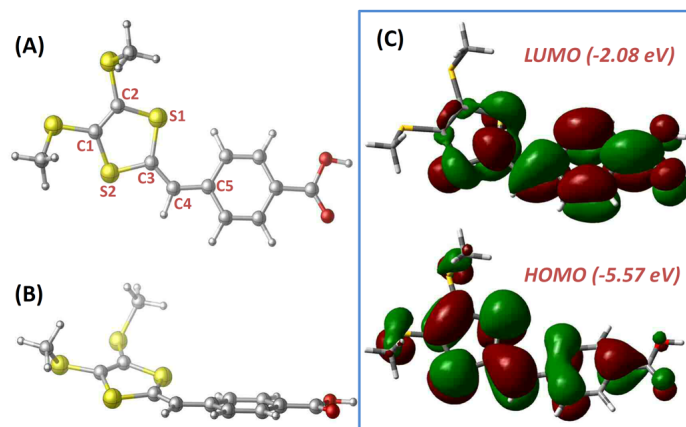


Figure 3.2: (A) and (B) Optimized structure of DTF **3a**, which represents a dihedral angle of 1.47 degrees between the planes of C<sub>4</sub>-C<sub>5</sub> and C<sub>3</sub>-S<sub>1</sub>. (C) Representation of the highest occupied and lowest unoccupied molecular orbitals of DTF **3a**

augmented wave (PAW) to take into account the effect of core electrons on the valence shell with the plane wave basis set to consider the valence electronic states. The electron densities of non-dispersion calculations were obtained by using the generalized gradient approximation (GGA), with an exchange-correlation functional of Perdew, Burke and Enzerhof (PBE) [14–16]. The effect of the dispersion interactions was considered by the use of optB86b-vdW functional [14,17–21] to include the non-local nature of electron correlation. The gold slab, DTF **3a** and the slab with the DTF **3a** deposited on top were allowed to relax for geometry optimization until all forces were smaller than 0.01 eV/Å [22]. The cut-off energy of 400 eV was used for all calculations. The gamma point was found to be sufficient for Monkhorst Pack of the integrals in the Brillouin zone in energy convergence. All outputs were visualized by Virtual NanoLab version 2015.1.

The geometry of DTF **3a** optimized by DFT calculations in the gas phase was used for further optimization in large enough unit cells to avoid any interactions between nearby molecules. Cell dimensions of the isolated molecule were optimized in three directions to obtain the optimized cell dimensions in which nearby molecules do

not interact with one another (Appendix C). Results with and without considering the dispersion correction show that the energy of the single molecule in the unit cell reaches a plateau at  $20 \times 15 \times 15$  and remains consistent by increasing the cell dimensions. Therefore, the lattice parameters of  $(\alpha, \beta, \gamma = 90)$  and  $(a = 20, b = 15, c = 15)$  were adopted for the rest of the calculations to save computational costs. The top layer of the gold slab and the molecule were allowed to relax until all forces were smaller than  $0.01 \text{ eV}/\text{\AA}$  for all relaxation convergences [22].

The FCC crystal structure of Au with lattice parameters of  $(\alpha, \beta = 90, \gamma = 120)$  and  $(a = 20, b = 15, c = 15)$  were optimized with PAW-DFT. The output was then utilized building the four layers of 111 surface of the  $p(1 \times 1)$  unit cell. The electronic wave functions were sampled in a k-point grid of  $21 \times 21 \times 21$  and  $5 \times 5 \times 1$  for both FCC crystal and slab structures. The calculated FCC lattice constant was found to be 4.078, which almost matches the experimental value of 4.080. Two to six layers and 15 to 20  $\text{\AA}$  of vacuum thickness on top of the slab were examined to achieve efficient slab and vacuum thicknesses. The choice of the number of layers was decided based on the comparison of the lattice constants and the total density of states of the middle layer of the slab versus total density of state (DOS) of the bulk (Figure 3.3). In all cases, the local DOS of the middle layer must match the bulk DOS. Moreover, the vacuum should be thick enough so that the adsorbent on the top does not interact with the surface in the cell above it. Eventually, four layers of Au (111) along with a vacuum of 18  $\text{\AA}$  in the z direction were employed to simulate a real slab structure.

The optimized DTF **3a** was then positioned on the Au (111) surface for further optimization. Since the simulation of the metal-organic interface needs an appropriate initial geometry for the organic compound and substrate, a variety of initial orientation geometries was evaluated and summarized in Figures 3.1 and 3.6 (more details can be found in Appendix C). An internal layer Au–Au bond of the second

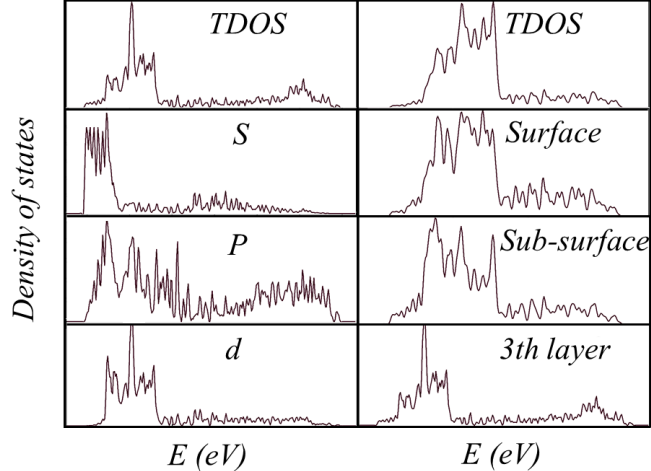


Figure 3.3: Total and projected density of states of (left) the bulk (right) and the Au (111). Total DOS of bulk closely matches the local DOS of the third layer of the slab. The numbering of the layers in the slab starts from the closest slab to the adsorbent.

and third layer of the gold slab was calculated to be  $2.51 \text{ \AA}$  with and without the dispersion correction being considered. The theoretically calculated data matches the actual bond distance very well.

Because a perfectly ordered gold surface was used in the simulations, some discrepancies between the calculated and experimental work functions were expected, since the actual gold surface inevitably contains defects and disordered domains. Nevertheless, the gold substrates used in the experimental work are quite densely packed metal surface and should give experimental results reasonably consistent with the theoretical data.

### 3.3 Experimental Details

KPFM was performed at atmospheric pressure and room temperature using an MFP-3D (Asylum Research) atomic force microscope (AFM), with a gold/platinum tip (40 KHz, MikroMasch-CSC35) operating in the tapping mode at a scan rate of 0.1 Hz. The work function was calculated using the method implemented in the Asylum

Research software. In this technique, an electrostatic force between a conductive tip and the sample is generated by applying an AC voltage of 1 mV to the sample. The electrostatic forces are adjusted by a DC bias to match the contact potential difference (CPD) between the tip and the sample. The work function of the sample can be calculated by the sum of the work function of the cantilever and the contact potential difference (Equation 3.1). The work function of the cantilever is calibrated according to the known work function of highly ordered pyrolytic graphite (HOPG) at 4.60 eV [23]. The CPD value of the HOPG is measured to be 0.17 eV. The work function of the tip can be determined by Equation 3.2 [24].

$$CPD = \varphi_{(tip)} - \varphi_{(sample)} \quad (3.1)$$

$$\varphi_{(sample)} = 4.60eV + CPD_{(HOPG)} - CPD_{(sample)} \quad (3.2)$$

X-ray diffraction (XRD) characterization ran by the Rigaku Ultima-IV instrument using Cu K- $\alpha$  radiation. Raman spectroscopic analysis of the thin film of DTF **3a** was conducted on a Renishaw spectrometer excited at a wavelength of 633 nm.

### 3.4 Sample Preparation

Gold substrates with a thickness of 15 nm were prepared in a vacuum metal evaporator built in the Merschrod lab. Gold wires were evaporated on cleaned glass slides under a vacuum of  $10^{-4}$  bar. The surface topography of one of these gold substrates was examined by AFM, showing the presence of gold nano-islands across the surface. X-ray powder diffraction of the gold surface reveals the Au (111) crystal orientation on the surface (Appendix C).

DTF **3a** was synthesized according to the reported procedures by Wang and Zhao

[25]. A solution of this compound was prepared by adding 0.1 mg [304.61  $\mu$ mol] of DTF **3a** to 2 mL of organic solvent (methanol or toluene). Thin films of DTF **3a** were prepared by drop-casting the solution on gold substrates. Methanol and toluene were used to prepare the AFM and Raman samples, respectively.

## 3.5 Results and Discussion

### 3.5.1 Crystallographic and Topographic Properties

Figure 3.4 shows the X-ray diffraction (XRD) patterns of the gold substrate with a thickness of 15 nm. The peak at  $37.5^\circ$  is in line with the Au (111) structure. It therefore confirms that the Au (111) model used in the theoretical simulations is a reasonable choice.

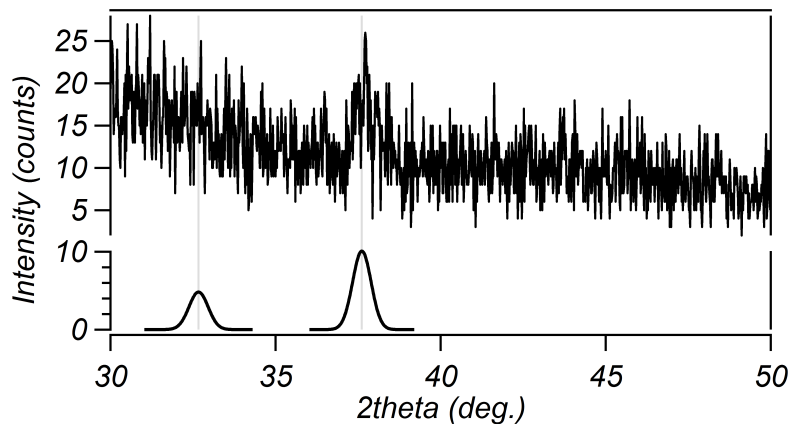


Figure 3.4: XRD patterns of the gold substrate prepared experimentally.

Figure 3.5A and B shows the representative AFM topography of the gold substrate before and after depositing a thin film of DTF **3a** on it. For comparison purpose, the AFM image of DTF **3a** thin film deposited on a glass slide is provided in Figure 3.5C.

It can be clearly seen from the AFM image of the bare gold substrate (Figure 3.5B)

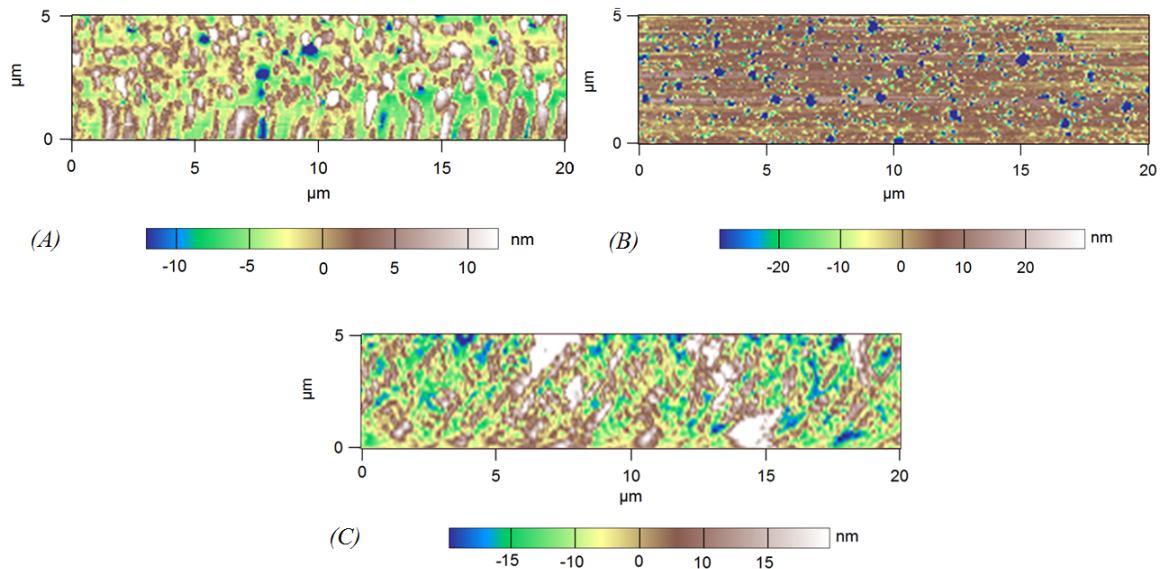


Figure 3.5: AFM topography of (A) the bare gold substrate, (B) the gold substrate with a thin film of DTF **3a** deposited on top of it, and (C) the thin film of DTF **3a** deposited on a glass slide.

that discrete gold nano-islands are distributed all over the surface. The thin film of **3a** deposited on the gold surface of gold substrate appears to assemble in a higher uniformity than the thin film on glass slide. The better film forming behavior on gold can be ascribed to the attraction between the  $\pi$ -electron density of **3a** and a gold surface. In the meantime, the presence of sulfur atoms in DTF **3a** also engenders Au–S interactions to enhance the binding to the gold surface. For the thin film on the glass slide, the molecule/substrate interactions are not as significant. As a result, the thin film topology shows randomly aggregated clusters rather than ordered features.

### 3.5.2 Geometric and Energetic Properties of DTF **3a** on a Gold Surface

The binding energy of each DTF **3a** adsorbed on the Au (111) surface was calculated according to Equation 3.3,

$$E_B = E_{SA} - (E_A + E_S) \quad (3.3)$$

where  $E_B$  is the calculated binding energy,  $E_A$  is the total energy of the adsorbent molecule,  $E_S$  is the total energy of the slab and  $E_{SA}$  is the total energy of the slab with the adsorbent molecule on the top of it. The total energy is the electronic component without taking vibrational energies into account. The calculated binding energies along with the corresponding Fermi energies, with and without considering the dispersion correction, are provided in Appendix C.1. The absolute value of a binding energy calculated with consideration of dispersion correction is much higher than that calculated without dispersion correction.

The computational results indicate that among the several possible binding modes, the face-on orientation gives rise to the strongest binding energy (with and without the dispersion correction). Indeed, the face-on interaction allows the sulfur atoms of the DTF to lie closer to the surface, achieving a synergistic effect of the strong S–Au and  $\pi$ –Au attractions. Figure 3.6 illustrates two calculated geometries of a DTF molecule adsorbed on the surface of a Au (111) slab, namely face-on and edge-on modes.

On considering the van der Waals (vdW) interactions, the binding energies of DTF **3a** on Au (111) surface are calculated to be  $-3.20$  eV (face-on) and  $-3.01$  eV (edge-on) respectively. Calculations with consideration of vdW interactions give binding energies of  $-0.28$  eV (face-on) and  $-0.11$  eV (edge-on). In both cases, face-on binding

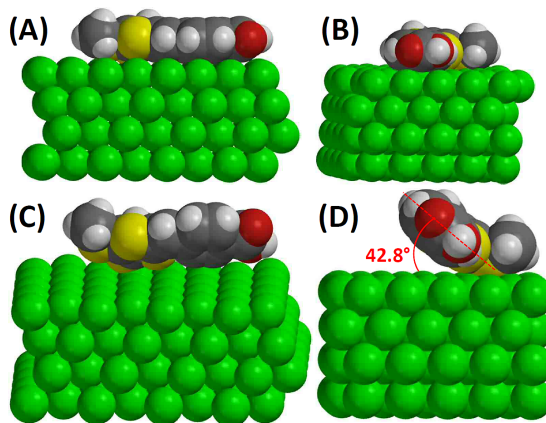


Figure 3.6: Optimized structure of DTF **3a** deposited on the surface of the Au (111). (A) and (B) show the face-on orientation at two different side views, (C) and (D) show two views of the edge-on orientation with a  $42.8^\circ$  angle between the plane of the benzene ring and the surface of the slab.

appears to be more energetically favored over the edge-on binding by *ca.* 0.2 eV. The non-covalent forces such as vdW seems to be a major contributor to the binding energy. Generally speaking, a binding energy higher than 1.3 eV is considered to be a strong adsorption [26].

Calculations with the dispersion correction show that the  $S_1$ -slab distance is at 2.86 Å, while the  $SCH_3$  connected to  $C_1$  is at a closer distance of 2.55 Å to the slab. Since the covalent Au-S bond distance is reported to be 2.46 Å [27], it is reasonable to believe that the interactions of all the S atoms in DTF **3a** with Au (111) surface are of partial covalent bonding character. The dihedral angle between the  $S_1-C_3$  and  $C_4-C_5$  bonds is calculated to be  $6.9^\circ$  for the single molecule of DTF **3a** in the unit cell and  $4.8^\circ$  when it is deposited on Au (111) surface. The central dihedral angle is decreased by  $2.1^\circ$  after binding to Au (111) surface, resulting in a more flattened shape of DTF **3a** to gain stronger face-on interactions with the gold slab.

To assess the contribution of the  $SCH_3$  side groups to the binding energy, an analogous DTF molecule to **3a** without the presence of  $SCH_3$  substituents on  $C_1$  and  $C_2$  was also calculated. The results show that the unsubstituted DTF molecule interacts

with the Au (111) surface to give a binding energy of  $-3.20$  eV (with dispersion correction) or  $-0.29$  eV (without dispersion correction). Upon comparing the binding energies calculated for SCH<sub>3</sub>-substituted DTF **3a**, the effects of SCH<sub>3</sub> groups on the binding energy can be deemed as negligible.

### 3.5.3 Raman Evidence for Geometrical Orientation

A Raman spectrum of the Au (111) substrate were taken before and after depositing the solutions of DTF **3a** at different concentrations on the surface (shown in Figure 3.7). As can be seen, the spectrum of the DTF **3a** powder (Figure 3.7–B) matches very well the simulated spectrum of the compound in the neutral state (Figure 3.7–A). The calculated C=O stretching peak at  $1800\text{ cm}^{-1}$  is not observed in the experimental spectra of DTF **3a** measured in bulk solids and on Au (111) surface. The exact reason for the disappearance of the C=O stretching band has not been fully clarified. Intermolecular hydrogen bonding interactions through the carboxyl groups of DTF **3a** could be an important factor. The Raman spectrum of the bare gold can be found in Appendix C.

The intensity of the broad experimental peak at  $1451\text{ cm}^{-1}$  increases upon decreasing the concentration of the compound, which corresponds to the C=C bond stretching of the benzene ring in the oxidized state. While the rest of the spectrum agrees well with the spectrum of the neutral state, which can describe a partially oxidized nature over the molecule due to the charge transfer between the gold substrate and the compound (computational and experimental Raman spectra of DTF **3a** in the oxidized state are shown in Figure 4.8). Furthermore, the intensity of the peak at  $505\text{ cm}^{-1}$  is observed to significantly increase with decreasing concentration of the compound. The relative intensity of the  $505\text{ cm}^{-1}$  peak reaches its highest at the lowest concentration of DTF **3a** after washing the surface with deionized water. The

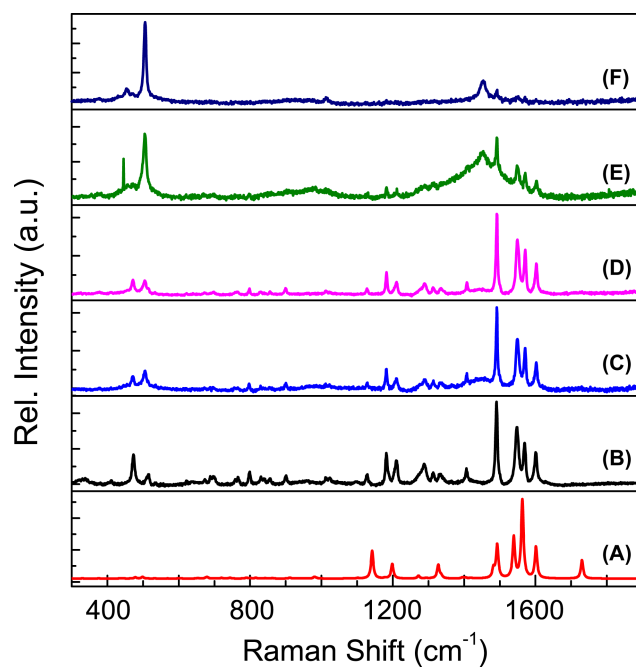


Figure 3.7: (A) Simulated Raman spectrum of DTF **3a** in the gas phase obtained by B3PW91/6-31+G(d,p) level of theory. (B) Raman spectrum of the pure compound in the solid state. (C–F) Raman spectrum of the DTF **3a** on the surface of 15 nm Au (111) at different concentrations, starting from the lowest concentration on the bottom.

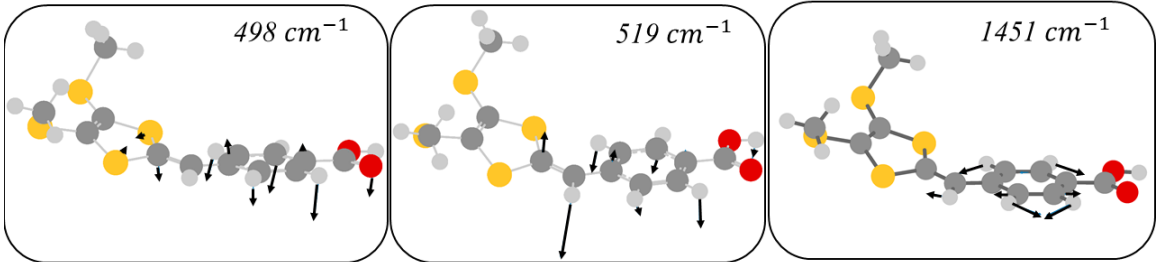


Figure 3.8: Vibrational modes of calculated peaks at 498, 519, 1453  $\text{cm}^{-1}$ .

corresponding peak is shifted to higher frequency for the bulk, which is assigned to the out-of-plane vibrational modes of benzene and five member rings. The intensity of the peaks mentioned above are greatly enhanced on the surface gold due to the electronic interaction of molecular electron cloud and gold orbitals. The vibrational modes of enhanced peaks are shown in Figure 3.8.

In-plane and out-of-plane vibration of the benzene ring is involved in all four peaks. The results show that the molecule is bonded to the surface through the conjugated  $\pi$ -electron cloud.

### 3.5.4 Work Function Modification

The work function of the gold substrate was calculated with and without considering the dispersion correction. Experimentally, the work function was measured before and after the deposition of the solution of DTF **3a**. The work function ( $\varphi$ ) is determined by Equation 3.4.

$$\Phi = E^{vac} - \epsilon_F \quad (3.4)$$

$E^{vac}$  is the vacuum potential and  $\epsilon_F$  is the Fermi level energy. The work function of gold (FCC) is calculated to be 5.63 (5.67) eV, and the reported value is 5.30 eV [28]. Furthermore, the KPFM results show a value of 5.03 eV for the bare Au (111) substrate, which is calculated to be 3.66 (3.57) eV and is reported as 4.72 eV in

the literature [29–31]. The measured work function of DTF **3a** on the glass slide is found to be 4.47 eV, which closely agrees with the calculated values with and without the dispersion correction (4.43 (4.52) eV). The work function of DTF **3a** at different adsorption orientations on the Au (111) was calculated to be  $3.30 \pm 0.1$  ( $3.40 \pm 0.1$ ) eV, which was measured to be 4.88 eV by the KPFM technique. The results indicate that the molecular orientation does not impact the  $\Phi$  values (all results are reported in Appendix C). Moreover, the work function of the substrate decreases both computationally and experimentally for 0.36 (0.17) and 0.15 eV, respectively. Therefore, a thin film of DTF derivatives can be deposited on the gold surface to modify the work function and electronic levels.

By removing the SCH<sub>3</sub> groups on C<sub>1</sub> and C<sub>2</sub> atoms, the molecular work function is calculated to be 4.50 (4.50) eV, while the work function of the gold substrate with DTF deposited on top of it is computed to be 3.34 (3.41) eV. The absence of SCH<sub>3</sub> groups leads to a slight decrease in the work function of the gold substrate by 0.32 (0.16) eV. It can therefore be concluded that the SCH<sub>3</sub> groups do not play a major role in modifying the work function of the substrate.

### 3.5.5 Charge Distribution

Adsorption of an organic  $\pi$ -conjugated molecule on the surface of a noble metal results in hybridization and charge re-distribution between the molecule and the metal surface. The charge density differences in the Z direction ( $\rho_Z$ ) are obtained with Equation 3.5.

$$\rho_Z = \rho_{\mathbf{3a-Au}} - (\rho_{\mathbf{3a}} + \rho_{Au}) \quad (3.5)$$

Herein  $\rho_{\mathbf{3a-Au}}$  is the charge density of the adsorbed DTF **3a** on an Au (111),  $\rho_{\mathbf{3a}}$

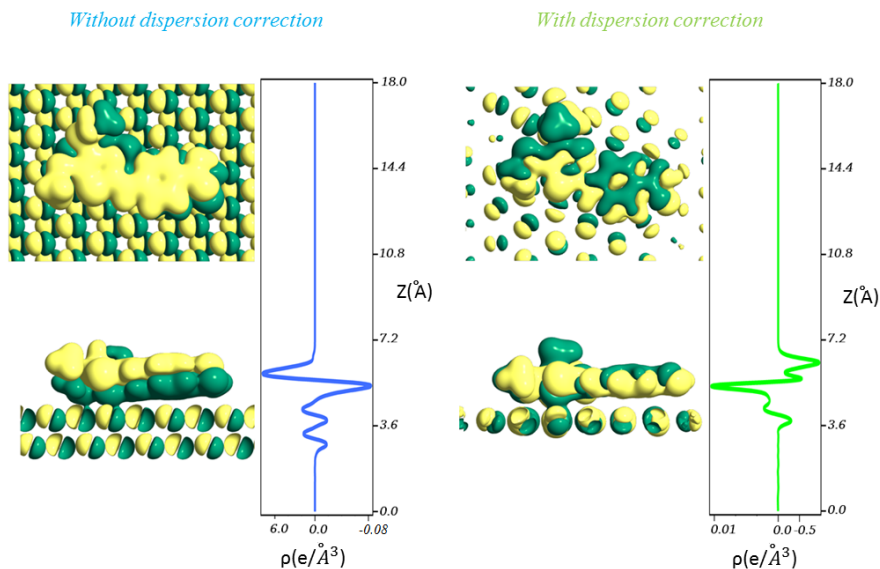


Figure 3.9: Iso-surfaces of difference charge distributions over adsorbent and surface at the top and side view with and without considering vdW interactions. The negative area (green) shows the gaining of electrons, and the positive area (yellow) indicates the production of holes. The plot of charge distribution versus distance in the z-axis can be seen on the right side of each type of calculation which is aligned with the side view of the iso-surfaces.

and  $\rho_{Au}$  are the charge densities of the molecule and gold surface, respectively. The charge difference iso-surfaces with and without considering the dispersion correction are shown in Figure 3.9.

As can be seen in Figure 3.9 (right), only the first layer of the gold slab is involved in charge perturbation with dispersion correction considered. Besides, the negative charge migrates over the benzene ring and  $S_1$  while the hole or positive charge appeared on  $S_2$ , which matches very well the lowest unoccupied molecular orbital (LUMO).

The charge density fluctuates over a much greater range of  $+6.0$  and  $-0.08$   $e/\text{\AA}^3$  in the calculation without dispersion correction, which compares to  $+0.01$  to  $-0.1$   $e/\text{\AA}^3$  for the calculations with considering vdW interactions. The calculations without dispersion correction show that the first two layers of the gold slab are involved in

charge distribution and the clear charge separation over the molecule and surface. Most of the changes occurs over the molecule than the substrate. It can be concluded that the calculations considering vdW interactions can significantly impact the charge distribution. Furthermore, calculations with considering dispersion correction show that transfer of negative charges occurs from the slab to the molecule.

### 3.5.6 Impact of Terminal Group on Electronic Properties

The impact of the substituents in the DTF molecule on the binding energy and electronic properties were investigated. As mentioned in Section 3.5.4, the orientational geometry does not impact the work function. Therefore, the face-on orientation, in which the dithiole ring is parallel to the surface of the slab, has been chosen for studying the substituent effects on electronic properties. The list of Au–S<sub>1</sub> distances for optimized structures of DTF derivatives deposited on the gold surface is given in Appendix C

Adsorption energy is defined as the difference of the Au (111) work functions before and after deposition of a DTF molecule. Detailed adsorption energy values for DTF derivatives with six different substituents are calculated and listed in Table 3.1. Molecular work function and polarizability values are provided in Appendix C.

	$\mu_{tot}$	$E_B$	$\Phi_{DTF-Au}$	$\Phi_{Au} - \Phi_{DTF-Au}$
NO <sub>2</sub>	8.1	-3.17 (-0.33)	3.36 (3.40)	0.30 (0.17)
CN	7.2	-4.02 (-0.39)	3.26 (3.35)	0.40 (0.22)
CHO	5.8	-3.02 (-0.14)	3.37 (3.42)	0.29 (0.15)
OCH <sub>3</sub>	3.7	-3.24 (-0.29)	3.35 (3.36)	0.31 (0.21)
Br	4.0	-3.24 (-0.49)	3.36 (3.37)	0.30 (0.20)
NH <sub>2</sub>	3.4	-3.51 (-0.38)	3.35 (3.37)	0.31 (0.20)

Table 3.1: Adsorption energies ( $E_B$ ), work function of the Au (111) with deposited DTF on top ( $\Phi_{DTF-Au}$ ) and the magnitude of drop in the work function of the Au (111) by deposition of DTF ( $\Phi_{Au} - \Phi_{DTF-Au}$ ) with six different substituents (all values are reported in eV). The electric dipole moments ( $\mu_{tot}$ ) of the single molecule in the gas phase are investigated with B3LYP/6-31++G(d,p) level of theory.

Comparison of the binding energies shows that the dipole moments of the DTF molecules are correlated to the binding energies. Calculations that include dispersion correction show that the highest absolute value of binding energy belongs to the DTF with CN substituent. The DTF with a CHO substituent has the weakest binding affinity for the gold surface. The relatively high adsorption energies of the DTFs with nitrogen-containing substituents, such as NO<sub>2</sub>, CN and NH<sub>2</sub>, suggest that nitrogen can significantly contribute to the binding with the Au (111).

Comparison of the work function values shows that the work function can be varied up to 0.1 eV by changing the substituent at the para position of the benzene ring. The largest change in the work function is obtained by deposition of the DTF with CN substituent. Furthermore, DTFs with CN and CHO show the highest and lowest work functions, respectively.

The work function of the gold substrate changes as a function of the molecular dipole moment of the DTF adsorbent, as a result of the formation of SAMs on the substrate. There is a linearly proportional relationship between the work function and the molecular dipole moment as described in Equation 3.6 [1].

$$\Delta\varphi_{mol} = -\frac{e\mu_{Z,mol}}{\epsilon_o A_\Theta} \Theta = -\frac{e\mu_{o,mol} \cos(\beta)}{\epsilon_o \epsilon_{eff} A_\Theta} \Theta \quad (3.6)$$

$\mu_{Z,mol}$  is the Z component of molecular dipole,  $\mu_{o,mol}$  is the molecular dipole moment,  $\beta$  is the tilt angle between the z axis through metal slab and the molecular axis,  $\epsilon_o$  is the vacuum permittivity,  $\Theta$  is the surface coverage,  $\epsilon_{eff}$  is the effective parameter that is dependent on the surface coverage and  $A_\Theta$  is the area of the unit cell at the p(1×1) surface. So the higher molecular polarizability can lead to the easiest circulation of loosely bound electron cloud over the molecule, which in turn results in a better hybridization with the substrate. In our study, the binding energies do not show a direct correlation with polarizability. Possibly, some other factors such as the

binding of the substituent to the substrate (face-on orientation on the gold surface) also come into play in addition to the polarizability effect.

### 3.5.7 Substituent Effect on Charge Distribution

The plots of differences in charge distribution through z-axis along with iso-surfaces for all DTF derivatives are shown in Figure 3.10 (iso-surfaces that are obtained without considering vdW interactions are reported in Appendix C).

Iso-surfaces of all derivatives indicate that the electrons migrate over the substituent on the benzene ring and  $S_1$ . The iso-surface at the interface of the molecule and the slab illustrates that the charge migration occurs between the molecule and the substrate, which happens through the dithiole side in all cases. Results show that the interlayer of the slab is also involved in the charge distribution, which could be attributed to the higher molecular polarizability as discussed in the previous section. Except DTF **3a**,  $S_1$  and  $C_1$  gain a hole in all other DTF derivatives, whereas  $C_4$  loses an electron in all molecules including DTF **3a**. The DTF with the CN substituent shows a slight fluctuation near zero in the range of  $-0.1$  to  $+0.1$   $e/\text{\AA}^3$ , while the other DTF molecules shows charge density differences in the range of  $-1.0$  to  $+1.0$   $e/\text{\AA}^3$ .

Figure 3.11 shows the iso-surfaces and plots of integrated charge density changes through the z-axis obtained by calculation without considering vdW interactions. As can be seen, a clear charge separation occurs over the molecule and surface. The common point between the calculations with and without the dispersion correction is that the interlayers are involved in the charge distribution for all DTF derivatives except DTF **3a**. The major difference is that the charge density fluctuates at much higher range from  $-4$  to  $+4$   $e/\text{\AA}^3$ . The highest charge density is distributed over the molecule rather than the slab. Therefore, vdW interactions play a major role in the charge distribution and should be considered in further studies on charge transfer

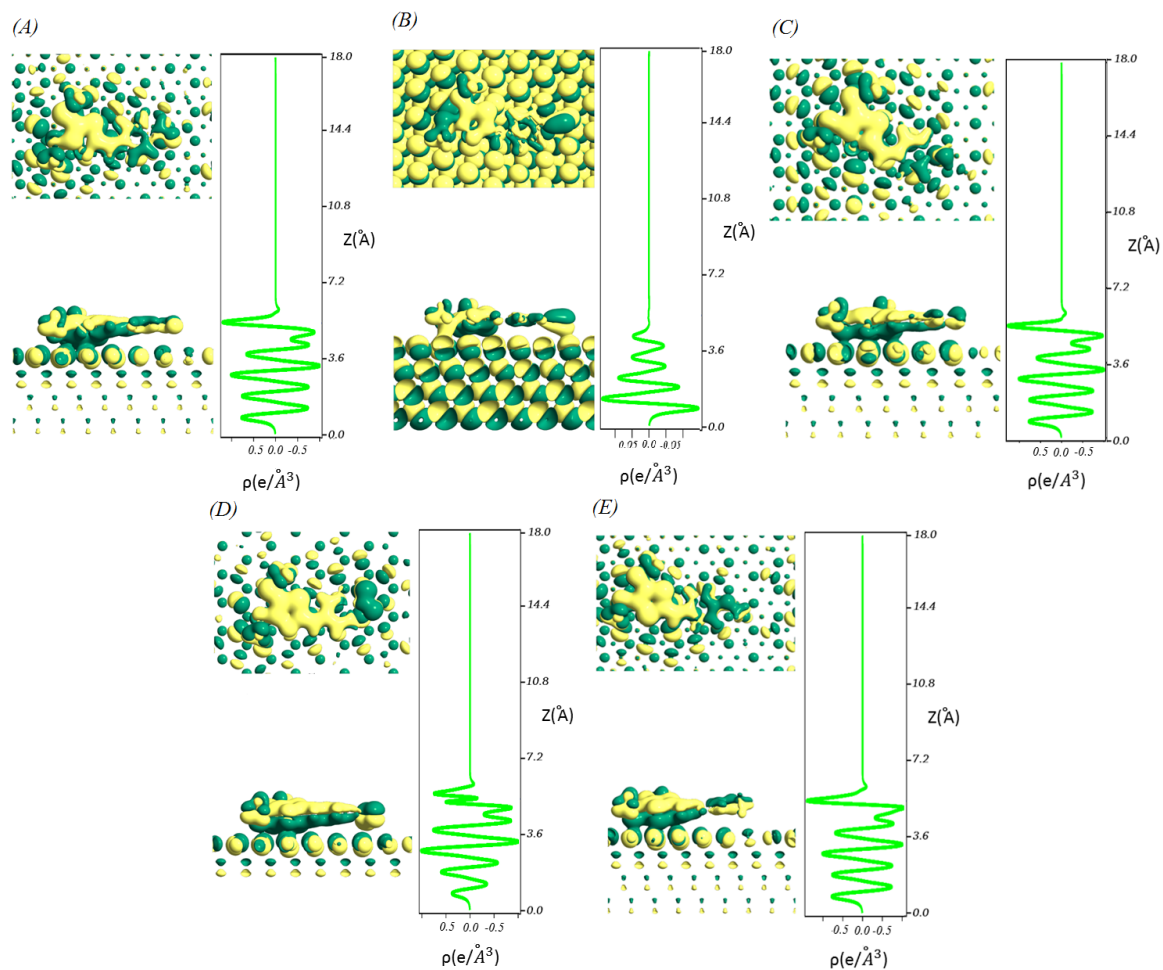


Figure 3.10: Iso-surfaces of difference charge distribution over adsorbent and surface at top and side views with considering vdW interactions for (A) CHO (B) CN (C) NH<sub>2</sub> (D) NO<sub>2</sub> (E) OCH<sub>3</sub> substituents. The negative area (green) associated with gaining electrons and the positive area (yellow) indicates the production of holes. The plot of charge distribution versus distance in the z-axis can be seen on the right side of each type of calculations which is aligned with the side view of the iso-surfaces.

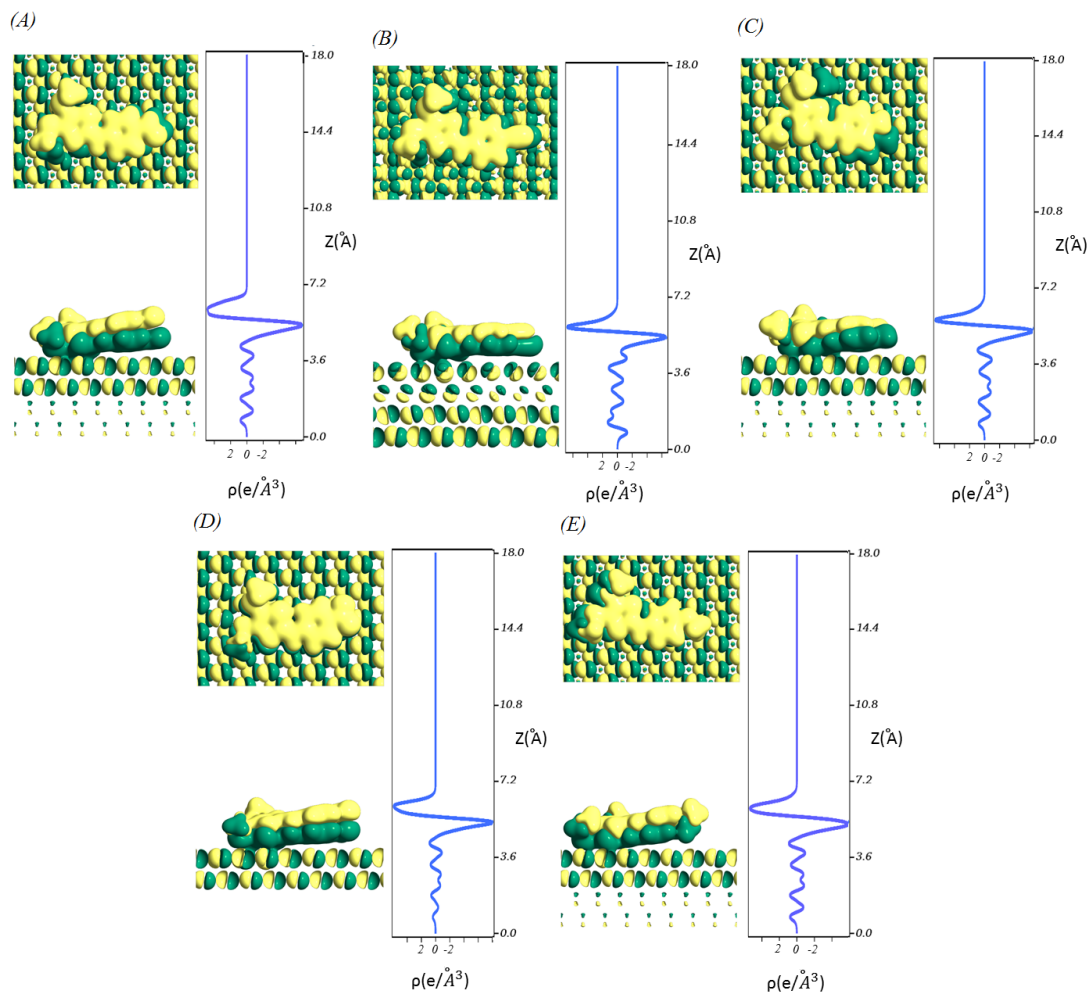


Figure 3.11: Iso-surfaces of difference charge distribution over adsorbent and surface at top and side views without considering vdW interactions for (A) CHO (B) CN (C) NH<sub>2</sub> (D) NO<sub>2</sub> (E) OCH<sub>3</sub> substituents. Negative area (green) shows the gaining of electrons and positive area (yellow) indicate the production of holes. The plot of charge distribution versus distance in the z-axis can be seen on the right side of each type of calculations which is aligned with the side view of the iso-surfaces.

properties.

## 3.6 Summary

In this chapter, DFT calculations were performed under periodic boundary conditions to simulate the electronic properties of the SAM formation of DTF derivatives on the surface of Au (111). The binding energy of the DTF **3a** at eighteen different orientations on the substrate are calculated, and the most favored orientational geometry is found to be a face-on mode through the dithiole ring. The Raman spectra of the DTF compound on an Au (111) show that benzene vibrational modes at  $C_3$  and  $C_4$  are involved in the molecule-substrate interactions, which lead to the face-on adsorption mode and results in the highest hybridization between adsorbent and substrate. The work functions of the gold surface before and after deposition of the DTF derivatives was also computed. Computational results show that the work function of the gold surface decreases upon adsorption of the DTF derivatives on the surface. As such, the work function of the gold surface can be tuned by modification of the substituent on the benzene ring of DTFs. The highest work function value to be computed was the one for the DTF with the CN substituent. Experimentally measured work functions by KPFM match very well the calculated values with and without the dispersion correction. Among all derivatives, the DTF with CN substituent bind more strongly than others. the DTF with the CHO substituent gives the weakest binding to the gold surface. Finally, calculations with vdW interaction considered show that the substituent on DTF has a significant impact on the charge redistribution between the DTF molecule and the gold substrate.

## Bibliography

- [1] Elisabeth Verwüster, Oliver T. Hofmann, David A. Egger, and Egbert Zojer. Electronic properties of biphenylthiolates on Au(111): the impact of coverage revisited. *J. Phys. Chem. C*, 119:7817–7825, 2015.
- [2] Silvio Osella, David Cornil, and Jerome Cornil. Work function modification of the (111) gold surface covered by long alkanethiol-based self-assembled monolayers. *Phys. Chem. Chem. Phys.*, 16:2866–2873, 2014.
- [3] Alexander S. Hyla, Paul Winget, Hong Li, Chad Risko, and Jean-Luc Brédas. Work function reduction by a redox-active organometallic sandwich complex. *Org. Electron.*, 37:263 – 270, 2016.
- [4] Yinhua Zhou, Canek Fuentes-Hernandez, Jaewon Shim, Jens Meyer, Anthony J. Giordano, Hong Li, Paul Winget, Theodoros Papadopoulos, Hyeunseok Cheun, Jungbae Kim, Mathieu Fenoll, Amir Dindar, Wojciech Haske, Ehsan Najafabadi, Talha M. Khan, Hossein Sojoudi, Stephen Barlow, Samuel Graham, Jean-Luc Brédas, Seth R. Marder, Antoine Kahn, and Bernard Kippelen. A universal method to produce low-work function electrodes for organic electronics. 336:327–332, 2012.
- [5] Oliver T. Hofmann, Gerold M. Rangger, and Egbert Zojer. Reducing the metal work function beyond pauli pushback: a computational investigation of tetrathiafulvalene and viologen on coinage metal surfaces. *J. Phys. Chem. C*, 112:20357–20365, 2008.
- [6] Siddharth J. Jethwa, Federico Grillo, Herbert A. Fruchtl, Grant J. Simpson, Michael-John Treanor, Renald Schaub, Stephen M. Francis, Neville V. Richardson, and R. Alan Aitken. Adsorption of a dihydro-TTF derivative on Au(111) via

- a thiolate complex bonding to gold adatoms. *Chem. Commun.*, 50:10140–10143, 2014.
- [7] Bruno Schuler, Shi-Xia Liu, Yan Geng, Silvio Decurtins, Gerhard Meyer, and Leo Gross. Contrast formation in Kelvin probe force microscopy of single  $\pi$ -conjugated molecules. *Nano Lett.*, 14:3342–3346, 2014.
- [8] Benjamin Bröker, Ralf-Peter Blum, Luca Beverina, Oliver T. Hofmann, Mauro Sassi, Riccardo Ruffo, Giorgio A. Pagani, Georg Heimel, Antje Vollmer, Johannes Frisch, Jürgen P. Rabe, Egbert Zojer, and Norbert Koch. A high molecular weight donor for electron injection interlayers on metal electrodes. *Chem. Phys. Chem.*, 10:2947–2954, 2009.
- [9] Patrizia Borghetti, Afaf El-Sayed, Elizabeth Goiri, Celia Rogero, Jorge Lobo-Checa, Luca Floreano, Jose Enrique Ortega, and Dimas G. de Oteyza. Spectroscopic fingerprints of work-function-controlled phthalocyanine charging on metal surfaces. *ACS Nano*, 8:12786–12795, 2014.
- [10] Luiza Buimaga-Iarinca and Cristian Morari. Adsorption of small aromatic molecules on gold: a DFT localized basis set study including van der Waals effects. *Theor. Chem. Acc.*, 133:1502, 2014.
- [11] Axel D. Becke. A new mixing of Hartree-Fock and local density-functional theories. *J. Chem. Phys.*, 98:1372–1377, 1993.
- [12] M. J. Frisch, G. W. Trucks, H. B. Schlegel, G. E. Scuseria, M. A. Robb, J. R. Cheeseman, G. Scalmani, V. Barone, B. Mennucci, G. A. Petersson, H. Nakatsuji, M. Caricato, X. Li, H. P. Hratchian, A. F. Izmaylov, J. Bloino, G. Zheng, J. L. Sonnenberg, M. Hada, M. Ehara, K. Toyota, R. Fukuda, J. Hasegawa, M. Ishida, T. Nakajima, Y. Honda, O. Kitao, H. Nakai, T. Vreven, J. A. Montgomery, Jr.,

- J. E. Peralta, F. Ogliaro, M. Bearpark, J. J. Heyd, E. Brothers, K. N. Kudin, V. N. Staroverov, R. Kobayashi, J. Normand, K. Raghavachari, A. Rendell, J. C. Burant, S. S. Iyengar, J. Tomasi, M. Cossi, N. Rega, J. M. Millam, M. Klene, J. E. Knox, J. B. Cross, V. Bakken, C. Adamo, J. Jaramillo, R. Gomperts, R. E. Stratmann, O. Yazyev, A. J. Austin, R. Cammi, C. Pomelli, J. W. Ochterski, R. L. Martin, K. Morokuma, V. G. Zakrzewski, G. A. Voth, P. Salvador, J. J. Dannenberg, S. Dapprich, A. D. Daniels, ?. Farkas, J. B. Foresman, J. V. Ortiz, J. Cioslowski, and D. J. Fox. Gaussian 09 Revision D.01. Gaussian Inc. Wallingford CT 2009.
- [13] Roy Dennington, Todd Keith, and John Millam. GaussView Version 5. Semichem Inc. Shawnee Mission KS 2009.
- [14] Pedro O. Bedolla, Gregor Feldbauer, Michael Wolloch, Stefan J. Eder, Nicole Dörr, Peter Mohn, Josef Redinger, and András Vernes. Effects of van der Waals interactions in the adsorption of isooctane and ethanol on Fe(100) surfaces. *J. Phys. Chem. C*, 118:17608–17615, 2014.
- [15] Paulo V.C. Medeiros, G.K. Gueorguiev, and S. Stafström. Bonding, charge rearrangement and interface dipoles of benzene, graphene, and PAH molecules on Au(111) and Cu(111). *Carbon*, 81:620 – 628, 2015.
- [16] Yang Wang, Christian Urban, Jonathan Rodríguez-Fernández, José M. Gallego, Roberto Otero, Nazario Martín, Rodolfo Miranda, Manuel Alcamí, and Fernando Martín. Formation of self-assembled chains of tetrathiafulvalene on a Cu(100) surface. *J. Phys. Chem. A*, 115:13080–13087, 2011.
- [17] Ji ří Klimeš, David R. Bowler, and Angelos Michaelides. Van der Waals density functionals applied to solids. *Phys. Rev. B*, 83:195131, 2011.

- [18] M. Dion, H. Rydberg, E. Schröder, D. C. Langreth, and B. I. Lundqvist. Van der Waals density functional for general geometries. *Phys. Rev. Lett.*, 92:246401, 2004.
- [19] Guillermo Román-Pérez and José M. Soler. Efficient implementation of a van der Waals density functional: application to double-wall carbon nanotubes. *Phys. Rev. Lett.*, 103:096102, 2009.
- [20] Valentino R. Cooper, Yungok Ihm, and James R. Morris. Hydrogen adsorption at the graphene surface: a vdW-DF perspective. *Physics Procedia*, 34:34 – 38, 2012.
- [21] Bhaskar Chilukuri, Ursula Mazur, and K. W. Hipps. Effect of dispersion on surface interactions of cobalt(ii) octaethylporphyrin monolayer on Au(111) and HOPG(0001) substrates: a comparative first principles study. *Phys. Chem. Chem. Phys.*, 16:14096–14107, 2014.
- [22] Georg Heimel, Lorenz Romaner, Jean-Luc Brédas, and Egbert Zojer. Interface energetics and level alignment at covalent metal-molecule junctions:  $\pi$ -conjugated thiols on gold. *Phys. Rev. Lett.*, 96:196806, 2006.
- [23] M.M. Beerbom, B. Lägél, A.J. Cascio, B.V. Doran, and R. Schlaf. Direct comparison of photoemission spectroscopy and in situ Kelvin probe work function measurements on indium tin oxide films. *J. Electron. Spectrosc. Relat. Phenom.*, 152:12 – 17, 2006.
- [24] Wilhelm Melitz, Jian Shen, Sangyeob Lee, Joon Sung Lee, Andrew C. Kummel, Ravi Droopad, and Edward T. Yu. Scanning tunneling spectroscopy and Kelvin probe force microscopy investigation of Fermi energy level pinning mechanism on InAs and InGaAs clean surfaces. *J. Appl. Phys.*, 108, 2010.

- [25] Yunfei Wang and Yuming Zhao. Carboxylated dithiafulvenes and tetrathiafulvalene vinylogues: synthesis, electronic properties, and complexation with zinc ions. *Beilstein J. Org. Chem.*, 11:957–965, 2015.
- [26] Scott Handy. *Applications of ionic liquids in science and technology*. InTech, 2011.
- [27] Evangelina Pensa, Emiliano Cortés, Gastón Corthey, Pilar Carro, Carolina Vericat, Mariano H. Fonticelli, Guillermo Benítez, Aldo A. Rubert, and Roberto C. Salvarezza. The chemistry of the sulfur–gold interface: in search of a unified model. *Acc. Chem. Res.*, 45:1183–1192, 2012.
- [28] W.M.H. Sachtler, G.J.H. Dorgelo, and A.A. Holscher. The work function of gold. *Surf. Sci.*, 5:221 – 229, 1966.
- [29] Yingjie Zhang, Olivier Pluchery, Louis Caillard, Anne F Lamic Humblot, Sandra Casale, Yves J. Chabal, and Miquel Salmeron. Sensing the charge state of single gold nanoparticles via work function measurements. *Nano Lett.*, 15:51–55, 2015.
- [30] Anna L. Domanski, Esha Sengupta, Karina Bley, Maria B. Untch, Stefan A. L. Weber, Katharina Landfester, Clemens K. Weiss, Hans-Jürgen Butt, and Rüdiger Berger. Kelvin probe force microscopy in nonpolar liquids. *Langmuir*, 28:13892–13899, 2012.
- [31] H. L. Skriver and N. M. Rosengaard. Surface energy and work function of elemental metals. *Phys. Rev. B*, 46:7157–7168, 1992.

# Chapter 4

## Reduction of Au (III) into Au Nanoparticles by Dithiafulvenes in Aqueous Media

### 4.1 Background

UV-Vis spectroscopy is a useful technique for detecting the presence of various metal nanoparticles. Absorption of visible light by gold nanoparticles (AuNPs) is dependent on the size of the particles. Nanoparticles usually absorb light in the range of 480 to 560 nm, which allows the growth of particles produced in solution to be monitored. In general, AuNPs can be synthesized by mixing a reducing agent with  $\text{HAuCl}_4$  in a biphasic solution under certain conditions. Tuneable parameters for the reductive synthesis of AuNPs include the reagent concentrations, stirring rate, and more importantly the reaction temperature. The morphological properties of the produced AuNPs, such as shape and size, are dependent on the applied conditions. Reduction of  $\text{HAuCl}_4$  should be carried out in an appropriately chosen solvent and with a suitable

reductant to achieve size-control over the resulting nanoparticles.

The formation of AuNPs in solution can be characterized by UV-Vis spectroscopic analysis; in particular, the absorption band at 520–620 nm is characteristic of AuNPs. The solution of AuNPs absorbs the green light to give orange to red color depending on the average size of the nanoparticles [1]. The wavelength of the absorption peak can be useful for estimating the mean size of the AuNPs suspended in solution. Aggregation and growth of AuNPs in size make the absorption band shift to longer wavelength (620 nm), turning the color of the AuNP solution into blue [2]. Mechanistically, the formation of AuNPs involves nucleation and growth steps. Addition of end-capping agents with a high affinity for gold atoms (e.g., alkylthiols) can stabilize AuNPs by forming a protecting layer to prevent AuNPs from further growth and agglomeration.

In this work, the reductive nature of DTF is taken advantage of for the synthesis of AuNPs. Apart from being an effective reductant, DTF is also expected to act as a stabilizing ligand binding with AuNPs due to the presence of sulfur atoms. This would help prevent the AuNPs from agglomeration and keep the average size distribution controlled under well-defined conditions, such as temperature, pH, and solvent polarity. The following sections discuss on the experimental investigations of AuNPs formation by treating Au(III) with DTF molecules in aqueous media. Computational studies were also carried out in the mean time to gain deeper understanding on the DTF–AuNP interactions at the molecular level.

## 4.2 Computational Methods

Density functional theory (DFT) calculations were performed using the Becke’s three parameters exact exchange-function (B3) along with gradient-corrected correlation function of Lee-Yang-Parr (LYP) and Perdew and Wang (PW91) that can predict

the best results for molecular geometry and vibrational frequencies of aromatic compounds [3]. The 6-311+G(d,p) basis set was used to obtain the complete geometry optimization and normal-mode analysis on isolated molecules in the ground state. The values of all calculated vibrational modes indicate that the optimized molecular structures are the ground state rather than transition state structures. The polarizable continuum model (PCM) was adopted to include the effect of solvent [4]. Excitation energies and excited-state properties were calculated by time-dependent density functional theory (TD-DFT) using the same functional and basis set as those used for geometry optimization [5]. The structure of the gold group and compound-complex were optimized using the B3LYP method with 6-31+G and LANL2DZ mixed basis sets. All calculations were carried out using the Gaussian 09 software package and the results were visualized by the GaussView 5.0.8 program [6, 7].

### 4.3 Experimental Details

DTF **3a** and **4a**, as shown in Figure 4.1, were synthesized through the procedures reported in Chapter 2 [8]. In these two compounds, the *para* position of the benzene ring is substituted with carboxyl (DTF **3a**) and methyl carboxylate (DTF **4a**) respectively, and they were both used for experimental investigations and comparative studies in this chapter.

UV-Vis absorption spectra were recorded in solution or on solid thin films using a Cary 6000i UV-Vis-NIR spectrophotometer. MFP-3D (Asylum Research) atomic force microscope (AFM) was utilized to study the morphological properties of the thin film surface with a silicon tip (NSC35/AIBS, MikroMasch) operated in the tapping mode (scan rate 1 Hz). The nanostructures were also characterized by SEM. Raman spectroscopic measurements of the thin film of **3a** were conducted on a Renishaw

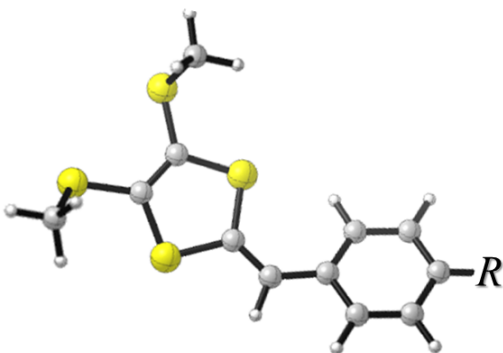


Figure 4.1: The structure of the DTF oligomer with R substituent at the *para* position of the benzene ring (yellow color represents sulfur atom). Two different substituents of carboxyl (DTF **3a**) and carboxymethyl (DTF **4a**) were used for future comparison studies. Dimerization occurs under oxidative condition by losing hydrogen through a bridging carbon atom between the five-membered ring and the benzene (Chapter 2 (Figure 2.1)).

inVia instruments with excitation at 830 and 630 nm. Thin films of the sample were prepared by drop casting a solution in methanol on the surfaces of mica and glass. Acetone with a trace amount of water was also used as the redox medium. The average size distribution of the AuNPs is measured using a Malvern Zetasizer Nano ZS (dynamic light scattering methods). Deconvolution of the UV-Vis absorption bands was done using the Igor Pro 6.37 software package.

## 4.4 Functionalized AuNPs Nucleation and Growth

AuNPs encapsulated with DTFs were synthesized through the reduction of  $\text{HAuCl}_4$  with DTF **3a** in solvents. The procedure began with dissolving 1 mg of **4a** in methanol and an addition of 1 mL of 1 M  $\text{HAuCl}_4$ . The mixture was then sonicated for half an hour to end up with an orange color solution as shown in Figure 4.2. As can be seen in Figure 4.2, AuNPs were formed in the solution and UV-Vis spectra were taken before and after addition of  $\text{HAuCl}_4$ . The characteristic peak of AuNPs at 525 nm could be observed after sonication of the solution for one hour. The peak

at 372 nm disappeared, indicating that free DTF **4a** molecules were all consumed by the Au(III)/DTF redox reaction [9]. The average size of 30–50 nm is predicted for the orange solution of AuNPs with the maximum absorption of 530 nm shown in Figure 4.2 [2].

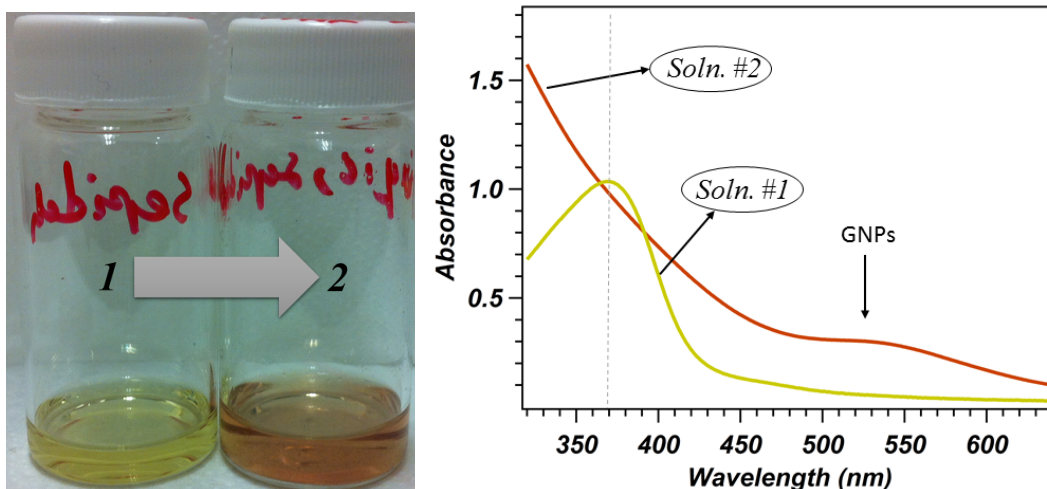


Figure 4.2: Left) The solution of **4a** in methanol before (vial number one with yellow color) and after (vial number two with orange color) mixing it with the  $\text{HAuCl}_4$  and sonication for an hour. Right) The UV-Vis spectra of solution number one and two as labeled. AuNPs peak at peak at 525 nm appeared after addition of the  $\text{HAuCl}_4$ .

The AFM images of the synthesized nanoparticles on a mica surface were taken in the tapping mode. The results are shown in Figure 4.4. As can be seen, flower-shaped features are clearly observable. The indicated morphology is also confirmed by the SEM image of carbon coated glass slides that are shown in Figure 4.3. SEM images were not taken from a freshly prepared solution. Results indicate that the observed features at the AFM images are not an artifact or impact of solvent evaporation on the mica surface. The spherical feature with the approximate size of thousands of nm has also appeared in the SEM image.

The mean size of AuNPs was measured to be 50 nm in the solution of methanol at pH 10 using the zeta-sizer analyzer. The mean size of particles dramatically increases to 800 nm at pH 6. Therefore, an acidic environment is thermodynamically more

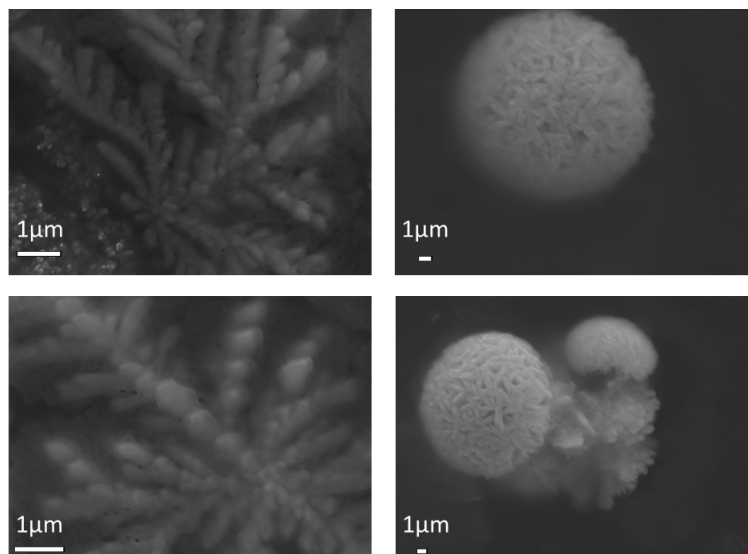


Figure 4.3: SEM images of the AuNPs that are freshly prepared through redox reaction of **3a** and gold acid. The film of solution on the glass slide was then coated with a layer of carbon for imaging.

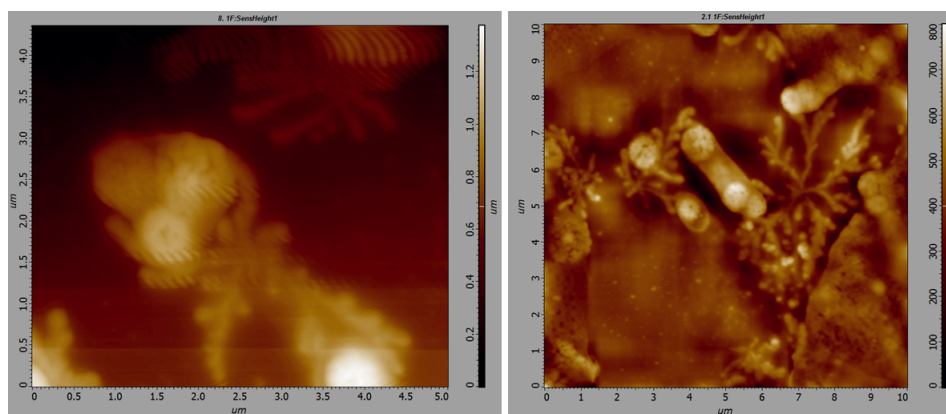


Figure 4.4: AFM height image of the deposited AuNPs on freshly cleaved mica at two scan areas. Left) the AFM image of the surface at  $10 \times 10$  nm scan area. Right) The focused AFM image of the flower shape feature in  $5 \times 5$  nm scan area.

avored for the oxidation reaction of **3a** in which protons facilitate the oxidation reaction.

Ethanol, water, THF, and acetone were also tested out to compare the reaction rates of AuNP formation. The color change occurred at a much slower rate in acetone, and a trace amount of water was necessary for the formation of gold nanoparticles. Therefore, acetone and trace water were used in the experiments for the mechanistic studies in the second part of the chapter. Solutions of **3a** and **4a** were prepared by adding a 1 mg of DTF compound in 10 mL of acetone and a trace amount of water. HAuCl<sub>4</sub> was prepared by solvation of 1 mg of AuCl<sub>3</sub> in 10 mL of acetone. 2 mL of preheated HAuCl<sub>4</sub> was mixed with 1 mL of the respective solutions of **5a** and **5b** and then heated to 40 °C and stirred for half an hour. AuNPs were gradually formed by reduction of Au<sup>3+</sup> to Au<sup>0</sup> through oxidation of dithiafulvene molecules, as evidenced by the appearance of a UV-Vis peak at 520 nm. The yellow color of the solution turned into red orange, indicating the presence of gold nanoparticles.

As can be seen in Figure 4.5A, the yellow color of **3a** solution turned green after half an hour of stirring with HAuCl<sub>4</sub> at 40 °C (oil bath). The UV-Vis spectrum of the green solution show a broad absorption band at 670–720 nm. The green color gradually turned into orange throughout the next 24 hours, which eventually gave the characteristic absorption at 520 nm. Eye-detectable fine dispersed dark particles precipitated out of the solution after two weeks due to the excessive growth of particles. There was a broad range of functionalized particle sizes in the solution based on the multiple peaks that appeared between 520 to 700 nm.

Figure 4.5B shows the solution of **4a** prepared by the addition of 1 mg of DTF compound in 10 mL of acetone and a trace amount of water (yellow solution on the left). The solution turned into blue after one hour of mixing with 1 mL of HAuCl<sub>4</sub>, stirring and heating at 40 °C in an oil bath. The color of the solution turned into

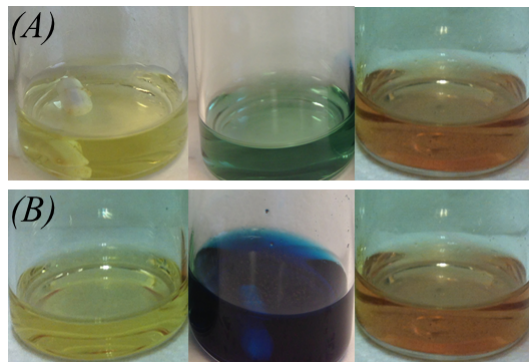


Figure 4.5: (A) The solution of **3a** in acetone and a trace of water (yellow solution). The color of the solution turns green by addition of preheated  $\text{HAuCl}_4$  to 40 °C and gradually turns orange by heating and stirring. (B) The solution of **4a** in acetone and a trace of water (yellow solution). The color of the solution turns blue by addition of preheated  $\text{HAuCl}_4$  to 40 °C and gradually turns orange by heating and stirring.

orange over the next 24 hours and black precipitates formed after two weeks.

#### 4.4.1 UV-Vis Analysis of Functionalized AuNPs

UV-Vis spectra of **4a** in methanol before and after the addition of  $\text{HAuCl}_4$  are shown in Figure 4.6 and the simulated UV-Vis spectra of the DTF compound in the gas phase in both neutral and oxidized states are shown in Figure 4.7. Figures 4.6 and 4.7 are generated by cubic fitting (as shown on the top) of the measured spectra and peaks are deconvoluted to the peaks involved in each absorption band (as shown on the bottom). The original spectra are reported in Appendix E. Comparison of the measured and calculated UV-Vis spectra reveals the following results:

1) Figure 4.6 on top: Experimental peaks at 216.22, 285.73, 420.73 and 487 nm correspond to the simulated peaks at 206.52, 239, 275.59 and 381 nm (Figure 4.7 (A)) for **4a** at neutral form (the peak assignments are reported in Appendixes E.2 and E.3). The solvent impact causes the differences between simulated and experimental peaks resulting in the bands appearing at higher wavelengths. The differences can arise from the simulation of the single molecule in the gas phase without considering

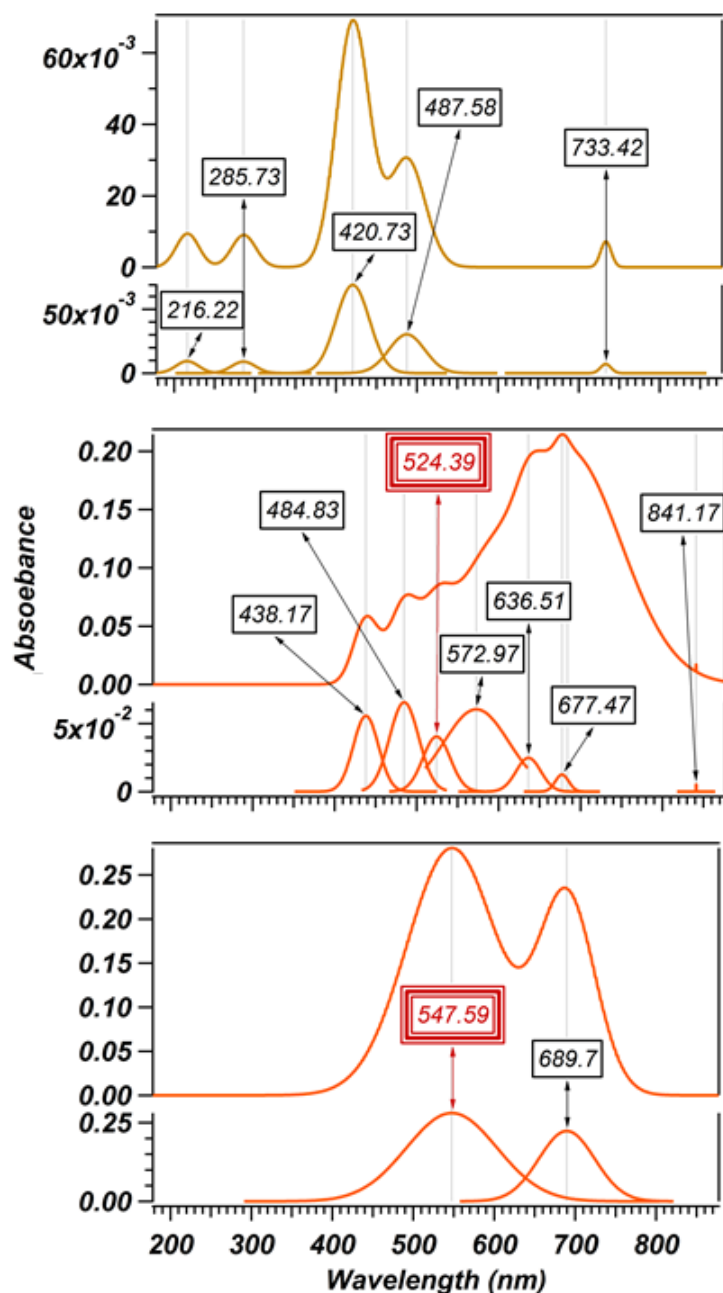


Figure 4.6: (Top) UV-Vis spectrum of **4a**; the peak at 420 nm refers to the maximum absorption of **4a** in neutral form, which is shown in simulated UV-Vis spectrum of **4a** in neutral form (Figure 4.7 (A)). (Middle) UV-Vis spectrum of **4a** after half an hour addition of H<sub>2</sub>AuCl<sub>4</sub> and sonication; the peak at 524 nm corresponds to the AuNPs absorbance. (Bottom) UV-Vis spectrum of **4a** after twenty four hours following addition of the H<sub>2</sub>AuCl<sub>4</sub>; the AuNPs corresponding peak is shifted to the higher wavelengths at 547 nm with relatively higher absorbance.

the surrounding AuNPs that are grafted to DTF molecules in the presence of the solvent.

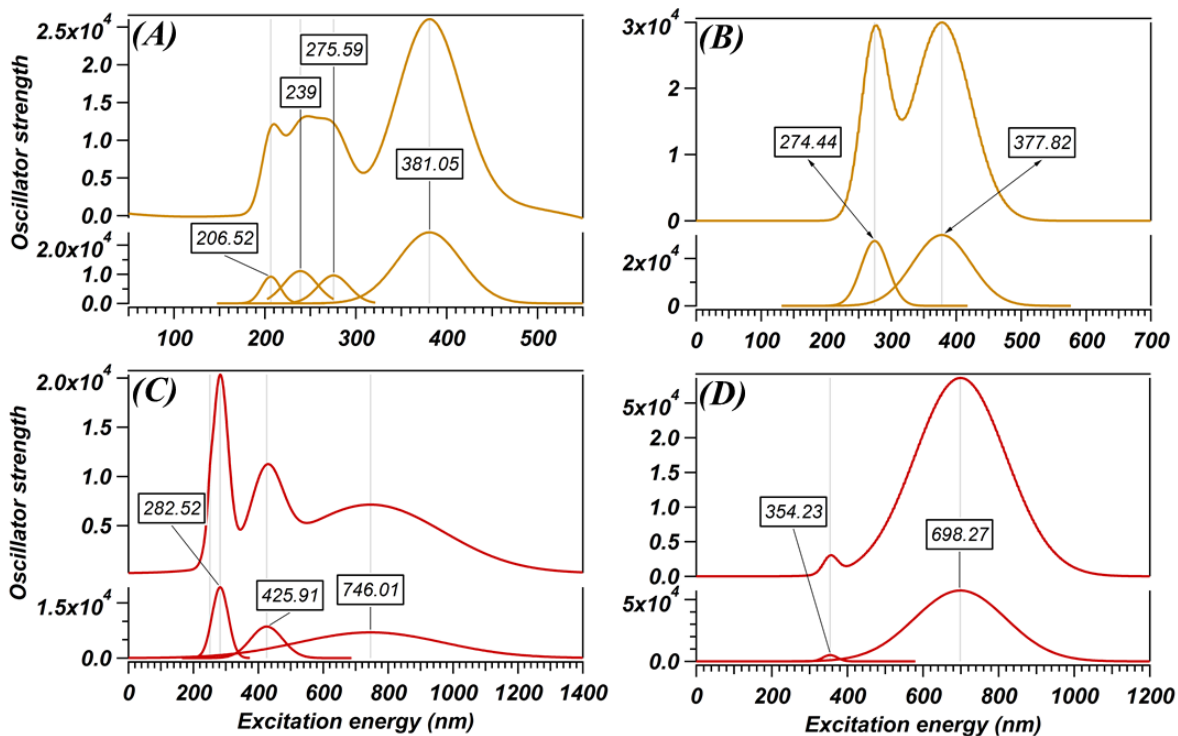


Figure 4.7: (A) and (C) are simulated UV-Vis spectra of **4a** in neutral and oxidized forms, which are obtained with time-dependent B3PW91/6-311G(d,p) level of theory and basis set and 40 number of states. Simulated UV-Vis spectrum indicate that there is no band between 500–600 nm before, and after oxidation of **4a**. Therefore the band at 524 nm right after addition of  $\text{HAuCl}_4$  refers to the AuNPs absorbance, which shifts for 23 nm to the higher wavelength after twenty-four hours (Figure 4.6). (B) and (D) are simulated UV-Vis spectra of dimerized **4a** in neutral and oxidized forms, which are computed with time-dependent B3PW91/6-31+G(D,P) level of theory and basis set and the number of states is 40.

2) Figure 4.6 middle: AuNPs characteristic band at 524 nm appears after an hour of mixing and sonication with  $\text{HAuCl}_4$ . This band cannot be referred to any peak in the simulated spectrum of the cationic form. As mentioned in the introduction, absorption of AuNPs at 520 nm indicates the average size distribution of approximately 30 nm [10].

3) Figure 4.6 bottom: AuNPs characteristic peak shifts to the higher wavelength at

547 nm, which indicates that the average size of the particles has grown substantially. Absorption of AuNPs at 550 nm indicate the average size distribution of approximately 90 nm [10]. Hence, the size of synthesized nanoparticles can be controlled by the time of sonication and temperature. Furthermore, the absorbance of the AuNPs peak considerably increased after twenty-four hours.

4) Figure 4.6 bottom: As mentioned in Chapter 2, the DTF oxidative dimerization reaction occurs in an oxidative environment. Accordingly the peaks at 689 and 677 nm (Figure 4.6 middle) correspond to a peak appears at 698 nm in the simulated spectrum of dimerized compound in the cationic form (Figure 4.7D).

AuNPs can also be synthesized by **3a** in which a carboxyl group is substituted at the *para* position of the benzene ring instead of methyl carboxylate group (**4a**). The substitution of a carboxyl group results in a faster rate of nucleation and growth of functionalized AuNPs, likely because the carboxyl group releases hydrogen ion and makes the solution more acidic than the solution of **4a**. The presence of hydrogen ions accelerates the release of electrons and oxidation of the compound. The color of the solution turns into green right after addition of  $\text{HAuCl}_4$ , whereas the solution of **4a** needs to be heated and sonicated at least for half an hour to give the same results. The redox potentials of the reactants involved are discussed in Section 4.6.1 by calculating the oxidation potentials of the molecules in the different types of solvents.

#### 4.4.2 Raman Analysis of Functionalized AuNPs

Raman spectra of **3a** in methanol before and after the addition of  $\text{HAuCl}_4$  are shown in Figure 4.8. As can be seen, the predicted peak at  $1620\text{ cm}^{-1}$  (Figure 4.8C), which is the carbon-oxygen double bond stretching of carboxyl group, does not appear in the experimental spectrum of the neutral compound (Figure 4.8A). It can be ascribed to the strong intermolecular hydrogen bonding interactions between the carboxyl groups

of the DTF molecules, which prohibits the carbon-oxygen bond from stretching as readily as in a free single molecule in the gas phase [11]. The corresponding peak can be clearly seen in the Raman spectrum of **4a** in the neutral form (Figure 4.9) in which there is no hydrogen bonding between carboxylate ester groups.

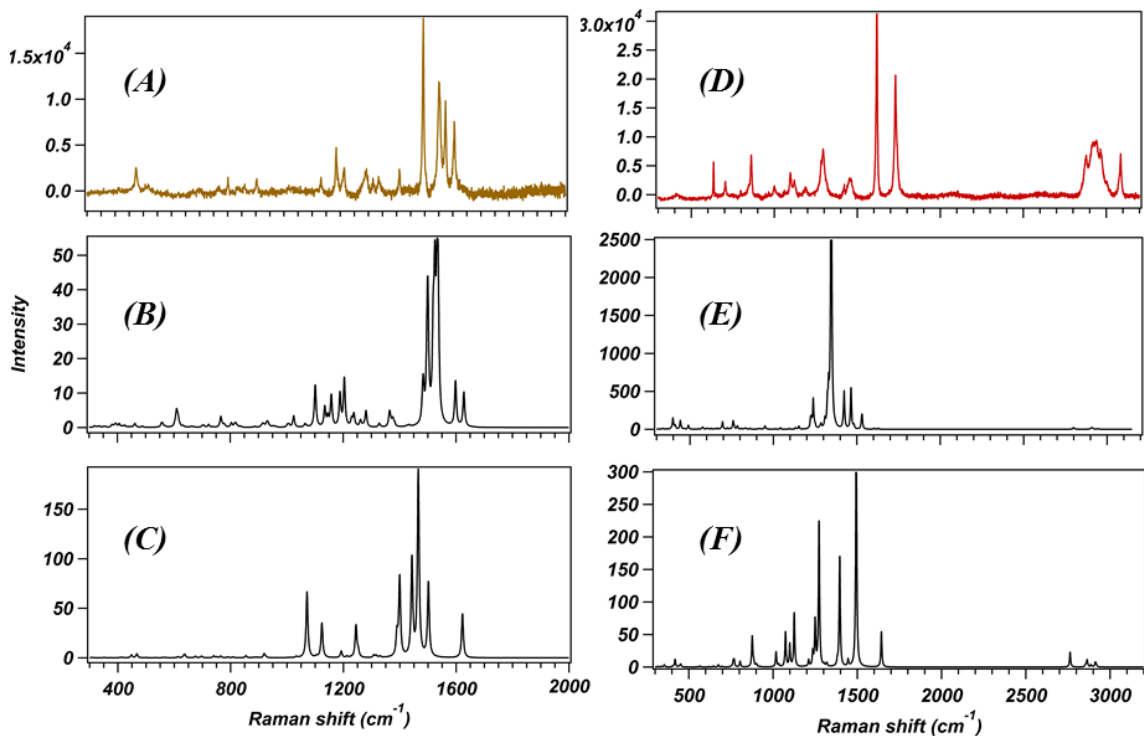


Figure 4.8: (A) and (D) The experimental Raman spectra of **3a** in methanol before and after addition of  $\text{HAuCl}_4$ , respectively. Red spectrum (D) is taken from the solution of **3a** after twenty-four hours of mixing it with  $\text{HAuCl}_4$  in which the color was turned orange. (B) and (E) Simulated Raman spectra of dimerized **3a** in neutral and oxidized states, respectively. (C) and (F) Simulated Raman spectra of **3a** in neutral and oxidized states, respectively.

The experimental Raman spectra of **3a** (Figure 4.8D) after mixing it with  $\text{HAuCl}_4$  does not match very well the simulated Raman spectra of **3a**, nor dimerized **3a** in the oxidized state. However, there is a closer similarity with simulated spectra of dimerized **3a** in the neutral form such as peaks at  $1612$  and  $1726\text{ cm}^{-1}$ , which appeared at  $1494$  and  $1536\text{ cm}^{-1}$ , respectively. The first peak is C=C bond stretching of the benzene rings and the second band is due to the C=C bond stretching as they are

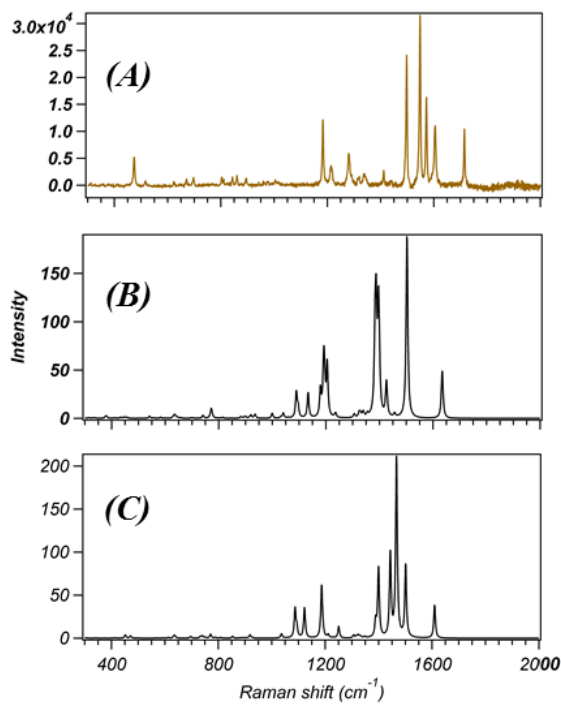


Figure 4.9: (A) The experimental Raman spectrum of **4a** in methanol. (B) Simulated Raman spectra of dimerized **4a** in neutral form. (C) Simulated Raman spectrum of **4a** in neutral form at B3PW91/6-31+G(G,P) level of theory and basis set. C=O bond stretching band appears in both computed and experimental spectrum of **4a** and dimerized **4a** at 1800 and 1620 cm<sup>-1</sup>, respectively. All simulations performed at B3PW91/6-31+G(D,P) level of theory and basis set.

shown in Figure 4.10.

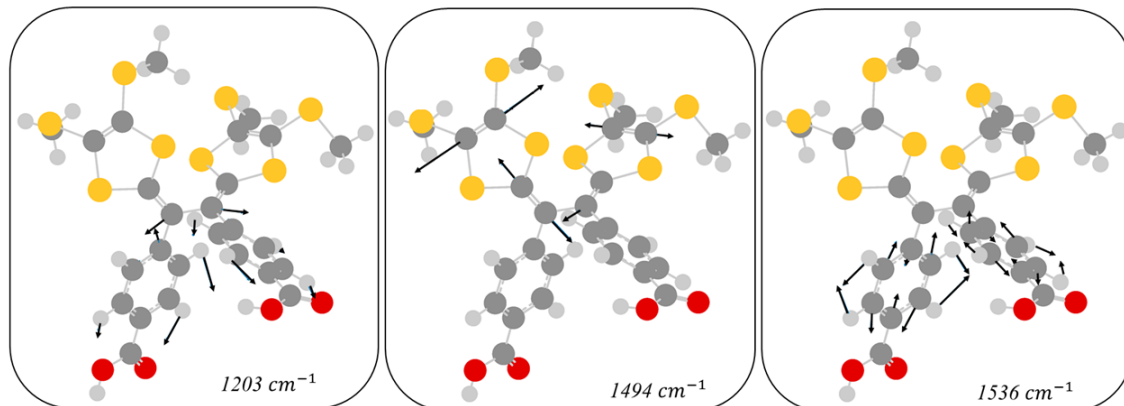


Figure 4.10: Vibrational modes of three enhanced peaks at 1289 and 1612, 1726  $\text{cm}^{-1}$  observed in the Raman spectra of **3a** computed with B3PW91/6-31+G(D,P) level of theory and basis set.

As can be seen in Figure 4.10, vibrational peaks due to the benzene ring and C=C bonds are dramatically enhanced in the presence of AuNPs. Therefore, it is reasonable to assume that AuNPs interact with dimerized **3a** through  $\pi$ -Au interactions. Furthermore, the experimentally observed peaks at 2875 to 3084  $\text{cm}^{-1}$  show enhancement, which are associated with the C-H stretching.

## 4.5 Time-dependent UV-Vis Spectral Analysis

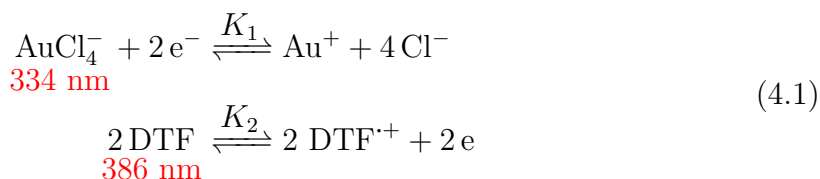
As mentioned in Section 4.3, acetone and trace water were utilized as the solvent for investigating the redox mechanisms at a much slower rate in the aqueous media. The solution of DTF compound and  $\text{HAuCl}_4$  were prepared through the following method, in which 2 mL of the  $\text{HAuCl}_4$  was heated at 40 °C with stirring for 30 minutes. Then 1 mL of the solution of the DTF compound was added to the stirring  $\text{HAuCl}_4$ , and UV-Vis spectra were taken at different time intervals to monitor the process. Figure 4.11 shows the time-dependent UV-Vis spectra of **4a** recorded at various time intervals within 24 hours. The results are summarized as follows:

1) The peak at 334 nm is assigned to the  $\text{HAuCl}_4$  absorption that appears right after the addition of  $\text{HAuCl}_4$  to the solution, which gradually decreases throughout the reaction processes [12].

2) Peak assignments for 386 and 684 nm are obtained by comparison of simulated UV-Vis peaks (Figure 4.7 (A) and (D)) and experimentally observed ones, which are associated with the DTF monomer in the neutral form and  $\text{TTFV}^{2+}$  dimer in the oxidized state. The UV-Vis spectra of **4a** in acetone and a trace amount of water show only one absorption band at 386 nm (Figure 4.11 (Left) yellow spectrum). The broad peak at 684 nm appears after addition of  $\text{HAuCl}_4$ , which gradually increases in intensity to reach the maximum absorption after 30 minutes of mixing (Figure 4.11 (Right)). Then the  $\text{TTFV}^{2+}$  peak at 684 nm is seen to decrease and eventually disappear after 24 hours. The corresponding peak completely vanishes after the appearance of the characteristic peak of AuNPs at 510 nm (Figure 4.11 (Left) red spectra) by warming the solution.

3) Comparison of the experimental and simulated spectra indicates that the peak at 684 nm corresponds to dimerized **4a** in the oxidized form, which is not yet bonded to the gold species.

4) The peak at 386 nm gradually decreases with increasing concentration of Au (III). Along with the increase is the decrease of the peak at 684 nm (Figure 4.11 (Right)), which indicates that **4a** and Au(III) are consumed by the redox (Equation 4.1) and dimerization reactions (Equation 4.2) respectively.



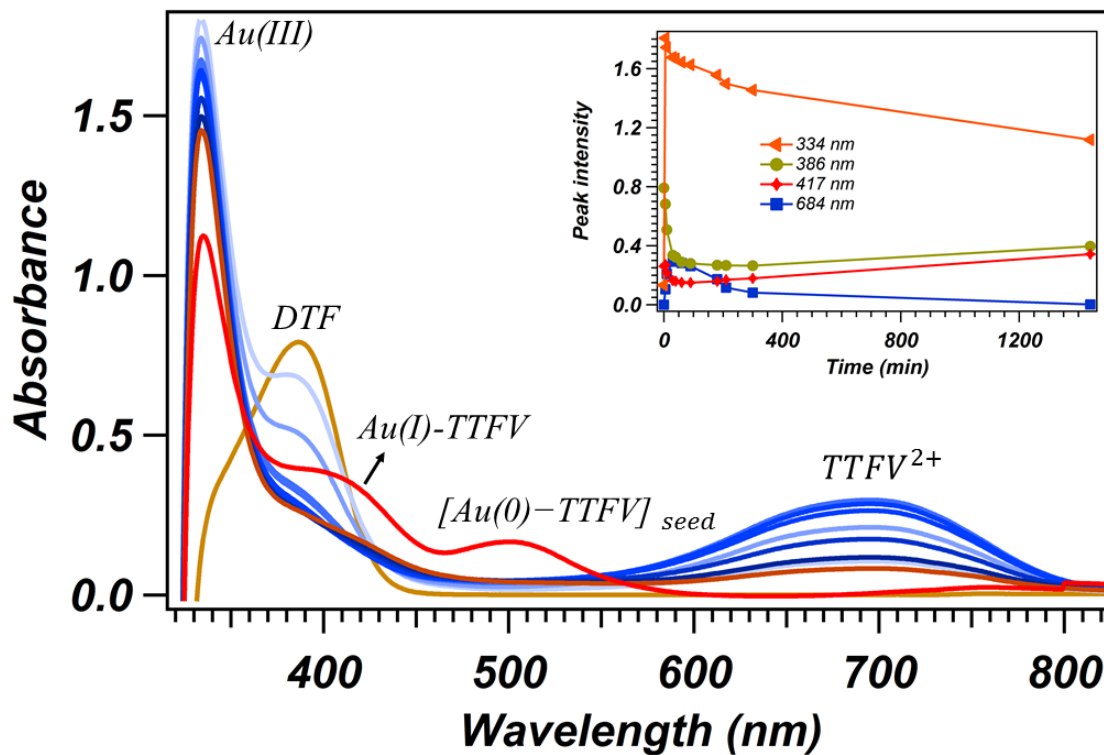
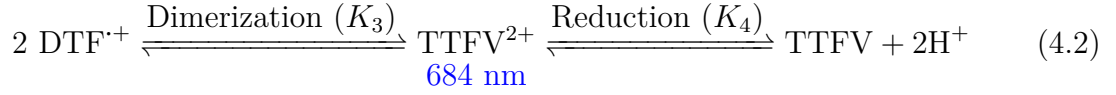


Figure 4.11: Left) Experimental time-dependent UV-Vis spectra of **4a** in acetone and a trace of water before and after addition of the pre-warmed HAuCl<sub>4</sub> at different time intervals. Red spectra are taken after warming the solution that was left in the closed cap vial overnight. Right) Peak intensity versus time are plotted for major peaks that are indicated in UV-Vis spectra.

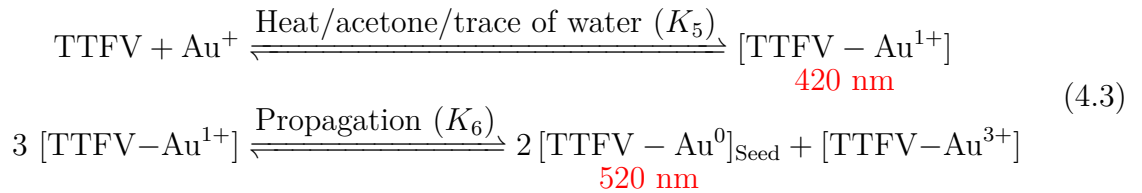


5) Dimerization occurs right after the formation of DTF in the cationic state. Therefore, there is no peak related to the DTF radical cation species. However, Au(III) substitution occurs in a faster rate than reduction in the presence of thiocyanate and thiosulfate [13].

6) Decreasing the intensity of the peak at 684 nm after 30 minutes indicates that the  $\text{TTFV}^{2+}$  species are consumed through another reaction, which is proposed to be a reduction (Equation 4.2) and coupling reaction with gold atoms (Equation 4.3).

7) The complex formed between gold atoms and TTFV molecules are then going through the propagation reaction to form the seeds of AuNPs, which contributes to the growth of the absorption peak at 520 nm.

8) AuNPs formation is a process accompanied by the absorption of heat to overcome the energy barrier and induce AuNPs seed formation at some steps. The color of the solution never turns into orange without heating the samples.



With the proposed method, AuNPs can only be obtained in acetone with a trace amount of water; therefore, the role of acetone and water should be considered in nanoparticle formation, which is still under debate and needs more investigation. It is proposed that acetone can change the solvent effect by heating and in the presence

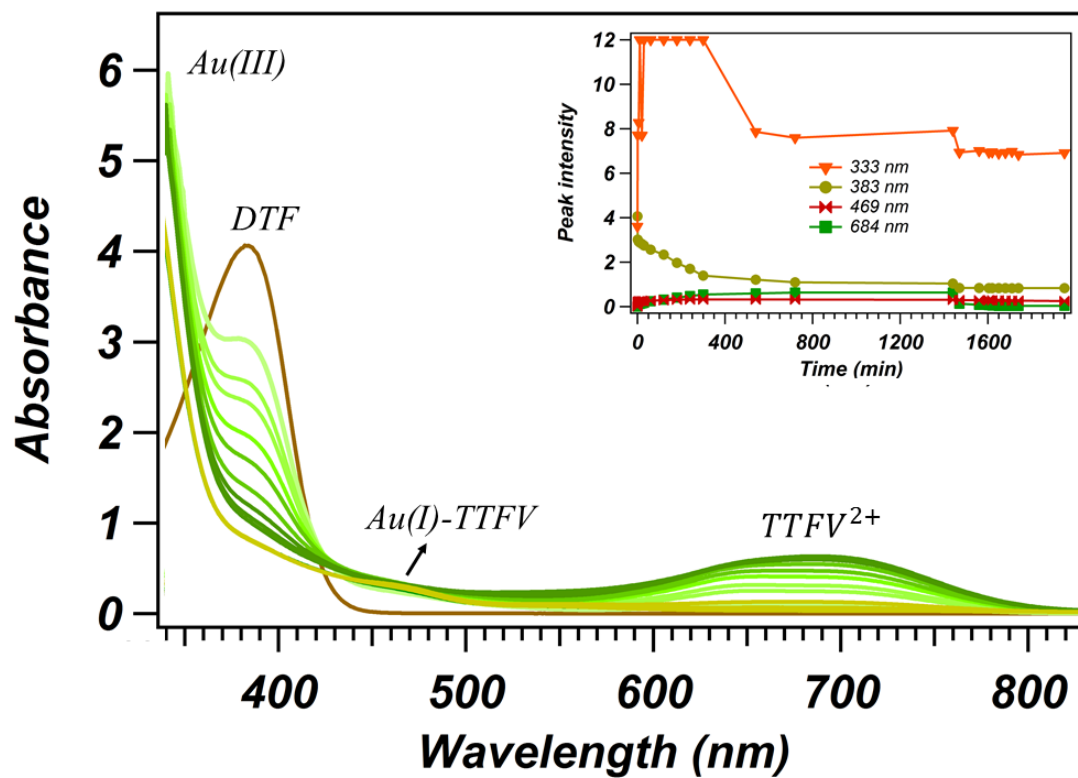


Figure 4.12: (Left) Experimental UV-Vis spectra of **3a** in acetone and a trace of water before and after addition of the pre-warmed  $\text{HAuCl}_4$  to  $40^\circ\text{C}$  throughout 32 hours. (Right) Peak intensity versus time is plotted for the assigned peaks.

of water.

The same set of experiments was conducted for **3a** and the results are plotted in Figure 4.12. As can be seen, the DTF peak at 383 nm and Au(III) absorption at 333 nm gradually decrease while TTFV<sup>2+</sup> absorption at 684 nm increases. The sample was then heated for 24 hours, after which a peak at 459 nm appeared, which corresponds to the TTFV and Au(I) complex. AuNPs did not form in the solution, and the color of the solution turned back to yellow. Hence, the TTFV-Au<sup>1+</sup> complex proved to be very stable, and the propagation reaction did not occur in the solution.

Based on the observations, it can be concluded that the gold and dimerized **3a** complex is stable and heating the sample at 40 °C does not supply enough driving force to form the seeds of AuNPs. Therefore, the substituent plays a major role in stabilizing the complex with gold. Peak intensity versus time for all the main peaks shows a small bump right after heating the sample (Figure 4.12 (Right)).

The same set of experiments was repeated for three more samples that were first left for 24 hours and then be heated to 40 °C. Finally, UV-Vis spectra of the sample were taken over a period of 24 hours (Appendix E). All spectra show that the DTF peak has shifted to higher wavelengths and the color of the solution turned back yellow, which is a sign of dimerized DTF in the neutral state that is bonded to the gold atoms.

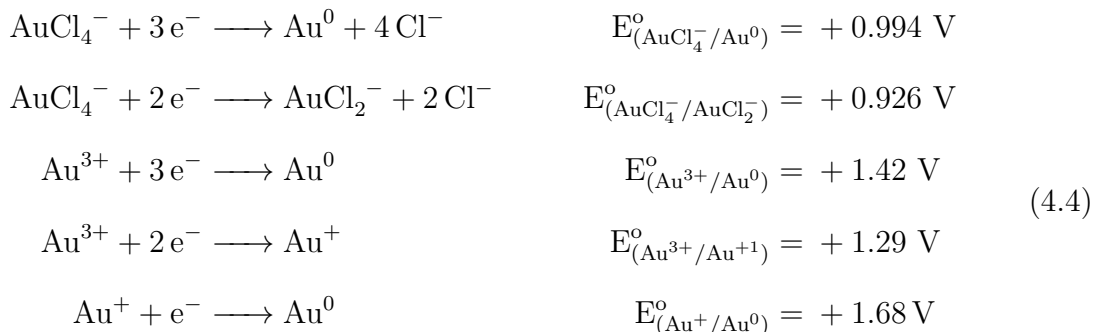
## 4.6 Effective Parameters on Reaction

As mentioned earlier, **4a** in acetone and a trace amount of water were used for UV-Vis studies due to a slower rate of reaction that allows us to track the reaction mechanism more accurately. The redox reaction proceeded readily without the need of heating or light irradiation. **3a/4a** can be easily oxidized in the presence of Au<sup>3+</sup>, which is

reduced to  $\text{Au}^+$ . Furthermore, the AuNPs peak did not appear in the solution of **3a**, and acetone and the color of the solution turned from back to yellow. So for these reasons, the solvent effects on the redox reaction was found essential to the AuNPs formation and the rate of reaction. On the other hand, the substituent on the benzene ring was found to be very critical in AuNPs formation and play a major role in stabilizing the [Au(I)-DTF] complex. So for the above-mentioned reason, the study of effective parameters on redox reaction is crucial for further understanding of the AuNP formation.

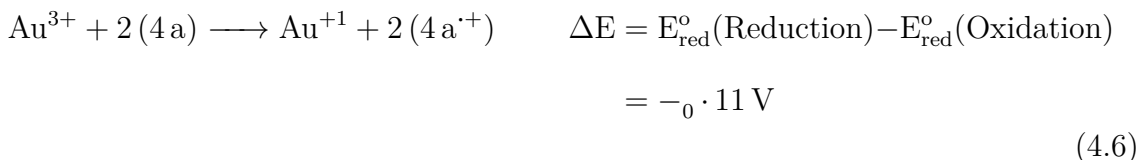
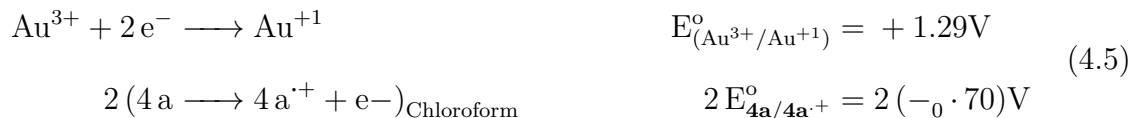
#### 4.6.1 Effects of Solvents Polarity

It is necessary to mention that  $\text{HAuCl}_4$  undergoes stepwise hydrolysis depending on the pH of the medium.  $\text{AuCl}_2\text{OH}_2$  at pH 4.5 is the main species in aqueous media [14]. Equation 4.4 shows the reduction potentials of  $\text{AuCl}_4^-$  and  $\text{Au}^{3+}$  at different oxidation states that are reported in the literature (values obtained in 0.4 M NaCl to maintain the concentration of  $\text{Cl}^-$  high enough to prevent hydrolysis of  $\text{HAuCl}_4$ ) [15].



The oxidation potentials of **3a** and **4a** in methanol are computed to be +5.16 and +5.13 V at the B3PW91/6-31+G(d,p) level of theory and basis set. Therefore, oxidation potentials are calculated to be +0.50 and +0.47 V respectively in reference

to a Ag/AgCl electrode ( $E^\circ(\text{Ag}/\text{Ag}^+) = +4.66 \text{ V}$ ) [16]. Equation 4.5 displays the electrochemical half reactions of gold and DTF [17], and Equation 4.6 shows the electrochemical redox reaction and total potential.



Oxidation potentials of compounds and  $\Delta E$  of redox reactions are calculated in seven different solvents and shown in Table 4.1. Positive values indicate that the redox reaction proceeds spontaneously and zero represents the reaction at equilibrium. Oxidation potentials decrease upon increasing the solvent polarity due to better stabilization of the ionic product of oxidation by the solvent. In the table, solvents are ordered from top to bottom in terms of increasing polarity. As can be seen, solvent polarity can change the absolute value of  $\Delta E_{redox}$  up to 0.5 V. Moreover, **3a** shows persistently a higher oxidation potential than **4a** in all different types of solvents. It is obvious that high solvent polarity can facilitate oxidation reaction.

## 4.7 Computational Analysis of 4a-Au<sub>n</sub> Complex

A number of different adsorption sites was studied in Chapter 3 such as adsorption through dithiole, benzene and carboxylic ester groups. The results show that **4a** tends to bind to the surface in a way that the benzene, dithiole, and carboxyl group interact with gold atoms synergistically.

Solvent	$E_{(4\mathbf{a}/4\mathbf{a}^+)}^o$	$\Delta E_1$	$\Delta E_2$	$\Delta E_3$	$\Delta E_4$	$\Delta E_5$
Chloroform	-0.58	-0.47	-0.51	-0.08	-0.21	0.18
THF	-0.63	-0.33	-0.27	0.16	0.03	0.42
DCM	-0.59	-0.26	-0.20	0.23	0.10	0.49
Acetone	-0.50	-0.07	0.00	0.43	0.30	0.69
Methanol	-0.47	-0.01	0.06	0.49	0.36	0.75
Acetonitrile	-0.46	0.00	0.07	0.49	0.36	0.75
Water	-0.44	0.05	0.12	0.54	0.41	0.80
	$E_{(3\mathbf{a}/3\mathbf{a}^+)}^o$					
Chloroform	-0.78	-0.64	-0.57	-0.14	-0.27	0.12
THF	-0.66	-0.40	-0.33	0.10	-0.03	0.38
DCM	-0.63	-0.33	-0.26	0.17	0.04	0.43
Acetone	-0.53	-0.13	-0.06	0.37	0.24	0.63
Methanol	-0.50	-0.07	0.00	0.42	0.29	0.68
Acetonitrile	-0.49	-0.06	0.01	0.43	0.30	0.69
Water	-0.47	-0.01	0.06	0.48	0.35	0.74

$$\Delta E_1 = E_{(Oxidation)}^o + E_{(AuCl_4^-/AuCl_2^-)}^o$$

$$\Delta E_4 = E_{(Oxidation)}^o + E_{(Au^{3+}/Au^{1+})}^o$$

$$\Delta E_2 = E_{(Oxidation)}^o + E_{(AuCl_4^-/Au^0)}^o$$

$$\Delta E_5 = E_{(Oxidation)}^o + E_{(Au^{1+}/Au^0)}^o$$

$$\Delta E_3 = E_{(Oxidation)}^o + E_{(Au^{3+}/Au^0)}^o$$

$$E_{(Oxidation)}^o = E_{(3\mathbf{a}/3\mathbf{a}^+)}^o \quad \text{or} \quad E_{(4\mathbf{a}/4\mathbf{a}^+)}^o$$

Table 4.1: Calculated oxidation potential of **3a** and **4a** in different solvents with B3PW91/6-31+G(D,P) level of theory and basis set (all values are reported in Volts).

The adsorption of the sulfur group of cysteine to clusters of 1,3,5 and 8 gold atoms were computationally studied by Zhao and co-workers, which shows a charge transfer from the gold cluster to the sulfur atom and a combination of the covalent and donor-acceptor interactions in the cluster of three gold atoms [18]. In this work, adsorption sites have also been studied by simulation of **4a** bonded to one gold atom and a cluster of three gold atoms in order to gain an insight into the charge transfer between the compound and the gold groups. Figure 4.13 shows the optimized structure of three possible binding sites of **4a** to the gold group containing one and three atoms [19]. Among all three bonding sites for **4a**–Au, binding mode (A) is the most stable

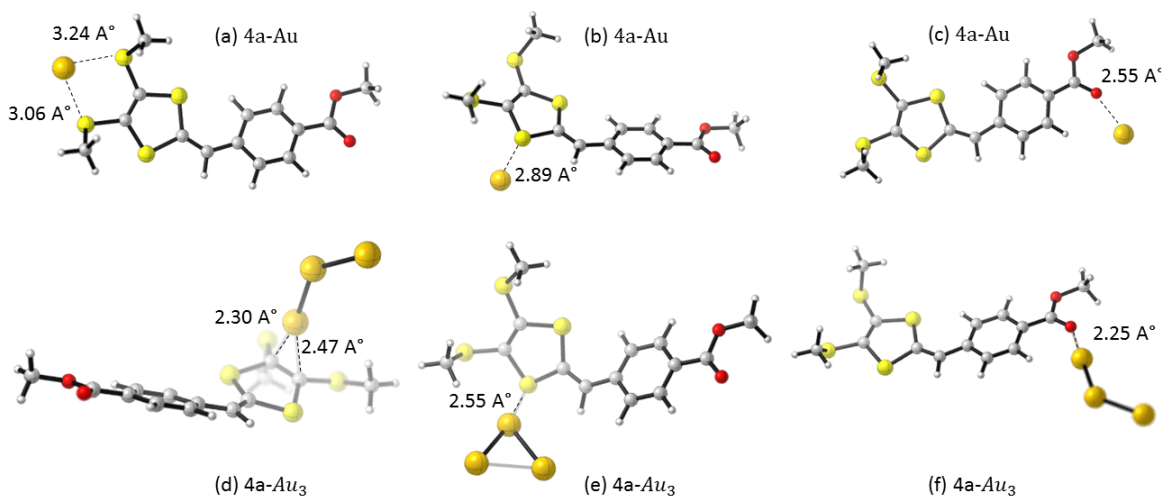


Figure 4.13: Optimized structure of **4a** and a group of gold atoms ( $n=1,3$ ).

structure in both the neutral and the oxidized states. In the case of **4a**–Au<sub>3</sub>, binding mode (F) is the most stable structure in the neutral and cationic state. Indeed, there are many possibilities of bonding, however, only the interactions involving the main functional groups were considered in assessing possible binding structures.

Ionization potential (IP) is defined as the amount of energy required for removing an electron away from a molecule in the gas phase. The adiabatic ionization energy is shown by Equations 4.7 and 4.8. In Equations 4.8, a zero-point vibrational energy

correction was applied.

$$IP = E_{cation} - E_{neutral} \quad (4.7)$$

$$IP = (E_{cation} + ZPVE) - (E_{neutral} + ZPVE) \quad (4.8)$$

To optimize the oxidized state, two different charge distributions were studied, in which the charge was considered to be dispersed over **4a** or the gold group. Ionization energies of both charge distributions show that the positive charge is more localized over **4a** than the Au<sub>n</sub> group. Analysis of Mülliken charge distribution for the lowest energy structures is shown in Figure 4.14. The highest change in charge density

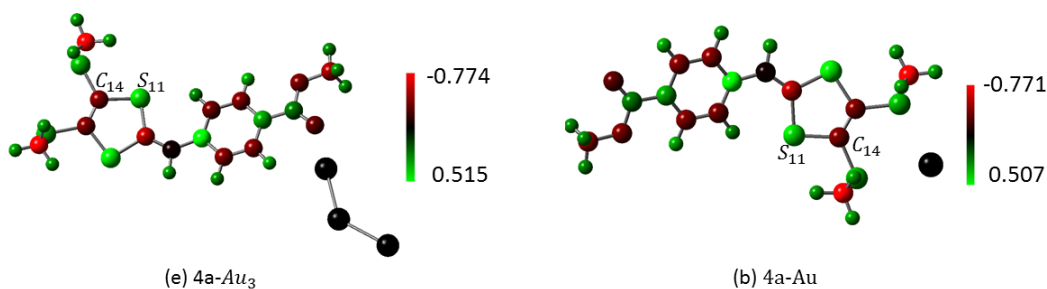


Figure 4.14: Mülliken charge distribution over **4a**-Au<sub>3</sub> after oxidation. Red regions represent a higher concentration of electron density while green shows less electron density.

after oxidation compared to the neutral molecule occurs over S11 and C14 for both complexes as shown in Figure 4.14.

## 4.8 Summary

In the current chapter, AuNPs were synthesized through the reduction of the HAuCl<sub>4</sub> using DTF derivatives as reductants. UV-Vis spectroscopic analysis was used to reveal the redox reaction mechanisms. Experimental results show that in the first redox step, Au(III) is reduced to an Au(I) species (Au(II) is not stable in the presence of an oxidant). DTF is oxidized to the cationic state of DTF. In the second step, a

dimerization reaction occurs on cationic DTF and then an Au(I)-TTFV complex is formed. It has been found that the oxidation of DTF occurs at a much faster rate than the formation of Au-DTF complex. Finally, the characteristic peak of AuNPs can be observed after heating the sample. It is concluded that the substituent on the *para* position of the benzene ring of DTF plays a major role in the formation AuNPs. Nanoparticles did not appear in the solution of DTF with carboxyl substituent and formed a stable Au(I)-dimerized DTF complex instead. Moreover, the polarity of the solvent and temperature directly impact the AuNP formation.

## Bibliography

- [1] James J. Storhoff, Robert Elghanian, Robert C. Mucic, Chad A. Mirkin, and Robert L. Letsinger. One-pot colorimetric differentiation of ppolynucleotides with single base imperfections using gold nanoparticle probes. *J. Am. Chem. Soc.*, 120:1959–1964, 1998.
- [2] Debanjana Ghosh and Nitin Chattopadhyay. Gold nanoparticles: acceptors for efficient energy transfer from the photoexcited fluorophores. *OPJ*, 3:18–26, 2013.
- [3] Axel D. Becke. A new mixing of hartree-fock and local density-functional theories. *J. Chem. Phys.*, 98:1372–1377, 1993.
- [4] Jacopo Tomasi, Benedetta Mennucci, and Roberto Cammi. Quantum mechanical continuum solvation models. *Chemical Reviews*, 105(8):2999–3094, 2005.
- [5] Erich Runge and E. K. U. Gross. Density-functional theory for time-dependent systems. *Phys. Rev. Lett.*, 52:997–1000, 1984.
- [6] M. J. Frisch, G. W. Trucks, H. B. Schlegel, G. E. Scuseria, M. A. Robb, J. R. Cheeseman, G. Scalmani, V. Barone, B. Mennucci, G. A. Petersson, H. Nakatsuji,

- M. Caricato, X. Li, H. P. Hratchian, A. F. Izmaylov, J. Bloino, G. Zheng, J. L. Sonnenberg, M. Hada, M. Ehara, K. Toyota, R. Fukuda, J. Hasegawa, M. Ishida, T. Nakajima, Y. Honda, O. Kitao, H. Nakai, T. Vreven, J. A. Montgomery, Jr., J. E. Peralta, F. Ogliaro, M. Bearpark, J. J. Heyd, E. Brothers, K. N. Kudin, V. N. Staroverov, R. Kobayashi, J. Normand, K. Raghavachari, A. Rendell, J. C. Burant, S. S. Iyengar, J. Tomasi, M. Cossi, N. Rega, J. M. Millam, M. Klene, J. E. Knox, J. B. Cross, V. Bakken, C. Adamo, J. Jaramillo, R. Gomperts, R. E. Stratmann, O. Yazyev, A. J. Austin, R. Cammi, C. Pomelli, J. W. Ochterski, R. L. Martin, K. Morokuma, V. G. Zakrzewski, G. A. Voth, P. Salvador, J. J. Dannenberg, S. Dapprich, A. D. Daniels, ?. Farkas, J. B. Foresman, J. V. Ortiz, J. Cioslowski, and D. J. Fox. Gaussian 09 Revision D.01. Gaussian Inc. Wallingford CT 2009.
- [7] Roy Dennington, Todd Keith, and John Millam. Gaussview Version 5. Semichem Inc. Shawnee Mission KS 2009.
- [8] Yunfei Wang and Yuming Zhao. Dithiafulvenyl-substituted phenylacetylene derivatives: synthesis and structure-property-reactivity relationships. *Org. Biomol. Chem.*, 13:9575–9579, 2015.
- [9] Huaiyong Zhu, Xuebin Ke, Xuzhuang Yang, Sarina Sarina, and Hongwei Liu. Reduction of nitroaromatic compounds on supported gold nanoparticles by visible and ultraviolet light. *Angew. Chem.*, 122:9851–9855, 2010.
- [10] Wolfgang Haiss, Nguyen T. K. Thanh, Jenny Aveyard, , and David G. Fernig. Determination of size and concentration of gold nanoparticles from uv-vis spectra. *Anal. Chem.*, 79:4215–4221, 2007.

- [11] J. Binoy, Jose P. Abraham, I. Hubert Joe, V. George, V. S. Jayakumar, J. Aubard, and O. Faurskov Nielsen. Near-infrared fourier transform raman, surface-enhanced raman scattering and fourier transform infrared spectra and ab initio calculations of the natural product nodakenetin angelate. *J. Raman Spectrosc.*, 36:63–72, 2005.
- [12] Li Shi, Qing Yu, Yiyin Mao, Hubiao Huang, Hongwen Huang, Zhizhen Ye, and Xinsheng Peng. High catalytic performance of gold nanoparticle-gelatin mesoporous composite thin films. *J. Mater. Chem.*, 22:21117–21124, 2012.
- [13] Anna Ericson, Lars I. Elding, and Sofi K. C. Elmroth. Kinetics and mechanism of reduction of gold(iii) complexes by dimethyl sulfide. *J. Chem. Soc., Dalton Trans.*, pages 1159–1164, 1997.
- [14] S Ivanova, C Petit, and V Pitchon. A new preparation method for the formation of gold nanoparticles on an oxide support. *Appl. Catal., A*, 267:191 – 201, 2004.
- [15] Mirjana D. Durovic, Ralph Puchta, Zivadin D. Bugarcic, and Rudi van Eldik. Studies on the reactions of  $[\text{AuCl}_4]^-$  with different nucleophiles in aqueous solution. *Dalton Trans.*, 43:8620–8632, 2014.
- [16] R. G. Bates and V. E. Bower. *J. Res. Natl. Bur. Stand.*, 53:283–290, 1954.
- [17] Li Li, Pedram Jahanian, and Guangzhao Mao. Electrocrystallization of tetrathiafulvalene charge-transfer salt nanorods on gold nanoparticle seeds. *J. Phys. Chem. C*, 118:18771–18782, 2014.
- [18] Yaxue Zhao, Feng Zhou, Huchen Zhou, and Haibin Su. The structural and bonding evolution in cysteine-gold cluster complexes. *Phys. Chem. Chem. Phys.*, 15:1690–1698, 2013.

- [19] Sandhya Rai, N. V. Suresh Kumar, and Harjinder Singh. A theoretical study on interaction of proline with gold cluster. *Bull. Mater. Sci.*, 35:291–295, 2012.

# Chapter 5

## Conclusions and Future Work

This work was aimed at characterizing dithiafulvene and tetrathiafulvalene derivatives as a class of excellent  $\pi$ -electron donors and their interactions with gold nanoparticles. The findings show that the DTF and TTF derivatives could be employed in synthesizing AuNPs decorated with dithiole groups, which have many applications in a variety of disciplines such as biological sensors. The findings suggest that the formation of functionalized AuNPs in aqueous media is a strong motivational factor for investigating the reaction mechanism and simulation of the redox reaction in solution. Moreover, the influence of the DTF adsorption on the substrate properties should be investigated to understand the DTF-gold interactions for further device applications.

The results can be used to improve the electronic properties and design more efficient DTF-based molecular materials/devices. One of the themes to emerge from my computational and experimental analysis is that the DTF molecule binds through face-on orientation on the Au (111) surface at the highest degree of hybridization between the  $\pi$ -electron cloud of DTF and the gold orbitals. The DTF thin film could decrease the Au (111) work function by about 0.1 eV, which is directly proportional to the polarity of the substituents. The results indicate that the major charge density

is distributed over the molecule rather than the surface. These findings are broadly in line with the literature reports, such as the results published by Hyla *et al.* in 2016, Osella *et al.* in 2013, and Li *et al.* in 2009. [1–3]

The mechanistic studies on AuNP formation through reduction with DTF compounds are only supported by UV-Vis spectroscopic evidence. One avenue for further study would be through time-dependent experiments using cyclic voltammetry and NMR techniques. Furthermore, it is important to simulate the active vibrational modes of the DTF on the surface of Au (111) and compare them with the actual Raman spectral data of the compound's thin film on the gold substrate. Such research requires a piece of equipment to produce a uniform thin film of the compound on the surface of gold such as a Langmuir trough, in which the thickness of the film can be carefully controlled. Quantum Espresso was found to be the best available software package for simulation of the Raman bands in the solid state. Future research into orbital overlap population with the band structure data can help understand the covalent nature of the gold and DTF interactions [4, 5].

The size and dimension of synthesized AuNPs must be carefully studied and compared with different common methods such as transmission electron microscopy (TEM), atomic force microscopy (AFM), scanning electron microscopy (SEM), and dynamic light scattering (DLS) in order to discover a suitable method for characterization of nanoparticles [6]. Furthermore, controlling the NPs size and morphology is a critical approach for future work, which can directly impact the properties of particles. Besides, the analysis of the  $\text{HAuCl}_4$  reaction with DTF molecules that are substituted with different end-groups such as thiolester, ester, and carboxyl group can uncover some steps of the reaction mechanism puzzle.

Another possible area for further investigations is the application of DTF in molecular junctions in which organic  $\pi$ -conjugated molecules are used to modify the conduc-

tivity of transistors [7]. Atomic force microscopy (AFM) serves as a facile technique for investigating the electronic properties of organic molecules that covalently bonds to the drain and source [8].

## Bibliography

- [1] Alexander S. Hyla, Paul Winget, Hong Li, Chad Risko, and Jean-Luc Brédas. Work function reduction by a redox-active organometallic sandwich complex. *Org. Electron.*, 37:263 – 270, 2016.
- [2] Silvio Osella, David Cornil, and Jerome Cornil. Work function modification of the (111) gold surface covered by long alkanethiol-based self-assembled monolayers. *Phys. Chem. Chem. Phys.*, 16:2866–2873, 2014.
- [3] Fenghong Li, Yi Zhou, Fengling Zhang, Xianjie Liu, Yiqiang Zhan, and Mats Fahlman. Tuning work function of noble metals as promising cathodes in organic electronic devices. *Chem. Mater.*, 21:2798–2802, 2009.
- [4] Paolo Giannozzi, Stefano Baroni, Nicola Bonini, Matteo Calandra, Roberto Car, Carlo Cavazzoni, Davide Ceresoli, Guido L Chiarotti, Matteo Cococcioni, Ismaila Dabo, Andrea Dal Corso, Stefano de Gironcoli, Stefano Fabris, Guido Fratesi, Ralph Gebauer, Uwe Gerstmann, Christos Gougoussis, Anton Kokalj, Michele Lazzeri, Layla Martin-Samos, Nicola Marzari, Francesco Mauri, Riccardo Mazzarello, Stefano Paolini, Alfredo Pasquarello, Lorenzo Paulatto, Carlo Sbraccia, Sandro Scandolo, Gabriele Sclauzero, Ari P Seitsonen, Alexander Smogunov, Paolo Umari, and Renata M Wentzcovitch. QUANTUM ESPRESSO: a modular and open-source software project for quantum simulations of materials. *Journal of Physics: Condensed Matter*, 21(39):395502 (19pp), 2009.

- [5] Gerold M. Rangger, Lorenz Romaner, Oliver T. Hofmann, Georg Heimel, Michael G. Ramsey, and Egbert Zojer. Analysis of bonding between conjugated organic molecules and noble metal surfaces using orbital overlap populations. *J. Chem. Theory Comput.*, 6:3481–3489, 2010.
- [6] A direct comparison of experimental methods to measure dimensions of synthetic nanoparticles. *Ultramicroscopy*, 182.
- [7] Georg Heimel, Lorenz Romaner, Jean-Luc Brédas, and Egbert Zojer. Interface energetics and level alignment at covalent metal-molecule junctions:  $\pi$ -conjugated thiols on gold. *Phys. Rev. Lett.*, 96:196806, 2006.
- [8] Lanlan Sun, Yuri A. Diaz-Fernandez, Tina A. Gschneidtner, Fredrik Westerlund, Samuel Lara-Avila, and Kasper Moth-Poulsen. Single-molecule electronics: from chemical design to functional devices. *Chem. Soc. Rev.*, 43:7378–7411, 2014.

# Appendix A

## Redox-dependent Properties of DTF-endcapped $\pi$ -Oligomers

\*

### A.1 Electronic Transition and Molecular Orbital Properties

Electronic transition properties for model compound **2b** in different oxidation states were simulated by the TD-DFT method at the B3LYP/6-31++(d,p) level of theory. Detailed electronic transition energies and MO assignments are listed in Tables A.1,A.2, A.3 and A.4. Eigenvalues of frontier molecular orbitals for **2b** are provided in Table A.5, and detailed contour plots for these orbitals are illustrated in Figure A.1 and A.2.

---

\*This appendix provides the supporting information from “Blah blah”, Authors, *Journal* **vol**, pages (year).

Oscillator strength ( $f$ )	Wavelength(nm)	transition	MO contribution
2.665	471	HOMO>LUMO	0.70227
0.7492	352.02	HOMO-1>LUMO-1 HOMO-2>LUMO	0.5212 -0.46202

Table A.1: Assignments of electronic transitions of **2b** in the neutral state.

Oscillator strength ( $f$ )	Wavelength(nm)	transition	MO contribution
1.0425	1823.54	SOMO>LUMO( $\beta$ ) LUMO>SOMO( $\beta$ ) SOMO>LUMO( $\alpha$ )	1.07711 -0.42385 -0.14552
1.2274	592.73	SOMO>LUMO( $\alpha$ ) SOMO>LUMO+2( $\beta$ ) SOMO-1>LUMO+1( $\beta$ ) SOMO-3>SOMO( $\beta$ ) SOMO>LUMO( $\beta$ ) SOMO-2>LUMO( $\alpha$ ) SOMO-1>LUMO+1( $\beta$ ) SOMO>LUMO( $\beta$ ) SOMO-2>LUMO+2( $\alpha$ )	0.82471 -0.33823 0.26939 -0.17459 0.16416 -0.13221 0.12393 -0.11999 -0.10539
0.7142	421.07	SOMO-1>LUMO+1( $\beta$ ) SOMO>LUMO+2( $\beta$ ) SOMO>LUMO( $\alpha$ ) SOMO-2>LUMO( $\alpha$ ) SOMO-1>LUMO+1( $\alpha$ ) SOMO>LUMO( $\beta$ ) SOMO-1>LUMO+3( $\beta$ ) SOMO>LUMO( $\beta$ ) SOMO-2>LUMO+2( $\beta$ )	0.5762 -0.54353 -0.445 -0.30482 0.12183 -0.11847 0.1054 0.10443 -0.101

Table A.2: Assignments of electronic transitions of **2b** in the radical cation state.

Oscillator strength ( $f$ )	Wavelength(nm)	transition	MO contribution
0.9399	1105.1	SOMO>LUMO( $\beta$ )	0.96778
		SOMO>LUMO( $\alpha$ )	-0.19161
		SOMO-1>LUMO+1( $\alpha$ )	0.1396
1.5665	554.93	SOMO>LUMO( $\alpha$ )	0.77272
		SOMO-1>LUMO+1( $\beta$ )	0.47651
		SOMO>LUMO+2( $\beta$ )	0.17438
		SOMO-2>LUMO( $\alpha$ )	0.16635
		SOMO>LUMO+2( $\alpha$ )	-0.14723
		SOMO-3>LUMO( $\beta$ )	-0.12437
		SOMO>LUMO( $\beta$ )	0.11664
		SOMO-2>LUMO+2( $\alpha$ )	-0.10259

Table A.3: Assignments of electronic transitions of **2b** in the dication triplet state.

Oscillator strength ( $f$ )	Wavelength(nm)	transition	MO contribution
2.9995	1025.440	SOMO>LUMO( $\alpha$ )	0.84748
		SOMO>LUMO( $\beta$ )	0.84748
		SOMO>LUMO( $\alpha$ )	-0.47177
		SOMO>LUMO( $\beta$ )	-0.47177
0.7929	397.5	SOMO>LUMO+2( $\alpha$ )	0.57554
		SOMO>LUMO+2( $\beta$ )	0.57554
		SOMO-1>LUMO+1( $\alpha$ )	0.39521
		SOMO-1>LUMO+1( $\beta$ )	0.39521

Table A.4: Assignments of electronic transitions of **2b** the dication singlet state.

	Neu	RC ( $\alpha$ )	RC ( $\beta$ )	DC(T)( $\alpha$ )	DC(T)( $\beta$ )	DC(S)
LUMO+3	-0.745	-2.9721	-3.099	-5.479	-6.235	-5.624
LUMO+2	-0.781	-3.245	-3.870	-5.625	-6.760	-6.438
LUMO+1	-1.485	-4.0271	-4.552	-6.601	-8.687	-7.117
LUMO	-2.121	-4.643	-6.709	-6.986	-8.969	-9.117
HOMO/SOMO	-5.030	-7.434	-7.244	-9.828	-10.388	-9.711
HOMO-1/SOMO-1	-5.277	-7.714	-8.194	-10.290	-11.256	-10.682
HOMO-2/SOMO-2	-6.020	-8.477	-9.038	-10.885	-11.453	-11.540
HOMO-3/SOMO-3	-6.780	-9.254	-9.536	-11.522	-11.842	-11.962
HOMO-4/SOMO-4	-7.157	-9.572	-9.539	-11.636	-11.843	-11.979

Table A.5: Frontier molecular orbital energies of **2b** in various oxidation states.

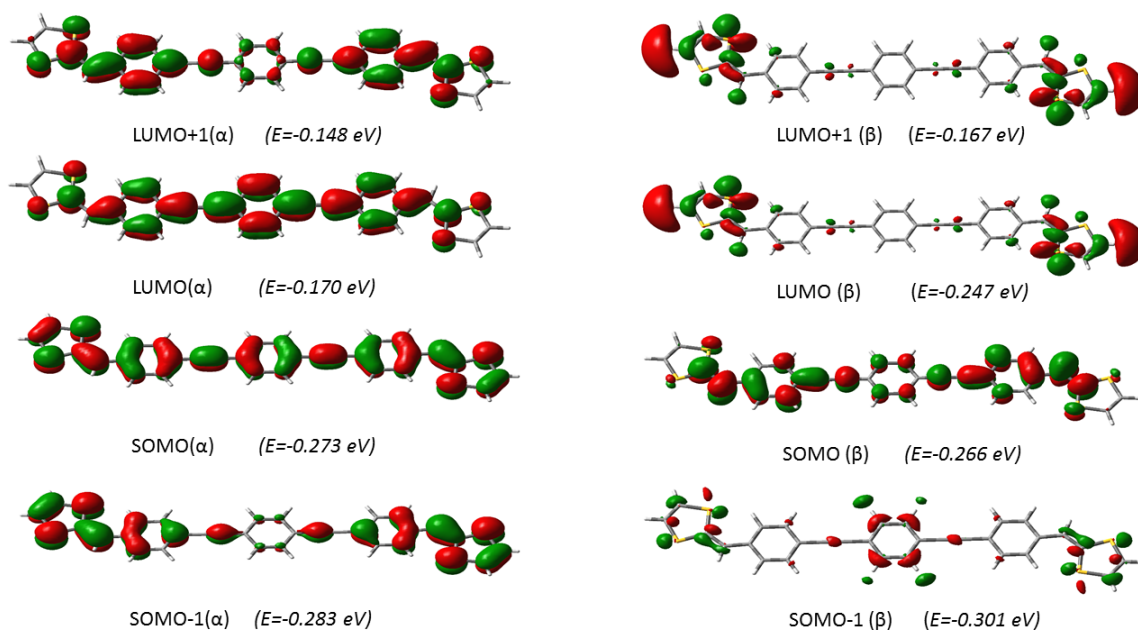


Figure A.1: Contours of frontier MOs for compound **2b** in the radical cation state and their eigenvalues calculated at the B3LYP/6-31++G (d,p) level.

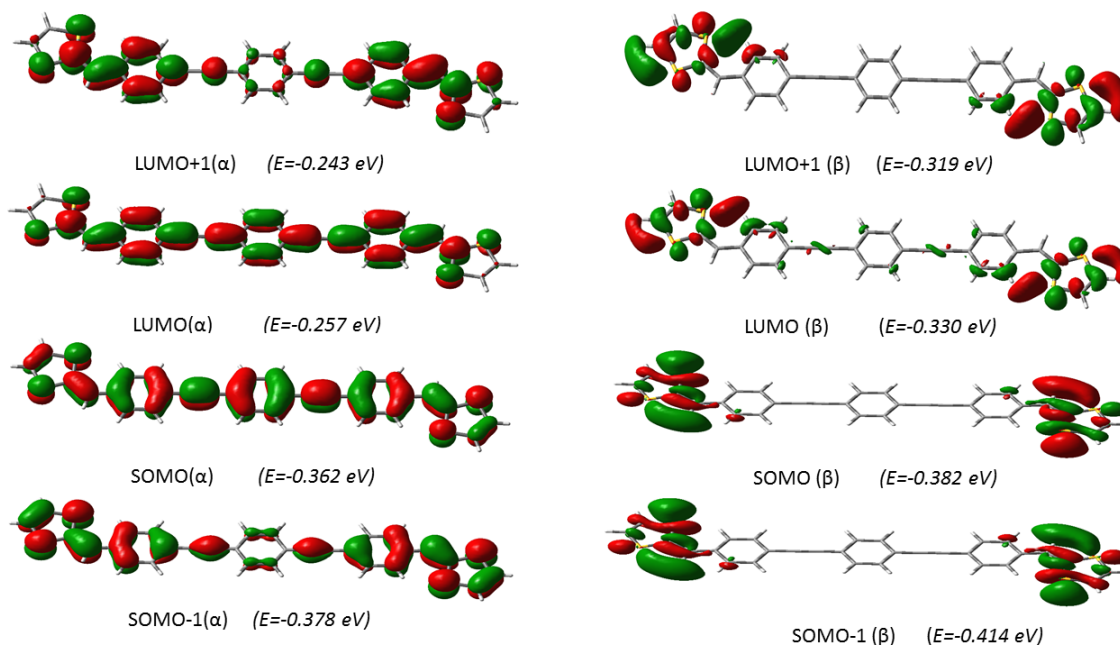


Figure A.2: Contours of frontier MOs for compound **2b** in the triplet dication state and their eigenvalues calculated at the B3LYP/6-31++G (d,p) level.

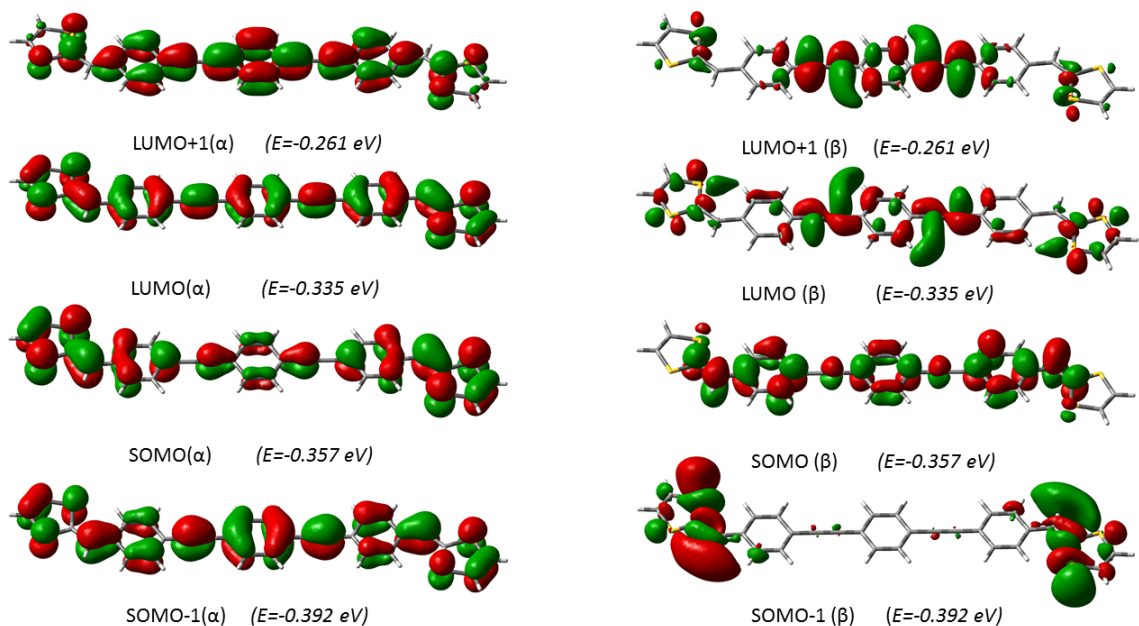


Figure A.3: Contours of frontier MOs for compound **2b** in the singlet dication state and their eigenvalues calculated at the B3LYP/6-31++G (d,p) level.

## A.2 Descriptions of Raman-Active Vibrational Modes

Tables A.6, A.7, A.8 and A.9 list the active vibrational modes of the Raman spectra for compound **2b** in the neutral, radical cation, dication singlet, and triplet states, respectively. DFT-calculated Raman frequencies were found to be slightly lower than experimental values, which can be rationalized by the effect of molecular orientation and inter-molecular interaction in the solid state on the vibrational energies. Figure A.4, A.5, A.6 and A.7 describe the vibrational eigenvectors of the outstanding Raman-active vibrational modes for compound **2b** in the neutral and cationic states.

Entry	$\nu_{cal}(cm^{-1})$	$\nu_{exp}(cm^{-1})$	Mode	$\Delta\nu_{(exp-cal)}$
1	1145.35	1126.7	C–H rocking	18.65
2	1592.35	1541.13	C=C stretching	51.22
3	1621.23	1565.1	C=C stretching	56.13
4	1640.64	1588.8	C–H rocking C=C stretching	51.84
5	2280.39	2203.7	Triple bond stretching	76.69

Table A.6: Raman active vibrational modes for **2b** in the neutral state.

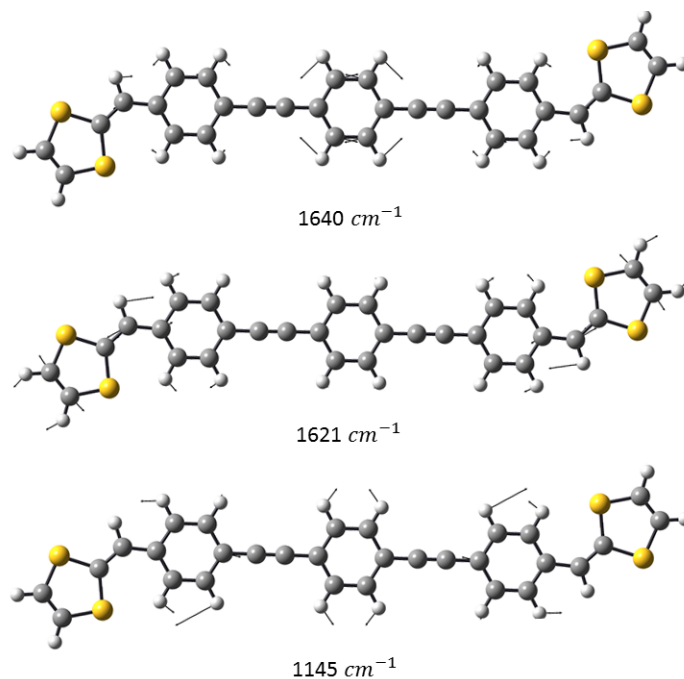


Figure A.4: Raman active vibrational vectors for compound **2b** in the neutral state calculated at the B3LYP/6-31++G(d,p) level.

Entry	$\nu_{cal}(cm^{-1})$	$\nu_{exp}(cm^{-1})$	Mode	$\Delta\nu_{(exp-cal)}$
1	747.16	722.13	C–C Stretching	25.03
2	1133.50	1125.9	C–C Stretching	7.6
3	1225.17	1189.8	C–H rocking	35.37
5	1579.76	1567.9	C–H rocking	11.86
6	1615	1588	C=C Stretching C–H rocking	27
7	3162.28	2898.7	C=C Stretching C–H stretching	263.58

Table A.7: Raman active vibrational modes for **2b** in the radical cation state.

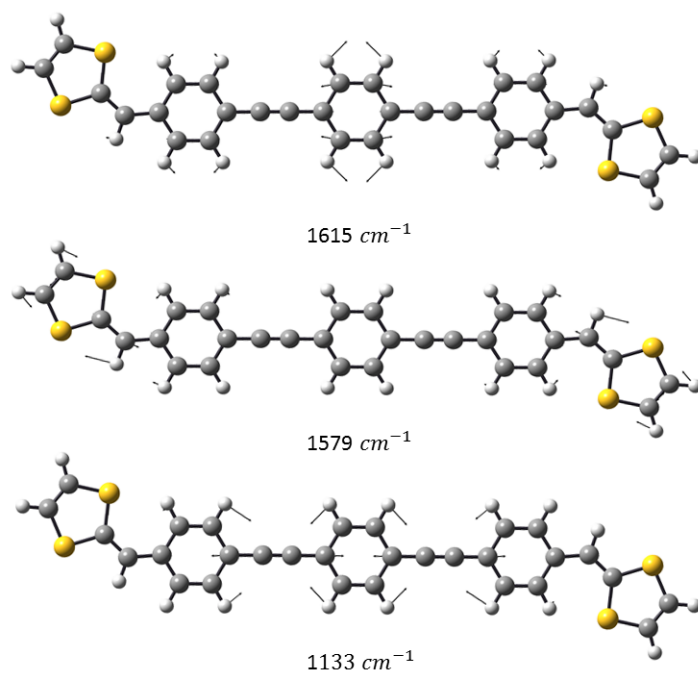


Figure A.5: Raman active vibrational vectors for compound **2b** in the radical cation state calculated at the B3LYP/6-31++G(d,p) level.

Entry	$\nu_{cal}(cm^{-1})$	$\nu_{exp}(cm^{-1})$	Mode	$\Delta\nu_{(exp-cal)}$
1	478.99	514.81	C=C–C bending	35.82
2	1143.76	1108.8	C–H rocking	34.96
3	1209.25	1129.2	C–H rocking	80.05
4	1329.71	1234.6	C–C stretching	95.11
5	1384.91	1293.2	C–H scissoring	91.71
6	1468.39	1369.7	C–H rocking	98.69
7	1514.06	1411.3	C=C Stretching	102.76
8	1549.07	1471.5	C–H rocking	77.57
9	1631.18	1596.2	C=C Stretching	34.98

Table A.8: Raman active vibrational modes for **2b** in the dication triplet state.

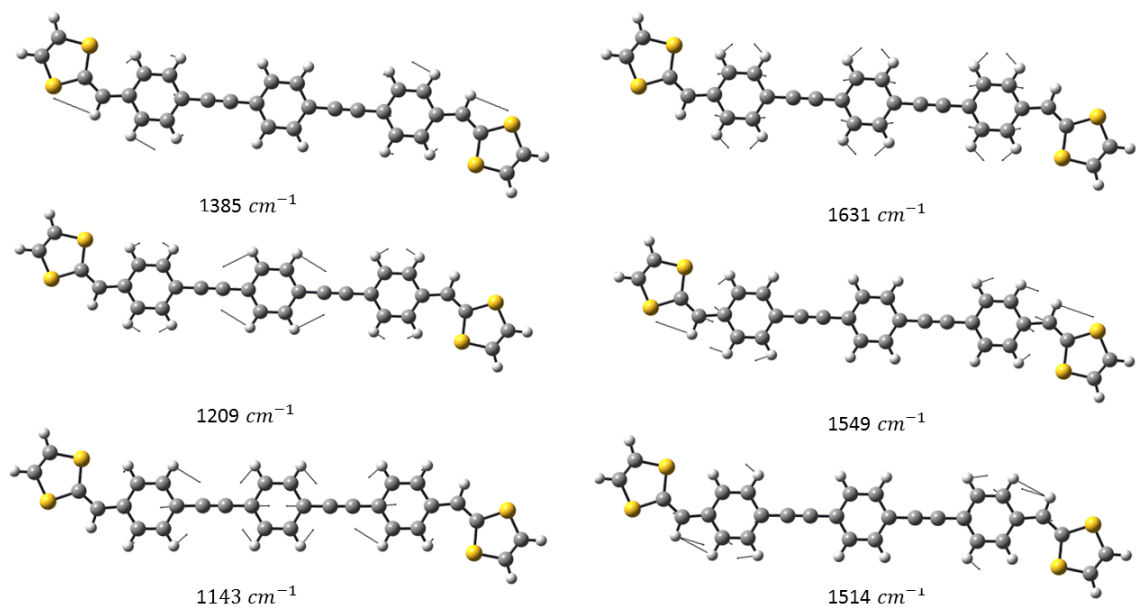


Figure A.6: Raman active vibrational vectors for compound **2b** in the dication triplet state calculated at the B3LYP/6-31++G(d,p) level.

Entry	$\nu_{cal}(cm^{-1})$	Mode
1	1119.57	C–H scissoring C=C benzene rings Stretching
2	1547.20	C=C dithiolenes Stretching
3	1602.43	C–H scissoring C=C benzene rings Stretching
4	2175.40	CC triple bond Stretching

Table A.9: Raman active vibrational modes for **2b** in the dication singlet state.

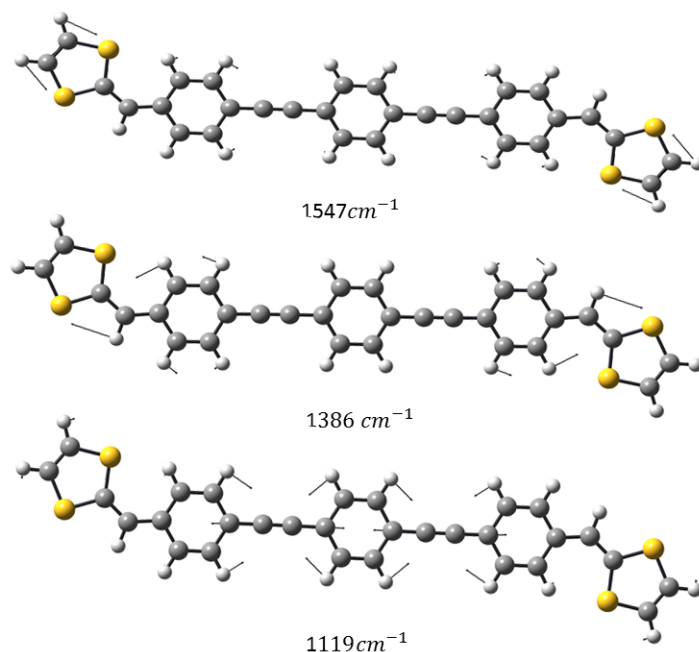


Figure A.7: Raman active vibrational vectors for compound **2b** in the dication singlet state calculated at the B3LYP/6-31++G(d,p) level.

### A.3 Raman Spectra of the Oxidized Film of **2a** After Two Weeks

The film of **2a** spin-cast on a glass substrate was exposed to iodine vapour in a closed beaker. Raman spectra of the film were taken before and after exposure, as discussed in the paper. The film was then left in open air for two weeks and examined by Raman again (Figure A.8).

### A.4 Coordinates of Optimized Geometries and Energies

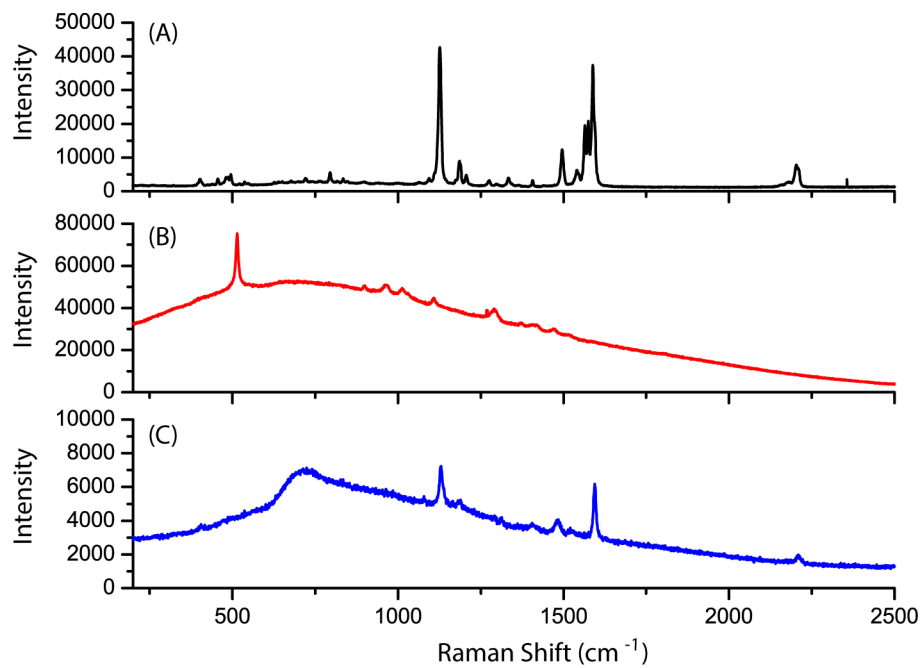


Figure A.8: Raman spectra of the solid thin film of **2a** on a glass substrate measured (A) before exposure to iodine vapour, (B) after exposure to iodine vapour for 65 min, and (C) after being left in open air for two weeks.

C	-0.80951	-1.13922	0.00003
C	0.57189	-1.27504	0.00003
C	1.41112	-0.13879	0.00000
C	0.80951	1.13922	-0.00003
C	-0.57189	1.27504	-0.00003
C	-1.41112	0.13879	-0.00000
H	-1.44185	-2.02114	0.00005
H	1.02008	-2.26332	0.00006
H	1.44185	2.02114	-0.00005
H	-1.02008	2.26332	-0.00006
C	6.05244	-1.82637	0.00010
C	7.43174	-1.96082	0.00011
C	8.29603	-0.83893	0.00004
C	7.68688	0.43685	-0.00004
C	6.30432	0.57856	-0.00005
C	5.45412	-0.54675	0.00002
H	5.41959	-2.70807	0.00016
H	7.86459	-2.95775	0.00018
H	8.28712	1.33787	-0.00010
H	5.86626	1.57157	-0.00012
C	-7.68688	-0.43685	-0.00002
C	-6.30432	-0.57856	-0.00002
C	-5.45412	0.54675	-0.00000
C	-6.05244	1.82637	0.00002
C	-7.43174	1.96082	0.00002
C	-8.29603	0.83893	0.00000
H	-8.28712	-1.33787	-0.00003
H	-5.86626	-1.57157	-0.00003
H	-5.41959	2.70807	0.00003
H	-7.86459	2.95775	0.00004
C	-4.03998	0.39937	-0.00000
C	-2.82639	0.27860	-0.00000
C	2.82639	-0.27860	0.00001
C	4.03998	-0.39937	0.00001
C	9.72830	-1.09681	0.00006
C	-9.72830	1.09681	0.00001
H	-9.98334	2.15501	0.00002
C	-10.79586	0.25562	-0.00000
C	-12.51770	-1.73590	-0.00003
H	-12.89518	-2.75131	-0.00004
C	-13.27698	-0.63197	-0.00001
H	-14.36033	-0.62624	-0.00001
C	10.79586	-0.25562	0.00001
C	13.27698	0.63197	-0.00002
H	14.36033	0.62624	-0.00002
C	12.51770	1.73590	-0.00008
H	12.89518	2.75131	-0.00014
S	12.45768	-0.91901	0.00005
S	10.76962	1.52573	-0.00008
S	-10.76962	-1.52573	-0.00003
S	-12.45768	0.91901	0.00001
H	9.98334	-2.15501	0.00012

Figure A.9: Cartesian coordinates of compound **2b** in the neutral state (sum of electronic and thermal Energies =  $-2746.293943$  Hartree, zero-point correction =  $0.377252$  Hartree)

C	0.80513	-1.14884	-0.00009
C	-0.57044	-1.28151	-0.00010
C	-1.40733	-0.13576	-0.00000
C	-0.80513	1.14884	0.00010
C	0.57044	1.28150	0.00011
C	1.40733	0.13576	0.00001
H	1.43845	-2.02949	-0.00017
H	-1.02360	-2.26700	-0.00018
H	-1.43845	2.02948	0.00018
H	1.02360	2.26700	0.00018
C	-6.02603	-1.82681	-0.00011
C	-7.39872	-1.95970	-0.00011
C	-8.26477	-0.82932	-0.00001
C	-7.65447	0.45406	0.00010
C	-6.27936	0.59446	0.00010
C	-5.42834	-0.53991	-0.00000
H	-5.39127	-2.70644	-0.00018
H	-7.83492	-2.95438	-0.00018
H	-8.25519	1.35442	0.00020
H	-5.83718	1.58510	0.00019
C	7.65447	-0.45406	-0.00003
C	6.27936	-0.59446	-0.00005
C	5.42834	0.53991	0.00004
C	6.02603	1.82681	0.00014
C	7.39872	1.95969	0.00016
C	8.26477	0.82932	0.00007
H	8.25519	-1.35442	-0.00010
H	5.83718	-1.58511	-0.00013
H	5.39126	2.70643	0.00021
H	7.83491	2.95438	0.00024
C	4.02836	0.39297	0.00003
C	2.80973	0.27216	0.00002
C	-2.80973	-0.27216	-0.00000
C	-4.02836	-0.39297	-0.00000
C	-9.67873	-1.08766	-0.00002
C	9.67873	1.08766	0.00010
H	9.93720	2.14453	0.00019
C	10.76308	0.24046	0.00003
C	12.49153	-1.72094	-0.00015
H	12.87883	-2.73266	-0.00024
C	13.23910	-0.60401	-0.00004
H	14.32229	-0.58197	-0.00004
C	-10.76308	-0.24046	-0.00001
C	-13.23910	0.60401	-0.00003
H	-14.32229	0.58197	-0.00004
C	-12.49153	1.72094	-0.00003
H	-12.87882	2.73266	-0.00003
S	-12.39503	-0.92287	-0.00002
S	-10.75160	1.52196	-0.00001
S	10.75160	-1.52196	-0.00014
S	12.39503	0.92287	0.00009
H	-9.93720	-2.14452	-0.00005

Figure A.10: Cartesian coordinates of compound **2b** in the radical cation state (Sum of electronic and thermal Energies =  $-2746.077723$  Hartree, zero-point correction =  $0.378033$  Hartree)

C	0.79712	-1.16188	-0.00009
C	-0.57253	-1.28716	-0.00009
C	-1.40610	-0.12867	-0.00001
C	-0.79712	1.16187	0.00008
C	0.57253	1.28715	0.00009
C	1.40610	0.12866	0.00001
H	1.42847	-2.04359	-0.00015
H	-1.03328	-2.26883	-0.00016
H	-1.42847	2.04358	0.00015
H	1.03328	2.26882	0.00016
C	-6.00248	-1.81930	-0.00012
C	-7.36821	-1.95252	-0.00013
C	-8.23970	-0.81439	-0.00005
C	-7.62844	0.47856	0.00005
C	-6.26111	0.61963	0.00006
C	-5.40539	-0.52338	-0.00003
H	-5.36486	-2.69644	-0.00019
H	-7.80596	-2.94603	-0.00020
H	-8.23136	1.37740	0.00012
H	-5.81659	1.60892	0.00013
C	7.62844	-0.47856	-0.00004
C	6.26111	-0.61964	-0.00005
C	5.40539	0.52338	0.00003
C	6.00248	1.81929	0.00013
C	7.36821	1.95252	0.00014
C	8.23970	0.81439	0.00006
H	8.23136	-1.37740	-0.00010
H	5.81660	-1.60893	-0.00012
H	5.36486	2.69644	0.00019
H	7.80596	2.94603	0.00021
C	4.02030	0.37625	0.00002
C	2.79482	0.25786	0.00001
C	-2.79482	-0.25787	-0.00002
C	-4.02030	-0.37626	-0.00002
C	-9.63479	-1.07601	-0.00007
C	9.63479	1.07602	0.00008
H	9.89403	2.13248	0.00016
C	10.74108	0.22614	0.00002
C	12.48590	-1.69871	-0.00011
H	12.88831	-2.70506	-0.00018
C	13.21716	-0.56473	-0.00002
H	14.30029	-0.52208	-0.00001
C	-10.74108	-0.22614	-0.00002
C	-13.21716	0.56474	0.00002
H	-14.30029	0.52209	0.00001
C	-12.48590	1.69872	0.00007
H	-12.88830	2.70507	0.00012
S	-12.34244	-0.93380	-0.00006
S	-10.75351	1.51897	0.00006
S	10.75352	-1.51896	-0.00010
S	12.34244	0.93381	0.00008
H	-9.89404	-2.13248	-0.00013

Figure A.11: Cartesian coordinates of compound **2b** in the dication singlet state (sum of electronic and thermal Energies =  $-2745.773027$  Hartree, zero-point correction =  $0.378722$  Hartree)

C	0.79923	-1.15417	-0.00010
C	-0.58052	-1.27796	-0.00010
C	-1.40285	-0.12593	-0.00001
C	-0.79923	1.15413	0.00009
C	0.58052	1.27792	0.00010
C	1.40285	0.12590	0.00001
H	1.42577	-2.03939	-0.00017
H	-1.03931	-2.26061	-0.00018
H	-1.42577	2.03935	0.00016
H	1.03930	2.26058	0.00017
C	-6.02506	-1.80723	-0.00011
C	-7.39599	-1.94135	-0.00011
C	-8.26173	-0.80508	-0.00002
C	-7.65335	0.48397	0.00008
C	-6.28163	0.62327	0.00008
C	-5.43190	-0.51714	-0.00002
H	-5.38871	-2.68511	-0.00019
H	-7.83236	-2.93568	-0.00019
H	-8.25434	1.38451	0.00017
H	-5.83661	1.61215	0.00016
C	7.65336	-0.48397	-0.00003
C	6.28163	-0.62329	-0.00005
C	5.43189	0.51712	0.00004
C	6.02505	1.80721	0.00014
C	7.39598	1.94134	0.00015
C	8.26173	0.80509	0.00007
H	8.25435	-1.38450	-0.00010
H	5.83662	-1.61217	-0.00013
H	5.38869	2.68509	0.00021
H	7.83234	2.93568	0.00024
C	4.03101	0.37034	0.00002
C	2.81352	0.25458	0.00001
C	-2.81352	-0.25461	-0.00001
C	-4.03101	-0.37037	-0.00002
C	-9.66291	-1.06896	-0.00004
C	9.66290	1.06898	0.00010
H	9.91796	2.12689	0.00019
C	10.77356	0.22491	0.00003
C	12.51995	-1.69097	-0.00014
H	12.92836	-2.69511	-0.00022
C	13.24895	-0.55280	-0.00003
H	14.33213	-0.50825	-0.00002
C	-10.77356	-0.22489	-0.00002
C	-13.24894	0.55284	0.00000
H	-14.33213	0.50829	0.00001
C	-12.51994	1.69101	0.00001
H	-12.92834	2.69514	0.00002
S	-12.37132	-0.94000	-0.00001
S	-10.79023	1.51991	-0.00001
S	10.79024	-1.51989	-0.00013
S	12.37131	0.94003	0.00010
H	-9.91797	-2.12688	-0.00008

Figure A.12: Cartesian coordinates of compound **2b** in the dication triplet state (sum of electronic and thermal Energies =  $-2745.779398$  Hartree, zero-point correction =  $0.378547$  Hartree)

# Appendix B

## Redox-dependent Properties of DTF-endcapped $\pi$ -Oligomers

### B.1 NLO Properties

NLO properties of DTF-end capped  $\pi$ -oligomers are calculated at the B3LYP/6-31++G (d,p) level and shown in Table B.1. Results show relatively high  $\gamma$  polarizability than  $\alpha$  which is found to be much higher for neutral molecule, while  $\beta$  and  $\mu$  polarizability calculated to be zero. Equation B.1 can calculate the total dipole moment.

$$\mu = \sqrt{\mu_x^2 + \mu_y^2 + \mu_z^2} \quad (\text{B.1})$$

In this equation  $\mu_x, \mu_y, \mu_z$  are dipole moments in x, y, z directions. The mean polarizability can be achieved by Equation B.2.

$$\alpha_0 = \frac{\alpha_{xx} + \alpha_{yy} + \alpha_{zz}}{3} \quad (\text{B.2})$$

where  $\alpha_{xx}$ ,  $\alpha_{yy}$ ,  $\alpha_{zz}$  are polarizability tensors. Anisotropy polarizability can be derived from Equation B.3.

$$\Delta\alpha = \frac{1}{\sqrt{2}} \sqrt{(\alpha_{xx} - \alpha_{yy})^2 + (\alpha_{yy} - \alpha_{zz})^2 + (\alpha_{zz} - \alpha_{xx})^2 + 6\alpha_{xx}^2} \quad (\text{B.3})$$

The first hyper-polarizability is obtained by Equation B.4.

$$\beta_i = \beta_{iji} + \frac{1}{3} \sum_{i \neq j} (\beta_{iji} + \beta_{jjj} + \beta_{jji}) \quad (\text{B.4})$$

where i, j are x, y or z directions. First hyper-polarizability can be derived also by the complete Equation B.5.

$$\beta_0 = \sqrt{(\beta_{xxx} + \beta_{xyy} + \beta_{xzz})^2 + (\beta_{yyy} + \beta_{xxy} + \beta_{xzz})^2 + (\beta_{zzz} + \beta_{xxz} + \beta_{yyz})^2} \quad (\text{B.5})$$

Diradical dication with singlet multiplicity shows higher  $\gamma$  value than triplet.

## B.2 Phenol Detection

UV-Vis spectroscopy was tested to detect the presence of phenol on the surface of DTF. First, a glass slide that was coated with a layer of gold was immersed in the solution of DTF in the toluene for two hours. Second, the surface was then washed with deionized water and finally, the prepared glass slide immersed in the solution of 500 ppm toluene for two more hours. The UV-vis spectra of the surface at different stages regarding the bare glass slide are shown in Figure B.1. As can be seen, the absorption peak at 600 nm shifts to higher wavenumbers with a decrease in intensity of absorbance. Based on the discussion in chapter 4, the broad peak at 600 nm may come from oxidized form of DTF. Raman spectra of the same surfaces are also taken

	Neutral	Radical cation	Diradical dication (T)	Diradical dication (S)
$\alpha_{xx}$	-96.893	328.170	813.407	744.522
$\alpha_{xy}$	23.910	-24.004	-24.728	-24.463
$\alpha_{yy}$	-202.027	-187.007	-172.007	-172.583
$\alpha_{xz}$	0.000	0.000	0.000	0.001
$\alpha_{yz}$	-0.001	0.003	0.004	0.004
$\alpha_{zz}$	-242.263	-236.230	-230.428	-344.370
$\alpha_{tot}$	-180.394	-47.533	205.486	113.785
$\Delta\alpha$	136.445	543.063	1016.787	1014.857
$\beta_{xxx}$	0.001	0.000	0.001	0.002
$\beta_{xxy}$	0.000	0.001	0.012	0.003
$\beta_{xyy}$	0.000	0.000	0.0018	0.001
$\beta_{yyy}$	0.000	0.000	0.000	0.000
$\beta_{xxz}$	-0.009	-0.025	-0.0136	-0.003
$\beta_{xyz}$	-0.011	0.011	0.012	0.003
$\beta_{yyz}$	0.000	-0.001	-0.001	0.000
$\beta_{xzz}$	0.000	0.000	0.00	0.000
$\beta_{yzz}$	0.00	0.000	0.000	0.000
$\beta_{zzz}$	0.000	0.000	0.000	0.000
$\beta_{tot}$	0.00	0.000	0.000	0.000
$\gamma_{xxxx}$	-69350.794	-10113.167	57839.151	47191.500
$\gamma_{yyyy}$	-1945.308	-1831.913	-1710.711	-1722.871
$\gamma_{xxyy}$	-15798.182	-14352.120	-12908.171	-13024.471
$\gamma_{zzzz}$	-308.362	-289.519	-272.658	-273.138
$\gamma_{xxzz}$	-18599.343	-17921.593	-17352.445	-17334.211
$\gamma_{yyzz}$	-451.836	-433.860	-413.457	-416.930
$\gamma_{tot}$	-28260.637	-15529.981	-1098.472	-3271.147
$\mu_x$	0.000	0.000	0.000	0.000
$\mu_y$	0.000	0.000	0.000	0.000
$\mu_z$	0.000	0.000	0.000	0.000
$\mu_{tot}$	0.000	0.000	0.000	0.000

Table B.1: The electric dipole moment ( $\mu$ ,D), polarizability ( $\alpha$ ), first hyperpolarizability ( $\beta$ ), and second hyperpolarizability ( $\gamma$ ) of investigated compounds at B3LYP/6-31++G(d,p) level.

and shown in Figure B.2. There is no detectable change in Raman spectra after immersion in the phenol.

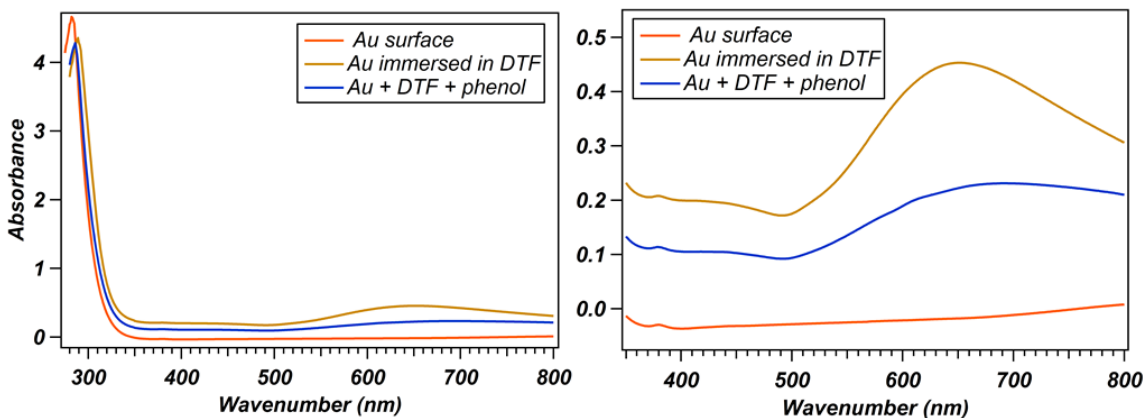


Figure B.1: UV-Vis spectra of (orange) glass slide that are coated with gold layer (yellow) coated glass slide with gold that was then immersed in the solution of DTF, that is dissolved in toluene, for two hours (blue) the prepared surface that was immersed in the phenol solution with concentration of 500 ppm for two hours.

### B.3 UV-Vis Spectra of DTF and $\text{HAuCl}_4$

Figure B.3 shows the UV-Vis spectra of DTF dissolved in toluene and mixed with gold acid. The gold peak intensity at 330 nm dramatically decreases after mixing it with DTF solution which represents the reaction processed. The DTF peak at 400 nm shifts to higher wavenumbers which are due to the bonding of compounds with gold species (chapter 4).

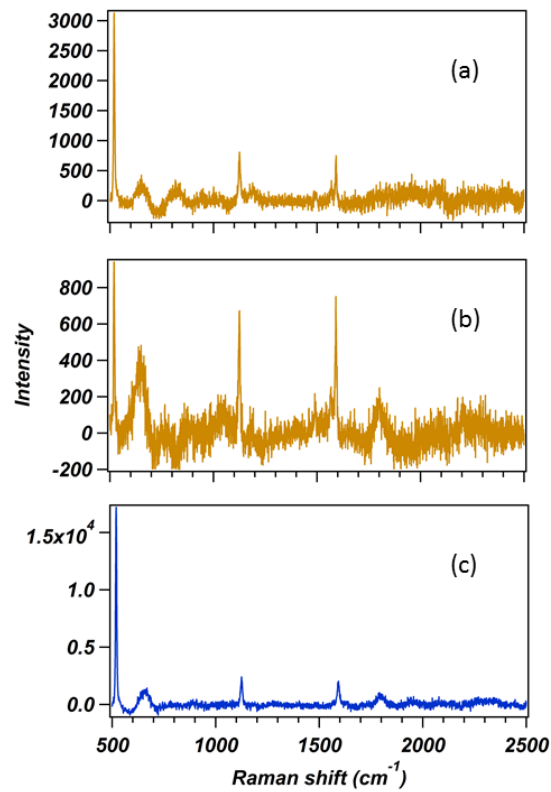


Figure B.2: Raman spectra of (a) glass slide that is coated with gold layer and then immersed in the solution of DTF, that is dissolved in toluene, for two hours (b) glass slide that is coated with gold layer and then immersed in the solution of DTF, that is dissolved in toluene, for twenty-two hours (c) the prepared surface that was immersed in the phenol solution with concentration of 500 ppm for two hours.

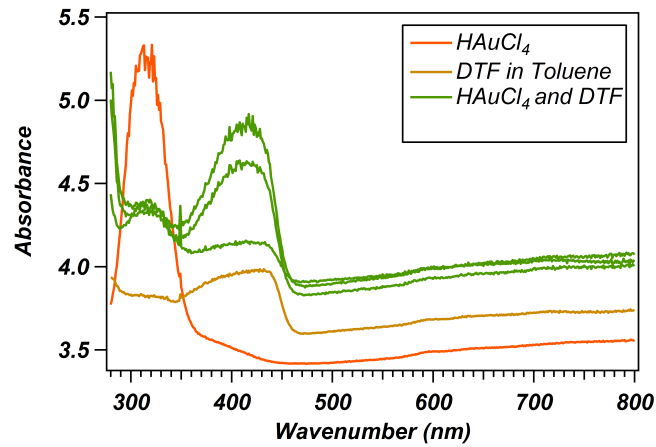


Figure B.3: UV-Vis spectra of .

# Appendix C

## SAM formation of Dithiafulvene

### Derivatives on Au(111):

### Orientalional Geometry, Binding

### Energies and Work Function

#### C.1 Geometry Optimization and Electronic Property Calculations

As it is mentioned in the chapter 3, the molecule should be optimized in a very large cell to prevent interacting with nearby molecules. In Figure C.1, the total energy of the single DTF **3a** in the cell is plotted against cell dimensions with and without considering vdW interactions. Both plots reach a plateau at the dimension of (20,15,15) Å. So the corresponding cell dimension was employed for further calculations. Energy increases by considering dispersion correction from (15,8,8) to (20,15,15) Å, which is due to reducing the effect of vdW interaction by increasing the molecule-molecule

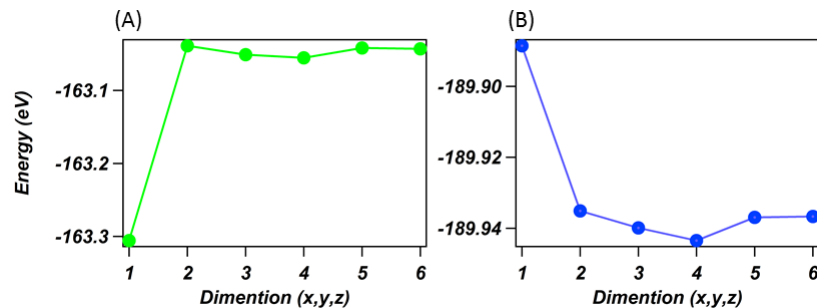


Figure C.1: Energy variation by increasing the cell lengths in (x, y,z) directions with (A) and without (B) dispersion correction. The numbers that are shown on the x-axis stand for (15,8,8), (20,15,15), (24,17,17), (25,20,20), (25,25,25) and (30,25,25) dimensions, respectively. All total energies have been obtained by  $5 \times 5 \times 1$  number of k-points.

distances. Therefore the overall stability of cell decreases. Calculation without considering the vdW interaction shows that the stability of the cell rises by expanding the cell dimensions due to the reduction of the repulsion forces.

Table C.1, shows the binding energy of the DTF **3a** adsorbed on the surface of Au (111) at different starting orientational geometries.

Table C.2 shows the distance of the gold substrate to the DTF derivative's sulfur atoms ( $S_1$  and  $S_{c_2}$ ) along with the magnitude of change in  $C_4-C_5$  and  $C_3-S_1$  dihedral angle.

## C.2 Molecular Work Function

Table C.3 shows the work function of the sole DTF derivatives in a very large unit cell.

Orientation	Angle ( $^{\circ}$ )	$E_B$	$\epsilon_F$	$\varphi$
Vertical through carboxyl	30	-2.942 (+0.063)	-1.78 (-1.72)	3.34 (3.40)
	45	-0.724 (+0.060)	-1.81 (-1.72)	3.35 (3.39)
	75	-0.687 (+0.021)	-1.80 (-1.69)	3.34 (3.38)
	90	-0.684 (+0.075)	-1.82 (-1.74)	3.36 (3.40)
Vertical through dithiol	30	-3.052 (-0.217)	-1.81 (-1.73)	3.36 (3.41)
	45	-2.349 (-0.232)	-1.84 (-1.75)	3.38 (3.41)
	75	-1.781 (-0.183)	-1.90 (-1.78)	3.41 (3.43)
	90	-1.244 (-0.014)	-1.95 (-1.85)	3.42 (3.46)
Edge-on 2	30	-3.005 (-0.028)	-1.79 (-1.75)	3.35 (3.41)
	45	-2.788 (+0.002)	-1.79 (-1.76)	3.35 (3.42)
	75	-2.336 (+0.019)	-1.78 (-1.78)	3.35 (3.42)
	90	-1.032 (+0.041)	-1.81 (-1.94)	3.42 (3.44)
Edge-on 1	30	-3.184 (-0.218)	-1.79 (-1.71)	3.35 (3.40)
	45	-3.177 (-0.317)	-1.79 (-1.71)	3.35 (3.40)
	75	-3.172 (-0.245)	-1.79 (-1.72)	3.35 (3.40)
	90	-2.877 (+0.045)	-1.78 (-1.79)	3.34 (3.47)
Face-on	B	-3.009 (-0.114)	-1.79 (-1.73)	3.35 (3.43)
	S	-3.197 (-0.276)	-1.79 (-1.68)	3.35 (3.36)

Table C.1: Calculated binding energies ( $E_B$ ), Fermi energies ( $\epsilon_F$ ) and work-function ( $\varphi$ ) of the DTF **3a** at eighteen different orientations on the surface of Au(111) with (without) dispersion correction. All values are reported in eV. B stands for the benzene plane and "S" stands for the dithiol plane.

	$d_{Au-S_1}$	$d_{Au-S_{C_2}}$	$\Delta\Phi$
NO <sub>2</sub>	2.79 (3.20)	2.57 (2.67)	7.54 (11.86)
CN	3.17 (3.73)	2.64 (3.75)	9.33 (8.49)
CHO	2.85 (3.57)	2.67 (3.43)	2.44 (6.02)
OCH <sub>3</sub>	2.62 (3.47)	2.55 (3.56)	2.50 (10.37)
Br	3.51 (3.83)	2.57 (2.63)	-6.60 (0.08)
NH <sub>2</sub>	2.58 (3.42)	2.64 (3.82)	4.77 (7.22)

Table C.2: Table shows the Au-S<sub>1</sub> and Au-S<sub>C<sub>2</sub></sub> distances (d) in Å along with the C<sub>4</sub>-C<sub>5</sub> and C<sub>3</sub>-S<sub>1</sub> dihedral angle change between plane of bonds ( $\Delta\Phi$ ) by deposition on the A (111).

	$\Phi_{DTF}$
NO <sub>2</sub>	4.64 (4.64)
CN	4.51 (4.53)
CHO	4.51 (4.50)
Br	4.26 (4.26)
OCH <sub>3</sub>	3.92 (3.96)
NH <sub>2</sub>	3.82 (3.73)

Table C.3: Molecular work function  $\varphi$  of the DTF derivatives in the unit cell with (without) dispersion correction. All values are reported in eV.

### C.3 Polarizability

The polarizability values for DTF derivatives with different substitutes at para position of the benzene ring are listed in Table C.4.

### C.4 Raman Spectra of Gold Substrate

Figure C.2 shows the Raman spectra of the bare gold substrate that doesn't show any characteristic peak. The broad peak at  $1600\text{ cm}^{-1}$  doesn't have any overlap with the spectra of deposited compound on the substrate.

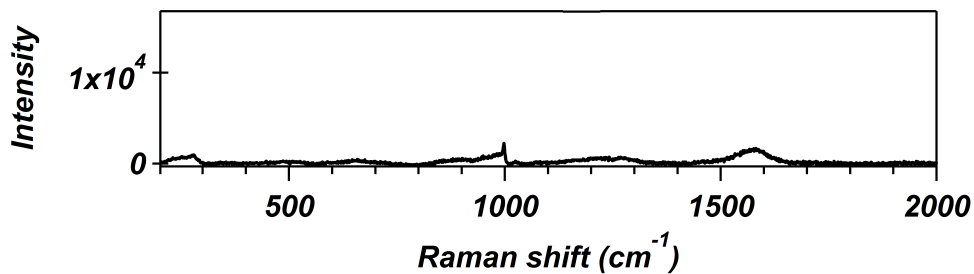


Figure C.2: Raman spectra of the prepared gold substrate.

	Br	CHO	CN	COOH	NH <sub>2</sub>	OCH <sub>3</sub>	NO <sub>2</sub>
$\mu_x$	-2.4	-5.5	-6.5	-4.1	2.7	1.7	-7.5
$\mu_y$	-0.9	0.0	-1.9	-0.1	-0.1	-1.1	-1.2
$\mu_z$	2.6	1.8	2.3	2.2	2.1	3.4	2.3
$\mu_{tot}$	3.7	5.8	7.2	4.6	3.4	4.0	8.1
$\alpha_{xx}$	-146.0	-170.4	-180.7	-152.7	-102.8	-116.2	-181.6
$\alpha_{xy}$	1.6	7.4	-8.5	11.5	4.0	-2.4	-5.0
$\alpha_{yy}$	10.6	23.0	25.2	-125.9	-119.0	-126.1	-126.7
$\alpha_{xz}$	-11.1	-15.1	-11.3	-14.7	-11.7	-3.6	-12.1
$\alpha_{yz}$	-1.4	-0.8	-1.5	0.4	-3.5	-1.5	-140.0
$\alpha_{zz}$	-3.8	5.6	10.0	-141.8	-132.6	-136.2	0.45
$\alpha_{tot}$	-46.4	-47.3	-48.5	-140.1	-118.1	-126.2	-149.4
$\Delta\alpha$	151.1	187.7	200.3	39.9	34.1	19.1	54.6
$\beta_{xxx}$	77.5	-407.5	-542.4	-147.8	220.0	177.6	-425.4
$\beta_{xxy}$	-36.5	-3.5	-122.6	45.9	-14.9	-56.4	-86.9
$\beta_{yyz}$	24.9	22.2	21.5	23.2	19.5	22.1	23.1
$\beta_{yyy}$	22.7	9.1	6.2	11.8	15.8	14.7	4.6
$\beta_{xxz}$	62.7	-1.3	24.1	9.5	17.4	84.9	32.1
$\beta_{xyz}$	-10.5	-9.0	-14.1	-4.5	-22.7	-6.7	-3.8
$\beta_{zzz}$	14.1	11.2	8.3	10.3	9.3	13.2	10.6
$\beta_{xzz}$	42.8	-16.7	-24.5	-9.1	-21.6	-6.2	0.3
$\beta_{xyy}$	39.9	-5.0	-29.2	-1.0	-5.6	-16.6	-26.7
$\beta_{yzz}$	10.9	5.3	4.9	8.7	3.8	6.6	8.5
$\beta_{tot}$	18014.7	92693.0	185324.2	15585.0	19655.3	19845.4	106948.0
$\gamma_{tot}$	-4886.1	-4860.5	-5090.5	-4864.0	-3305.6	-4050.1	-5295.1

Table C.4: The electric dipole moment ( $\mu$ ,D), polarizability ( $\alpha$ ), first hyperpolarizability ( $\beta$ ), and second hyperpolarizability ( $\gamma$ ) of DTF derivatives with different substitutes at para position of benzene ring with B3PW91/6-31+G(d,p) level of theory.

# Appendix D

## Vienna Ab-initio Simulation Package (VASP)

### D.1 Introduction

The VASP software package [1–4] is based on ab-initio quantum mechanical simulation which computes the Schrödinger equation by density functional theory using plane wave basis sets in order to consider the electronic charge density and the local potential effect of electrons. Periodic calculations were implemented based on the plane wave density functional theory. The interactions between the electrons and ions are described using pseudopotentials or the projector-augmented-wave (PAW) method. [5,6]

### D.2 Pseudopotentials and PAW

Matter consists of core electrons, that are closely localized at inner atomic shells, and valence electrons that exist in outer electronic shells. The core electron wave functions

cannot be accurately describe by plane wave basis sets due to the large number of wave functions needed to describe the oscillations. Furthermore, the chemical nature of the core electrons remain constant in different chemical environments and can be included in the calculation by pseudopotential approximations. Therefore, the effective ionic potential of core electrons on the valence shells are considered instead in this approximation.

There are three types of potentials accessible through the VASP package, including:

1. norm-conserving pseudopotentials
2. ultra-soft pseudopotentials
3. PAW potentials

In all different methods, the core electrons are kept frozen for the above-mentioned reasons. In the PAW technique, the oscillatory wave functions of the valence shell electrons are Fourier transformed to well-behaved and smooth wave functions. The PAW total energy is a slightly modified functional of ultrasoft pseudopotentials which is obtained by linearization of two terms of pseudopotential total energy functional. [5,7]. All information about the quantum calculation of pseudopotentials and PAW can be found in detail at:

1. [cms.mpi.univie.ac.at/wiki/index.php/VASP\\_workshop](http://cms.mpi.univie.ac.at/wiki/index.php/VASP_workshop)
2. [www.vasp.at/index.php/documentation](http://www.vasp.at/index.php/documentation)

## D.3 Periodic boundary condition

The periodic boundary condition is used to accurately model the crystalline structure that is infinite in x and y directions in which each unit cell is surrounded by an infinite

number of identical unit cells. In the slab simulation, the adjacent unit cells should not be interacting in the z direction [8].

## D.4 Reciprocal space and k-points

Density functional theory is performed by using pseudopotentials in reciprocal space by using Fourier transforms. The smallest repetition unit in reciprocal space is the Brillouin zone defined by k vectors and containing k-points [9, 10].

In this work, the FCC crystal structure optimization of the Au is computed with  $21 \times 21 \times 21$  k-points. For the calculation of energy and electronic properties of the slab (and slab plus molecule), calculations at the  $\Gamma$  point only were sufficient. An increase in the number of k-points doesn't significantly impact the total energy and the electronic properties. Furthermore, the calculated work functions at  $\Gamma$  match well with experimental values. Moreover, all calculated energies and properties were used to compare adsorption orientations or effect of substituents. In using a difference between two values, these comparisons cancel out the intrinsic error of choosing the number of k-points in reciprocal space.

All optimization parameters such as k-points and cutoff energy should be identical in order to compare the energy and electronic properties of systems. Figure D.1 represents a sample INCAR file that was used to optimize and compute the work-function for the adsorbent on the surface as described in detail in chapter 3.

## Bibliography

- [1] G. Kresse and J. Hafner. Ab initio molecular dynamics for liquid metals. *Phys. Rev. B*, 47:558–561, 1993.

```
SYSTEM = Au+molecule
LPLANE = .FALSE.
PREC = ACCURATE
ADDGRID= .TRUE.
ICHARG = 2
ENCUT = 400
ENAU = 644.873
LREAL = A
ALGO = FAST
EDIFF = 1E-4
EDIFFG = -0.01
NSW = 300
IBRION = 1
ISMEAR = 0
SIGMA = 0.05
NELMIN = 6
MAXMIX = 100
NPAR = 10
NSIM = 1
LVTOT = .TRUE.
IDIPOL = 3
LDIPOL = .True.
GGA = MK
PARAM1 = 0.1234
PARAM2 = 1.0000
LUSE_VDW = .TRUE.
AGGAC = 0.0000
```

Figure D.1: A sample INCAR file that was used for optimization and work-function calculations in this work.

- [2] G. Kresse and J. Hafner. Ab initio molecular-dynamics simulation of the liquid-metal-amorphous-semiconductor transition in germanium. *Phys. Rev. B*, 49:14251–14269, 1994.
- [3] G. Kresse and J. Furthmüller. Efficiency of ab-initio total energy calculations for metals and semiconductors using a plane-wave basis set. *Comput. Mater. Sci.*, 6:15–50, 1996.
- [4] G. Kresse and J. Furthmüller. Efficient iterative schemes for ab initio total-energy calculations using a plane-wave basis set. *Phys. Rev. B*, 54:11169–11186, 1996.
- [5] G. Kresse and D. Joubert. From ultrasoft pseudopotentials to the projector augmented-wave method. *Phys. Rev. B*, 59:1758–1775, Jan 1999.
- [6] Cesare (ed) Pisani. *Quantum-mechanical ab-initio calculation of the properties of crystalline materials*. Springer, 1996.
- [7] P. E. Blöchl. Projector augmented-wave method. *Phys. Rev. B*, 50:17953–17979, 1994.
- [8] Pedro H. C. Camargo. *Electronic structure: basic theory and practical methods*. Cambridge University Press, 2008.
- [9] Roald Hoffmann. *Solids and surfaces: a chemist's view of bonding in extended structures*. Wiley, 1989.
- [10] Roald Hoffmann Richard Dronskowski. *Computational Chemistry of Solid State Materials: A Guide for Materials Scientists, Chemists, Physicists and others*. Wiley, 2006.

# Appendix E

## One phase reduction mechanism of Au (III) by dithiafulvene building blocks in aqueous media

### E.1 Simulated and experimental IR spectra

Figure E.1 are the experimental and simulated IR spectra of dimerized **3a** powder and residual particles of mixed dimerized **3a** and gold acid. As it can be seen, the spectra of the neutral compound match very well calculated spectra of dimerized neutral, while spectra of the compound after the reaction completed with gold acid shows better agreement with dimerized neutral too.

### E.2 Raman spectra of **3a**

Figure E.2 shows simulated and experimental Raman spectra of **4a** and dimerized **4a** in neutral state. The peak at  $1800\text{ cm}^{-1}$  which is due to C=O stretching can be clearly

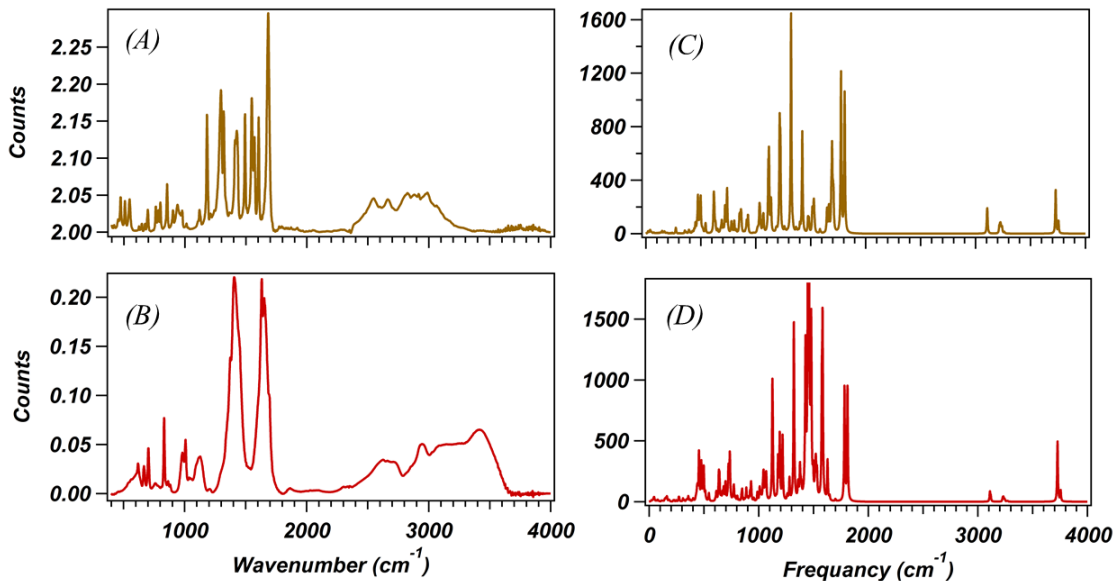


Figure E.1: IR spectra of (A) dimerized **3a** powder, (B) residual particles of mixed dimerized **3a** and gold acid solutions.(C) and (D) Calculated IR spectra of dimerized **3a** in neutral and oxidized forms in order.

seen in the experimental Raman spectra. The corresponding peak was disappeared in the Raman spectra of **3a** due to hydrogen bonding between nearby molecules through carboxyl group.

### E.3 calculated oxidation potential of gold

The oxidation potential of gold(I) to gold(0) in different solvents are computed with b3PW91/6-31+G (d,p) level of theory and basis set. Oxidation potentials are calculated in reference to a Ag/AgCl electrode ( $E^o(\text{Ag}/\text{Ag}^+) = +4.66 \text{ V}$ ) in Table E.1. The highest oxidation potential is found to be in chloroform which is a nonpolar solvent, and the lowest is calculated to be in the water with the highest polarity.

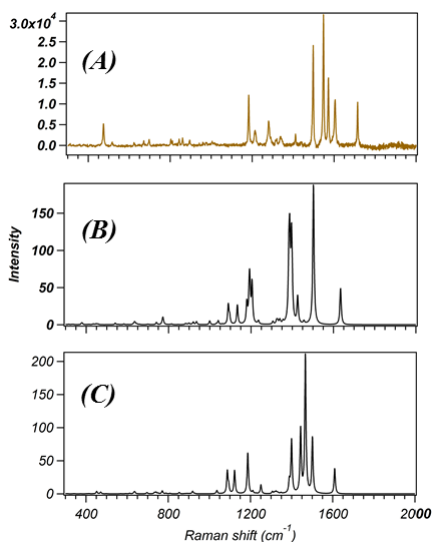


Figure E.2: (A) Experimental Raman spectra of **4a** in methanol. (B) Simulated Raman spectra of dimerized **4a**. (C) Simulated Raman spectra of **4a** in neutral states.

Solvent	$E^o_{(\text{Au}^+/\text{Au}^0)}$
Chloroform	1.51
THF	1.18
DCM	1.09
Acetone	0.83
Methanol	0.75
Acetonitrile	0.74
Water	0.68

Table E.1: The calculated oxidation potential of gold(I) to gold(0) in different solvents with b3pw91/6-31+g(d,p) level of theory and basis set (all values are reported in Volts).

## E.4 UV-Vis investigations of redox reaction

### E.4.1 UV-Vis spectra of **4a** before peak deconvolution

Figure E.3 represent the original UV-Vis spectra of **4a** in acetone before, right after addition of gold acid and twenty-four hours after mixing it with gold acid. To be able to analyze each peak clearly, spectra are deconvoluted to the involved peaks and shown in Figure 4.6.

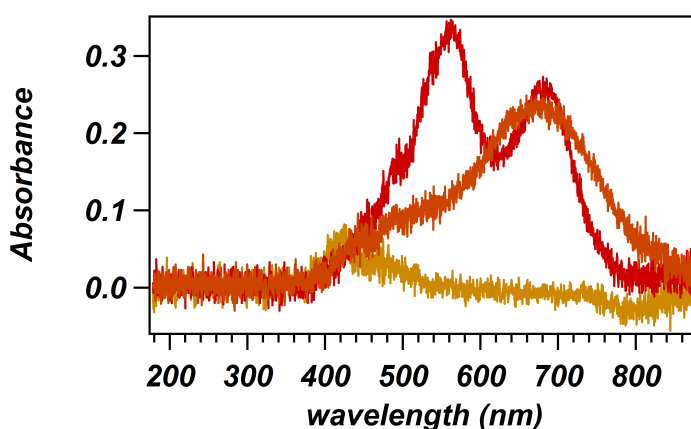


Figure E.3: UV-Vis spectra of **4a** in acetone (yellow graph), after addition of  $\text{HAuCl}_4$  for half an hour (Orange graph) and after twenty four hours (red graph).

### E.4.2 Time dependant UV-Vis measurements

The time-dependent spectra of **3a** in acetone and trace of water in three samples that ran individually for UV-Vis measurements are shown in Figure E.4. The time-dependent spectra of the first trial are shown in Figure 4.12. AuNP's characteristic peak at 520 nm did not appear at each trial, and the color of the solution turned back to yellow. Furthermore, the neutral compound absorption peak shifts to the higher wavelengths due to binding it to the gold species. The shift in HOMO>LUMO transition to the higher wavelengths represent a decrease in band gap due to covalent

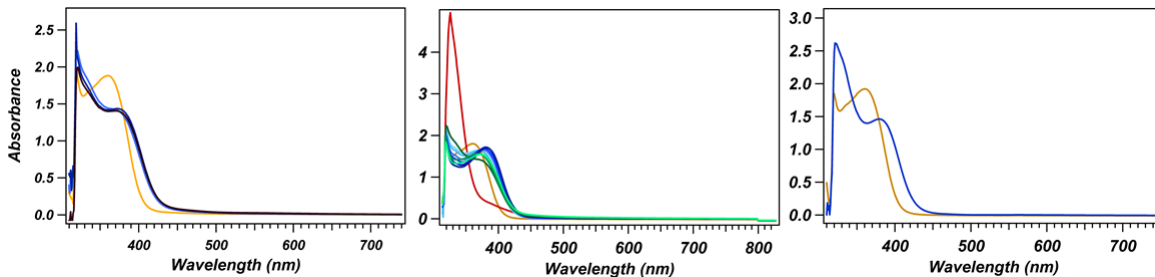


Figure E.4: Time-dependent UV-Vis spectra of 3 samples of **3a** in acetone and trace of water at different concentrations.

Oscillator strength ( $f$ )	Wavelength(nm)	transition	MO contribution
0.6032	382.49	HOMO>LUMO	0.68563
		HOMO>LUMO+2	0.14284
0.1647	279.05	HOMO-2>LUMO	0.63628
		HOMO-1>LUMO	-0.24479
		HOMO-1>LUMO+1	-0.10362
0.0396	207.32	HOMO-7>LUMO	0.59801
		HOMO-4>LUMO+2	-0.10458
		HOMO-2>LUMO+3	-0.23948
		HOMO-1>LUMO+3	-0.15859

Table E.2: Assignments of electronic transitions of **4a** in the neutral state.

bonding of **4a** with gold and lower energy transition of electrons from valence band to conduction band. UV-Vis spectroscopy is not an enough evidence showing the exact mechanism of interaction between **4a** and gold species. Although it can qualitatively says the formation of the functionalized nanoparticles through redox reaction and proofs formation of the major component in the solution.

### E.4.3 UV-Vis peaks assignments

The UV-Vis band assignments of the **4a** at neutral and oxidized form are reported in table. E.2, E.3. As can be seen, the maximum absorbance of **4a** appeared at 382.47.59 and 780 nm in neutral and oxidized forms which are correlated to the HOMO>LUMO and SOMO>LUMO ( $\alpha$ ,  $\beta$ ) transitions, respectively. The peak at 370 nm, which is

Oscillator strength ( $f$ )	Wavelength(nm)	transition	MO contribution
0.2089	787.59	SOMO>LUMO( $\alpha$ )	-0.18424
		SOMO>LUMO( $\beta$ )	0.97760
0.1693	437.48	SOMO>LUMO( $\alpha$ )	-0.53360
		SOMO-5>LUMO( $\beta$ )	0.72931
		SOMO>LUMO( $\beta$ )	-0.13607
		SOMO>LUMO+1( $\beta$ )	0.31734
0.3582	285.4	SOMO-1>LUMO( $\alpha$ )	0.70631
		SOMO-1>LUMO+2( $\alpha$ )	-0.10582
		SOMO-10>LUMO( $\beta$ )	0.13721
		SOMO-8>LUMO( $\beta$ )	-0.11651
		SOMO>LUMO+1( $\beta$ )	-0.59906
		SOMO-2>LUMO+3( $\beta$ )	-0.11189

Table E.3: Assignments of electronic transitions of **4a** in the radical cation state.

a maximum absorption of **4a** at the neutral form (Figure 4.2), was appeared at the same wavelength that was predicted computationally in the gas phase.

## E.5 Substituent effect on electronic levels

As can be seen in Figure 4.1, the R substituent on the benzene ring can be replaced by different substituents to modify electronic properties. The total energy and Fermi energy of the compound with the various substituents at three positions of ortho, meta and para are calculated and shown in Table E.4. Calculations are conducted with Abinit-7.6.4 software to perform electronic structure and ionic relaxation calculations based on the density functional theory in the local density approximation (LDA) using the exchange and correlation functional of Perdew using Projector Augmented-Wave (PAW) calculations. The maximal absolute force tolerance for structural relaxation iterations was set to 0.00004 Hartree/Bohr at which iterations will stop below this value. The value for tolerance indifference of forces was set to 0.000002 Hartree/Bohr. The energy cutoff was set at 300 eV. All the calculations were carried out using a very

Substituent\ Position	Ortho	Meta	Para
NO <sub>2</sub>	-159.839	-159.841	-159.845
NH <sub>2</sub>	-129.130	-129.131	-129.131
Br	-131.817	-131.824	-131.824
CH <sub>3</sub>	-125.603	-125.608	-125.608
CHO	-140.376	-140.377	-140.381
CN	-133.689	-133.693	-133.695
OCH <sub>3</sub>	-141.586	-141.592	-141.591

Table E.4: The total energies in eV for the compound in Figure 4.1 with different R substituents and at three positions of ortho, meta, and para on the benzene ring.

Substituent\ Position	Ortho	Meta	Para
NO <sub>2</sub>	-0.19273	-0.19074	-0.19977
NH <sub>2</sub>	-0.17926	-0.17681	-0.17071
Br	-0.18350	-0.18313	-0.18214
CH <sub>3</sub>	-0.18088	-0.17735	-0.17556
CHO	-0.18577	-0.18800	-0.19237
CN	-0.18622	-0.1888	-0.19215
OCH <sub>3</sub>	-0.17963	-0.17789	-0.17179

Table E.5: Fermi energies in eV for the compound in Figure 4.1 with different R substituents and at three positions of ortho, meta, and para on the benzene ring.

large supercell with  $30 \times 20 \times 20$  Å dimensions in which molecule do not interact with nearby cells.

The results are ordered based on the energy value from more stable on the top, which corresponds to the compound with NO<sub>2</sub> substituent, to the least stable on the bottom of the Table E.4. Furthermore, ortho substituent found to be less stable than two other positions. The Fermi energies also show the same trend from highest value for NO<sub>2</sub> to the lowest value for OCH<sub>3</sub> (Table E.5).

HOMO-LUMO gap energies are calculated with b3pw91/6-31+g(d,p) level of theory and basis set and reported in Table E.6 and E.7.

		NO <sub>2</sub>	NH <sub>2</sub>	Br	CH <sub>3</sub>
Ortho	HOMO	-0.20377	-0.19469	-0.20081	-0.19897
	LUMO	-0.09717	-0.04345	-0.04497	-0.04238
	$\pi - \pi^*$	0.10660	0.15124	0.15584	0.15659
Meta	HOMO	-0.20797	-0.19253	-0.20149	-0.19463
	LUMO	-0.10135	-0.04570	-0.05839	-0.04836
	$\pi - \pi^*$	0.10662	0.14683	0.14310	0.14627
Para	HOMO	-0.21343	-0.18281	-0.19985	-0.192880
	LUMO	-0.10287	-0.03823	-0.05839	-0.04682
	$\pi - \pi^*$	0.11056	0.14458	0.14223	0.14659

Table E.6: HOMO, LUMO, band gap energies of the ortho, meta, and para at neutral state obtained with b3pw91/6-31+g(d,p) level of theory and basis set.

		CHO	CN	OCH <sub>3</sub>
Ortho	HOMO	-0.19975	-0.20485	-0.19413
	LUMO	-0.07883	-0.06931	-0.04891
	$\pi - \pi^*$	0.12092	0.13554	0.14522
Meta	HOMO	-0.20533	-0.2078	-0.19550
	LUMO	-0.007813	-0.06931	-0.04938
	$\pi - \pi^*$	0.12720	0.13849	0.14612
Para	HOMO	-0.20725	-0.20976	-0.18866
	LUMO	-0.08493	-0.07953	-0.04207
	$\pi - \pi^*$	0.12232	0.13023	0.14659

Table E.7: HOMO, LUMO, band gap energies of the ortho, meta, and para at neutral state obtained with b3pw91/6-31+g(d,p) level of theory and basis set.

Substituent	Ortho		Meta		Para	
	DTF	DTF <sup>0+</sup>	DTF	DTF <sup>0+</sup>	DTF	DTF <sup>0+</sup>
NO <sub>2</sub>	53.9	59.0	-10.2	-9.0	-9.4	-18.0
NH <sub>2</sub>	-50.4	-32.10	-22.8	-3.7	-19.1	-1.2
Br	-77.1	-66.7	-13.7	0.0	-16.3	0.1
CH <sub>3</sub>	-61.1	-51.4	-19.5	-11.0	-19.1	0.2
CHO	-41.6	-45.3	-15.2	-17.1	-12.0	-15.1
CN	-47.1	-47.2	-12.6	-17.6	-11.8	-14.8
OCH <sub>3</sub>	-35.9	-18.4	-22.1	11.7	-19.6	0.0

Table E.8: C<sub>1</sub>–C<sub>2</sub>–C<sub>3</sub>–S<sub>1</sub> dihedral angles before and after oxidation for the compound with different Substituents at three positions of ortho, meta, and para.

## E.6 Substituent effect on structural properties

Table E.8 shows C<sub>1</sub>–C<sub>2</sub>–C<sub>3</sub>–S<sub>1</sub> (as shown in Figure E.5) dihedral angle changes after oxidation.

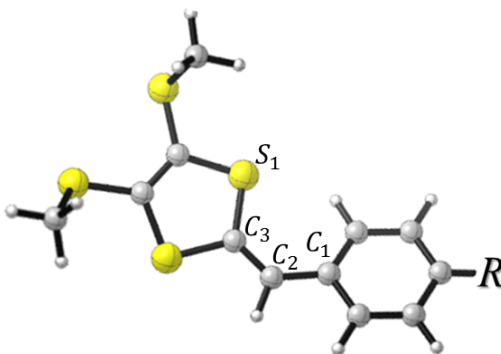


Figure E.5: The structure of dithiafulvenyl with R substituent at the para position of the benzene ring.